Clemson University

TigerPrints

All Theses

Theses

8-2023

Modeling Heat Propagation and Thermal Enhanced Decay in a Solar Thermal Remediation System

Justin Trainor
jttrain@g.clemson.edu

Recommended Citation

MODELING HEAT PROPAGATION AND THERMAL ENHANCED DECAY IN A
SOLAR THERMAL REMEDIATION SYSTEM

A Thesis

Presented to

the Graduate School of

Clemson University

In Partial Fulfillment

of the Requirements for the Degree

Master of Science

Hydrogeology

by

Justin Timothy Trainor

August 2023

Accepted by:

Dr. Ronald Falta, Committee Chair

Dr. Lawrence Murdoch

Scott Brame

ABSTRACT

Low temperature solar thermal remediation is designed to accelerate ongoing biotic and abiotic treatment processes at a much lower temperature and cost than high temperature thermal remediation strategies. An array of borehole heat exchangers are used to circulate a solar-heated fluid through a closed-loop system of thermally conductive pipes. Thermal energy heats the surrounding contaminated zone through the process of thermal conduction which serves to enhance the degradation of the contaminant.

A three dimensional analytical solution was previously constructed to model heat propagation from borehole heat exchangers into the surrounding subsurface. The model utilizes a system of finite line sources to describe the borehole heat exchangers while accounting for variable borehole heating rates as well as multiple borehole heaters. This user-friendly simulation model can calculate subsurface temperature change at a low computation time, and is currently being used as a guidance tool for designing and optimizing solar thermal remediation systems. The analytical design tool has been validated by comparison with field data from a solar thermal remediation test site in Colorado, and is currently being used to optimize a detailed field test on Vandenberg Space Force Base in Southern California. The analytical model is compared to high-resolution temperature data during early stages of the test, and then used to predict the longer-term performance of the solar thermal remediation system.

A new feature has been added to the analytical design tool to estimate the thermal-enhanced decay of a contaminant using a modified first-order decay solution. This new capability uses temperature-dependent decay rates to project the thermal-enhanced decay of

volatile organic compounds (VOC's) over time, and is used to model VOC destruction at Vandenberg Space Force Base. With the ability to analyze the impact of increasing subsurface temperature on the duration of bioremediation projects, the decay tool offers an additional advantage in optimizing these types of remediation systems.

ACKNOWLEDGEMENTS

I am deeply grateful for having Dr. Falta as my research advisor and the opportunity to take part in this research. Thank you for your patience, promptness, guidance, and expertise in subsurface remediation modeling that you shared with me.

I'd like to recognize my committee member Dr. Murdoch for always challenging me in every course that I took here (and during my Thesis Defense) in the Hydrogeology Master's Program at Clemson University. Your enthusiasm and dedication to your students' learning and growth are one of the many reasons I joined this program.

I'd also like to recognize my committee member Scott Brame for all the outstanding work he does in putting together the Clemson Hydrogeology Field camp as well as the Hydrogeology Symposium. Because of him, I learned so much about hydrogeologic field methods and I had the privilege of presenting my research at the largest gathering of professionals focused on hydrogeology in the Southeast U.S. (and had a lot of fun doing it).

TABLE OF CONTENTS

FIGURES

TABLES

1. INTRODUCTION

Volatile organic compounds (VOC's) are chemicals that are commonly released into the environment as industrial and commercial waste products, often in the form of chlorinated solvents (USGS, 2006). Common organic chemicals such as benzene, tetrachloroethylene, and trichloroethylene (TCE) can persist in groundwater for long periods of time because their properties allow them to resist natural degradation and remain in either aqueous or gas phases as a contaminant plume (CA EPA, 2010). Even the smallest concentrations can surpass drinking water standards, making these contaminants a health risk to the public. To maintain these limits, groundwater remediation is often required to either physically remove these chemicals from the contaminated site or to accelerate the degradation of these compounds into less harmful constituents.

While many remediation strategies for eliminating VOC's exist in the environmental world, thermal remediation has proven to be an effective approach. Heat transfer properties of most soils are relatively constant and don't vary with grain size, which means that thermal remediation can be effective in both high and low-permeability zones (Divine, 2020). However, there are still many different methods of thermal remediation and choosing the right one for a contaminated site will depend on the type of contaminant involved, properties of the polluted soil, availability of water, as well as the soil's heat sensitivity (Vidonish et al., 2016).

Low-temperature thermal remediation is an attractive method because it can accelerate ongoing biotic and abiotic treatment processes at a much lower temperature and cost than remediation strategies that operate at the boiling point or above such as high-temperature conductive heating, electrical resistive heating, steam injection, and radio frequency heating for

example. Thermal remediation methods that operate at high temperatures may alter ecosystems by decomposing soil minerals and organic matter (Vidonish et al., 2016). Low-temperature thermal remediation aims to avoid these scenarios and therefore may be a more sustainable approach to environmental remediation.

Moderate increases in subsurface temperature have been shown to enhance biodegradation by boosting the mesophilic activity of primary dechlorinating bacteria. For instance, Macbeth, et al. (2012) observed a fourfold increase in TCE dechlorination rate by increasing its temperature from 10 to 30 °C and Suthersan, et al. (2012) reported a 50% reduction in the half-life of 1,1,1-Trichloroethane by increasing ambient temperatures by just 10 °C. Biodegradation rates of petroleum hydrocarbons were also shown to increase threefold after increasing soil temperatures from 10 to 20 °C (Margesin and Schinner, 2001). Peak biodegradation rates of hydrocarbons have been observed between 30 °C and 40 °C (Xu et al., 1997). The half-life of 1,1,1-TCA was observed to be reduced by 3 orders of magnitude after heating groundwater up to 40 °C which shows that moderate heating can also increase abiotic reactions in the subsurface (Horst et al., 2018).

Increases in subsurface temperature have also been shown to enhance the physical extraction of organic contaminants from soils by boosting their solubility and susceptibility to partition from aqueous to gas phase. Suthersan, et al. (2012) observed that hydrolysis rates of some organic compounds increased with rises in temperature and Chen et al. (2012) showed how the Henry's law constants of twelve common VOCs increases by factors of 2 to 10 between temperatures of 8 and 38 °C. Therefore, low-temperature thermal remediation can be effective when applied in conjunction with other remediation strategies, including soil vapor extraction,

air sparging, chemical oxidation, and most notably bioremediation of chlorinated solvents (Divine, 2020).

Conventional building and cooling systems that use air-water heat pumps can achieve moderate increases in subsurface temperature (Horst et al., 2018), however while these systems have relatively low installation, operation, and maintenance costs, the technology is reliant on a source of fuel or electricity to provide the energy that is transferred into the ground. Solar subsurface heating systems are a more sustainable method because they utilize solar radiation in place of expending fuel or electricity to transfer heat into the subsurface (Horst et al., 2018).

While solar subsurface heating systems are more expensive to install than conventional heating methods (Lazaar, 2015), there are no utility costs to maintain the heat transfer. Additionally, the technology's control system and recirculation pump can be powered using photovoltaic solar panels, which means that these systems can operate even in remote locations (Horst et al., 2018). One application of this technology, known as the Thermal In-Situ Sustainable Remediation (TISR^{TM}), was developed by Arcadis and demonstrated how capital investments can be paid back within three years or less from the start of heating, and that the total treatment time can be reduced by three to five years (Divine, 2020).

1.1 Solar Thermal Remediation of Volatile Organic Compounds

Solar thermal remediation is a low-temperature heating method that uses solar-powered borehole heat exchangers (BHEs) to heat the subsurface to 15-40 ∘C and accelerate ongoing biotic and abiotic treatment processes. As shown in Figure 1, a solar heated fluid is circulated

from a collection of solar panels to an array of BHEs through a closed-loop system of thermally conductive pipes.
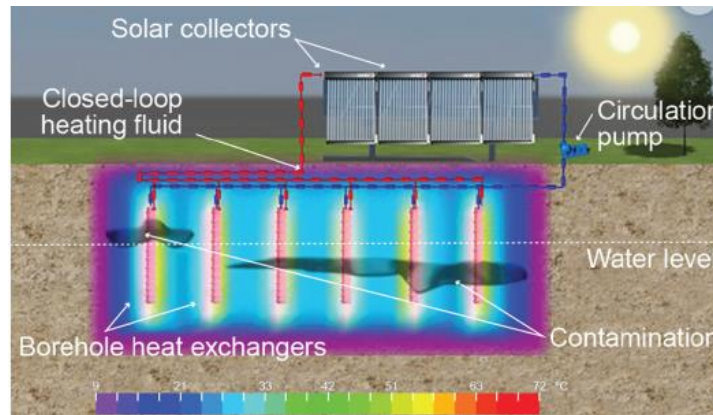
Figure 1. Diagram of a typical solar thermal remediation system: Closed-loop array of borehole heat exchangers with a circulating working fluid heated by solar panels (Horst et al., 2018).

The component of the closed-loop system of pipes that are placed into boreholes are typically configured as either a U-tube formation, where elongated vertical inlet and outlet tubes resemble a U-shape, or as a spiral coil. The spiral coil configuration has a higher surface area and therefore allows for more heat transfer while limiting the amount of air that can be trapped within the pipe (Man et al., 2010). Figure 2 shows how the solar heated mixture of glycol fluid and water is funneled into the center tube of each BHE before returning up to the ground surface through an outer coiled tube. During this process, thermal energy that is being applied to the BHE from the incoming fluid is transferred into the surrounding subsurface via conduction, which serves to enhance the degradation of the contaminant. The degree of this heat transfer largely depends on the temperature difference between the heated fluid and the surrounding subsurface.
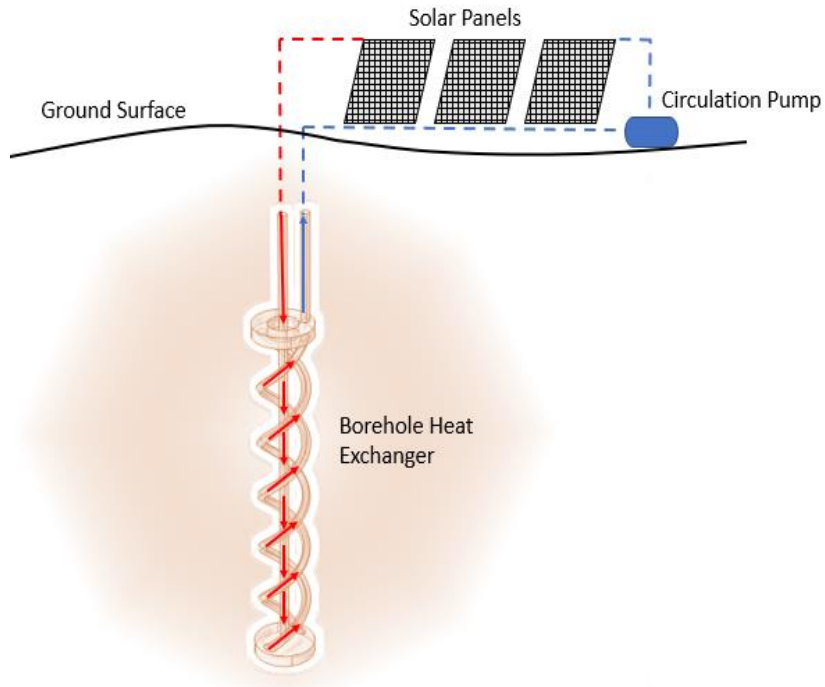
Fig. 2. Diagram of heat being transferred from a circulating fluid into the surrounding subsurface via a BHE of a solar thermal remediation system.

As heat propagates outward into the cooler soil matrix, the temperature of the space surrounding the BHE will rise until it approaches that of the heated fluid and an equilibrium is reached. The circulating fluid in this closed-loop system is cooled as a result of the heat transfer and is returned to the solar panel array to be reheated. If the BHE is installed below the water table, then heat that has been transferred into the subsurface can be pushed away from the remediation system by convection. Installation of low-temperature thermal remediation systems such as this in areas of high groundwater velocities would be unfavorable, as the system could fail to achieve desired temperatures in the subsurface (Ornelles et al., 2022).

1.2 Motivation for Modeling Heat Propagation and Thermal Enhanced Decay

Modeling heat propagation from the BHE's is an important step in the design and development of the solar thermal remediation system. In order to meet specific energy demands and costs of a thermal remediation project, the gradual temperature response in the subsurface should be taken into account before installation of the technology at a field site. This way, the orientation and geometry of the system can be constructed to meet those energy demands and costs as closely as possible (Molina et al., 2011). Therefore, there is a need for using modeling software to predict subsurface temperature response from different solar thermal remediation system configurations.

For example, an environmental entity implementing solar thermal remediation would need to have a good estimate of the number of solar panels required to supply enough power to achieve a target subsurface temperature. By modeling heat propagation from the proposed site configuration, they may find that the current configuration of the proposed test site is insufficient, and that additional solar panels will be required to reach the target subsurface temperature. Conversely, they may find that the proposed system configuration may exceed the target subsurface temperature, and project costs may be cut by reducing the number of solar panels in the proposed system configuration.

In addition to the BHE-subsurface temperature response, modeling the thermal enhanced decay of the contaminant of interest is another advantageous approach for designing and developing solar thermal remediation systems. Estimating the degree that a contaminant's decay rate will be thermally enhanced can give insight on how long a solar thermal remediation project could potentially take. This could have great implications on the project's ability to meet specific energy demands and costs. Modeling the thermal enhanced decay at a solar thermal remediation

site can also give insight on the cost benefits of operating at higher temperatures than ambient conditions.

1.3 Advantages of Using Analytical Solutions to Model Subsurface Heat flow

Numerical solutions are typically used to solve most heat transfer problems in engineering industries. Complex heating problems that involve heterogeneities in the hydrogeologic setting or geometry can often be difficult or even impossible to solve analytically. Numerical methods such as finite element, finite volume, finite difference, and boundary element method can offer approximate solutions to heat transfer problems that are sufficiently accurate (Mehta et al. 2013).

If the hydrogeologic setting of the solar thermal remediation system is simplified where isotropic groundwater flow and subsurface homogeneity is assumed, then the use of an analytical solution for heat transfer can produce very similar results to multiphase numerical models (Ornelles, 2021). In such cases, analytical solutions can be beneficial because they typically have shorter computation times than numerical solutions, are numerically exact, and are continuous in time and space (Anderson et al., 2015). This becomes a more efficient approach for optimizing thermal remediation systems because while data are still needed for analytical model input, less preliminary work is required to set up the model.

2   RESEARCH OBJECTIVES

Previous research for this project focused on developing and validating the solar thermal remediation design tool by comparison with numerical models and some test site temperature data. This study aims to continue validating the design tool by modeling an additional solar thermal remediation test site on Vandenberg Space Force Base in Southern California. The study will also focus on the development of a new thermal enhanced decay capability that has been added to the design tool.

The first critical research objective for this paper is to model heat propagation from the solar thermal remediation system on Vandenberg Space Force Base using the analytical design tool. Simulated temperature change around the heat exchangers is calibrated to high-resolution temperature data during early stages of the heating test to predict the long-term performance of the solar thermal remediation system at the site. The simulation is calibrated using a range of groundwater velocities in order to gauge the possible source of heterogeneity in the subsurface that could potentially cause uncertainty in the analytical model.

The second critical research objective is to estimate potential thermal enhanced decay on Vandenberg Space Force Base using the new decay feature of the analytical design tool. The decay tool is used to demonstrate how the current configuration of the solar thermal remediation system can be optimized by altering the configuration of solar collectors and BHE's in the remediation system.

3 THE ANALYTICAL SOLAR THERMAL REMEDIATION DESIGN TOOL

Ornelles (2021) and Ornelles et al. (2022) modified a three dimensional analytical solution to model heat propogation from borehole heat exchangers into the surrounding subsurface. The model utilizes a system of finite line sources to describe the borehole heat exchangers while accounting for groundwater flow, axial effects, and multiple borehole heat exchangers with time-varying heating rates. Their model has been modified to include an additional capability where it can calculate the thermal enhanced decay of a contaminant at any given point in time and space due to heating. This feature gives the user an idea of how the decay rate of the contaminant can be thermally enhanced by the borehole heat exchangers, and allows for more flexibility in optimizing thermal remediation systems. The model was previously shown to calculate subsurface temperature change to an acceptable level of accuracy compared with comprehensive numerical models and actual temperature data from two solar thermal remediation test sites (Ornelles, 2021).

The analytical design tool has been validated by comparison to the proven TOUGH EOS1 and TOUGH EOS3, which are numerical multiphase modeling codes used to simulate heterogeneous and often complex hydrogeological systems. Subsurface heatflow from BHE's with the analytical modeling tool was compared to that of the numerical model under a number of different conditions including fully and partially saturated conditions, variable hydraulic conductivity, groundwater flow, and multiple BHE's with seasonally variable heat flow (Ornelles, 2021).

.

Analytical models that can simulate heat transfer from borehole heat exchangers into the surrounding subsurface by conduction can be divided into two main categories: infinite and finite line source models. Infinite line source models simulate heat transfer radially from an infinitely long line and as a result neglect vertical heat flow. While this method can accurately predict subsurface temperature change for shorter run-times, the axial thermal effects that occur at the top and bottom of shallow borehole heat exchangers can eventually play a larger role in the heat transfer after a certain amount of time of heating (Philippe, 2009). Infinite line source models are also unable to simulate steady-state conditions and can yield higher temperature changes, leading to the general under-sizing of BHE lengths in designing solar thermal remediation systems (Molina et al., 2011). For these reasons, finite line source models are more appropriate for simulating longer-term subsurface heating.

3.1 Analytical Solution Using Finite Line Sources to Describe BHE's

Ornelles (2021) and Ornelles et al. (2022) modified a moving finite line source solution that was developed by Molina et al. (2011) that could account for additional heat transfer by convection via groundwater flow. The governing equation that describes three-dimensional temperature change around a single BHE is defined by Equation 1 where T is the average temperature of the subsurface material (°C) at time t (s) at a given point in space x,y,z (m), ϕ is the porosity, ρ_w is the water density (kg/m^3), C_w is the water heat capacity (J/kg/°C), C_R is the rock grain heat capacity (J/kg/°C), ρ_R is the rock grain density (kg/m^3), V_d is the darcy velocity (m/s), and λ is the bulk thermal conductivity of the porous medium (W/m/K).

$$\frac{\partial T}{\partial t}[\phi\rho_w C_w + (1-\phi)C_R\rho_R] = -V_d\rho_w C_w \frac{\partial T}{\partial x} + \lambda\frac{\partial^2 T}{\partial x^2} + \lambda\frac{\partial^2 T}{\partial y^2} + \lambda\frac{\partial^2 T}{\partial z^2} \quad \text{(Equation 1)}$$

Ornelles (2021) and Ornelles et al. (2022) modified the Molina et al. (2011) solution to simulate temperature change around an array of multiple BHEs with variable heating rates by applying superposition in time and space, and dividing the power delivery into equally spaced heating periods. This solution was developed as a guidance tool for designing and optimizing solar thermal remediation systems.

Equation 2 is implemented into the design tool, where T_0 is the initial temperature of the subsurface material (°C), Q and Q_{mn} are the thermal energy flow rate (J/s or W), a_m and b_m are the top and bottom depths defining the length of the BHE (m), v_T is the effective linear flow velocity (m/s), and α is the thermal diffusivity of the porous medium (m^2/s).

$$T = T_0 + \sum_{n=0}^{n} \sum_{m=1}^{n_{heater}} \left\{ \frac{\Delta Q_{mn}}{2\pi\lambda(b_m - a_m)} e^{\frac{v_t x}{2\alpha}} \left[\int_{a_m}^{b_m} f_m(x,y,z,(t-t_n)) - \int_{-b_m}^{-a_m} f_m(x,y,z,(t-t_n))dz' \right] \right\}$$

(2)

The thermal conductivity can be described by Fourier's Law for heat conduction shown as Equation 3, where q_x is the heat flux in the x direction through a given cross sectional area (W/m^2) and $(\partial T / \partial x)$ is the temperature gradient in the x direction (°C/m).

$$q_x = -\lambda \frac{\partial T}{\partial x}$$

(3)

The thermal diffusivity can be defined in Equation 4 as the thermal conductivity divided by the total volumetric bulk heat capacity C_b $(J/m^3/°C)$, which is the sum of the groundwater and subsurface material bulk heat capacities.

$$\alpha = \frac{\lambda}{\phi\rho_w C_w + (1-\phi)\rho_R C_R}$$

(4)

The effective linear flow velocity, v_T can be defined in Equation 5 as the darcy velocity V_d (m/s) mulitiplied by the water density and heat capacity, divided by the total volumetric bulk heat capacity.

$$v_T = \frac{V_d \rho_w C_w}{\phi \rho_w C_w + (1-\phi)\rho_R C_R} \qquad (5)$$

Equation 2 involves a finite line source heat flow, Q over a specified vertical thickness from the top of the heat exchanger, a to the bottom, b (Figure 3). The porous medium material is assumed to be homogeneous and groundwater flow is assumed to be isotropic and extend to the ground surface.
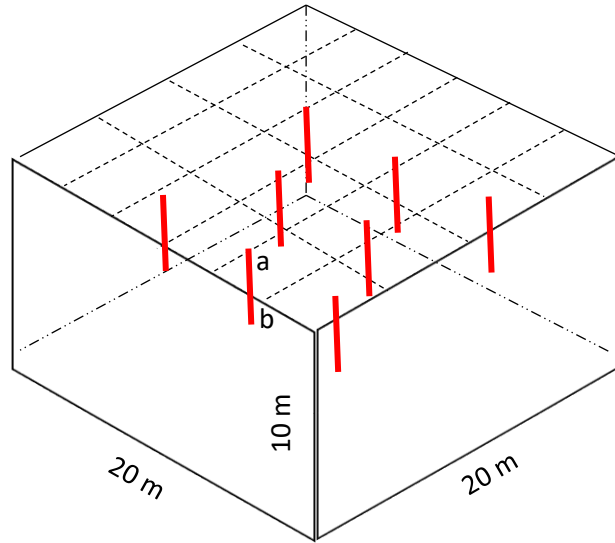
Figure 3. A 3D representation of some finite line sources used to model heat propagation from an array of BHEs (Molina et al., 2011).

The added effects of having multiple BHEs in the design is made possible using Equation 2 by summing every temperature change for a specified number of borehole heat exchangers, n_{heater} at their given locations in time.

Equation 2 also allows for a variable borehole heating rate where the heatflow at each borehole at a specified heating period, Q_{mn} is broken up into time steps where n is the number of

heating periods, m specifies the applicable borehole heat exchanger, and t_n marks the starting time of heating period n.

The function that is integrated with depth in Equation 2 is defined by Equation 6 where r_m is the radial distance from heat source m (m).

$$f\left(x, y, z, (t - t_n)\right) = \frac{1}{4r_m}\left[e^{\frac{-v_T r_m}{2\alpha}} erfc\left(\frac{r_m - v_T(t - t_n)}{2\sqrt{\alpha(t - t_n)}}\right) + e^{\frac{v_T r_m}{2\alpha}} erfc\left(\frac{r_m + v_T(t - t_n)}{2\sqrt{\alpha(t - t_n)}}\right)\right]$$

(6)

The distance from the heater, r_m can be described using Equation 7 where x_{0m} and y_{0m} are cartesian coordinates for the BHEs (m) and z is a vertical coordinate (m).

$$r_m = \sqrt{(x - x_{0m})^2 + (y - y_{0m})^2 + (z - z')^2}$$

(7)

3.2 Analytical Solution that Describes Thermal Enhanced Decay

In the current work, the analytical modeling tool has an additional function that can calculate the enhanced decay of a contaminant in the vicinity of the BHE's over time. Thermal enhancement of VOC biodegradation is well documented in environmental remediation of chlorinated solvents. Peak enhancement has been observed to occur between 30-40 degrees Celsius which can result in a four-fold increase in dechlorination rate (Macbeth et al, 2012). Suthersan et al. (2012) observed that a 10 degree increase in temperature can reduce the 1,1,1-TCA half-life by 50%.

Modeling thermal enhanced decay of VOC's can be a difficult task because decay coefficients can vary between biomass populations. This may be because there are additional factors that can affect the extent of reductive dechlorination other than temperature, such as electron donor/acceptor availability, toxic chlorinated ethene concentrations, or metabolism of the microbial species (Bryck, 2014). For this project, the decay factors used to model thermal enhanced decay were estimated based on the Arrhenius Equation where the decay factors double for every ten degree increase in temperature between 20 and 40 ◦C.

The decay tool in the analytical model uses a first order decay equation to calculate the ratio of the thermally enhanced concentration $\left(\frac{C_{Thermal}}{C_0}\right)$ to the base case concentration $\left(\frac{C_{base}}{C_0}\right)$ at any location after a specified amount of time. The resulting decay ratio $\left(\frac{C_{Thermal}}{C_{base}}\right)$ is useful because it estimates the additional decay that occurrs at a specific location after a specified amount of time, compared to that which would occur without thermal enhancement.

Ordinary first-order decay can be derived starting with a governing equation for normal solute decay in the aqueous phase as described by Equation 8, where λ_b is the base decay rate, R is the retardation factor, C is the concentration, and ϕ is the porosity.

$$\phi R \frac{dC}{dt} = -\phi \lambda_b C \qquad (8)$$

$\int_{C_0}^{C} \frac{dC}{C} = \int_{t_0}^{t} \frac{-\lambda_b}{R} dt$ \qquad where $t_0 = 0$ seconds

When both sides are integrated, the solution is:

$LnC(t) - LnC_0 = \frac{-\lambda_b}{R}(t - t_0)$ which is equal to Equation 9:

$$\frac{C(t)}{C_0} = e^{\frac{-\lambda_b}{R}t} \qquad (9)$$

Equation 9 calculates the base case decay (C_{base}) as a function of time without the influence of temperature. If the decay rate becomes a function of temperature, and temperature is a function of time, then the decay rate is also a function of time and $\lambda = \lambda(t)$. Then the solution becomes:

$Ln\frac{C(t)}{C_0} = -\frac{1}{R}\int_0^t \lambda(t)dt$ which is equal to Equation 10:

$$\frac{C(t)}{C_0} = e^{-\frac{1}{R}\int_0^t \lambda(t)dt} \qquad (10)$$

The time-dependent thermal conductivity can be rewritten as: $\lambda(t) = \lambda_b F_T$ where F_T is the temperature-dependent decay factor that is also time-dependent. Equation 10 then becomes:

$$\frac{C(t)}{C_0} = e^{-\frac{\lambda_b}{R}\int_0^t F_T dt} \qquad (11)$$

For a specified location in space, F_T is numerically integrated with respect to time using the Trapezoidal Rule. The period of time from the start of heating to the specified end-time is divided into *nt* time intervals and the decay factor at each time step is determined using the temperature calculated from the analytical model at each point in time. The relationship between temperature and decay factor is specified by the user in the model interface where a decay factor is assigned to each indicated temperature between 0 and 60 ∘C.

15

Figure 4 shows the portion of the analytical model's user interface where decay factors can be assigned to different temperatures. Between the 5-degree temperature intervals, the decay factors are linearly interpolated by the analytical model before being numerically integrated using Equation 11 (for more information regarding the model user interface, see Appendix 1).

temperature C	decay factor
0	0.1
5	0.2
10	0.5
15	0.71
20	1
25	1.41
30	2
35	2.8
40	4
45	2
50	1
55	0.5
60	0.2

Fig. 4. Thermal enhanced decay input window in the model's user interface where decay factors can be assigned to temperatures between 0 ◦C and 60 ◦C

Figure 5 shows an example of how a third decay factor is linearly interpolated between 2 user-specified decay factors from Figure 4 at a temperature of 22 ◦C.
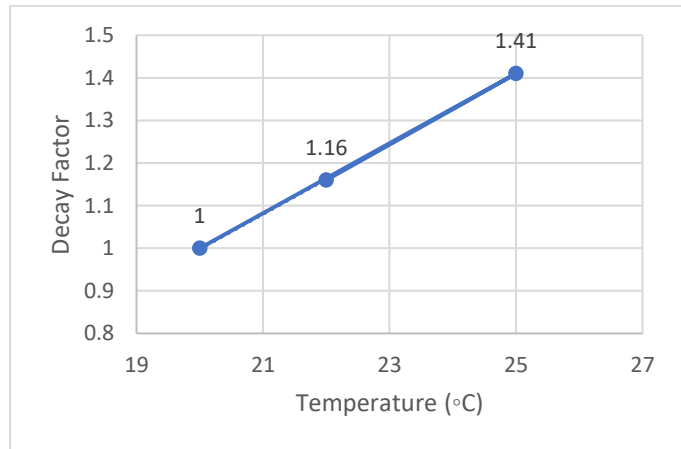
Fig. 5. Linear interpolation between 2 defined decay factors in the analytical model.

The complete equation for the thermal enhanced concentration ($C_{Thermal}$) at a single

point after a specified amount of time is described by Equation 12:

$$\frac{C(t)}{C_0} = exp\left\{-\frac{\lambda_b}{R}\sum_{n=0}^{nt}\frac{\Delta t}{2}(F_{Tn} + F_{Tn-1})\right\} \qquad (12)$$

Finally, the decay ratio $\left(\frac{C_{Thermal}}{C_{base}}\right)$ that is computed by the analytical design tool at each

point after a specified amount of time can be calculated by dividing Equation 12 by Equation 9:

$$\frac{C_{Thermal}}{C_{base}} = \frac{exp\left\{-\frac{\lambda_b}{R}\sum_{n=0}^{nt}\frac{\Delta t}{2}(F_{Tn}+F_{Tn-1})\right\}}{exp\left\{\frac{-\lambda_b F_T(T_0)}{R}t\right\}} \qquad (13)$$

It should be noted that in Equation 13, the decay factor at the initial background

temperature, $F_T(T_0)$ has been added to the base case concentration component of the decay

ratio. In most cases this term will equal 1 because at ambient temperatures, contaminant decay

will generally occur at the base decay rate, λ_b. However, if the user decides to assign a decay

factor other than 1 to the background temperature, then the $F_T(T_0)$ term becomes relevant and

should be included in Equation 9. It should also be noted that this approach assumes that the

contaminant is stationary and fixed to a single position in space through time. This is a key

limitation of this approach for modeling thermal enhanced decay because the analytical design

tool is unable to account for convectional transport of the chemical via groundwater flow.

3.2.1 Example Computation of the Decay Ratio at a Single Point

To demonstrate how the equations in Section 3.2 are used to compute the decay ratio in the analytical design tool, the base decay, thermal enhanced decay, and decay ratio at a single point in space are considered after 3 years of heating. The decay properties along with the temperature-dependent decay factors are shown in Table 1.

Decay Tool Properties	
days since start of heating, t	1095 days (3 years)
time step (Δt)	219 days (0.6 years)
base decay rate, λ_b	0.35 1/year
retardation factor, R	2
background temperature	18.5 (◦C)
Temperature (◦C)	**Decay Factor**
15	1
20	1.5
25	2
30	3

Table 1. Decay variables along with the assigned temperature-dependent decay factors to demonstrate calculating the decay ratio $\left(\frac{C_{Thermal}}{C_{base}}\right)$ with time.

The base case concentration (C_{base}) after 3 years is calculated using Equation 9. The initial temperature at t(0) is 18.5 ◦C which, referencing Table 1, corresponds to a decay factor between 1 and 1.5. The decay factor that is linearly interpolated at a temperature of 18.5 ◦C between these two factors is 1.35, so the base case concentration after 3 years is:

$$\frac{C_{base}}{C_0} = e^{\frac{-(0.35\ ^1/yr)(1.35)}{2}(3\ yr)} = 0.49$$

The units of λ_b and t cancel, and after 3 years of degrading at the base decay rate, the contaminant concentration has been reduced by 51%.

The thermal enhanced concentration ($C_{Thermal}$) after 3 years of heating is calculated using Equation 12 where F_T is numerically integrated using the Trapezoidal Rule and the 3-year heating period is divided into 5 time-intervals of 0.6 years:

$$\int_0^3 F_T dt = \sum_{n=0}^5 \frac{0.6}{2}\{F_{Tn} + F_{Tn-1}\} \quad \text{which is equal to:}$$

$$\frac{0.6}{2}\{F_{T(0\ yr)} + 2F_{T(0.6\ yr)} + 2F_{T(1.2\ yr)} + 2F_{T(1.8\ yr)} + 2F_{T(2.4\ yr)} + F_{T(3\ yr)}\}$$

The decay factor at each time step depends on the temperature that has been computed by the analytical model at the single point of interest for each time. After obtaining the temperature results from the design tool, the equation above can be rewritten as:

$$\frac{0.6}{2}\{F_{T(18.5°C)} + 2F_{T(24.75°C)} + 2F_{T(28.7°C)} + 2F_{T(28.19°C)} + 2F_{T(28.64°C)} + F_{T(29.13°C)}\}$$

Referencing Table 1, the temperature-dependent decay factors are linearly interpolated and the integration becomes:

$$\sum_{n=0}^5 \frac{0.6}{2}\{F_{Tn} + F_{Tn-1}\} = \frac{0.6}{2}\{(1.35) + 2(1.975) + 2(2.74) + 2(2.638) + 2(2.728) + (2.826)\} = 7.30\ yr$$

The integrated F_T is substituted into Equation 12 along with the base decay rate and retardation factor:

$$\frac{C_{Thermal}}{C_0} = e^{\frac{-(0.35\ ^1/yr)}{2}(7.30\ yr)} = 0.28$$

The units of λ_b and t cancel, and after 3 years of thermal enhanced decay, the contaminant concentration has been reduced by 72%.

The decay ratio $\left(\frac{C_{Thermal}}{C_{base}}\right)$ after 3 years of heating at the single point of interest can finally be calculated where C_0 is canceled out and the ratio becomes:

$$\left(\frac{C_{Thermal}}{C_{base}}\right) = \left(\frac{C_{Thermal}}{C_0}\right)\left(\frac{C_0}{C_{base}}\right) = \frac{0.28}{0.49} = 0.57$$

At the single point of interest after 3 years of heating, the contaminant decay has been thermally enhanced by 43%. This method of evaluating concentrations as ratios is convenient because it dismisses the need to account for an initial contaminant concentration while setting up the model.

4   MODELING BHE HEAT FLOW AT VANDENBERG SPACE FORCE BASE

4.1 Installation of the Solar Thermal Remediation System

The analytical design tool was developed as one of the main objectives for Project ER20-5028 of the Environmental Security Technology Certification Program (ESTCP), where it was intended to function as a "practical guidance document and design tool" for optimizing solar thermal remediation systems (Divine, 2020). The test site chosen for this project is located on Vandenberg Space Force Base in Southern California, which lies at approximately 40 degrees N and 105 degrees W. A base map of the test site is shown in Figure 6 where an array of 8 BHE's have been installed and are powered by a system of 8 flat plate solar panels.
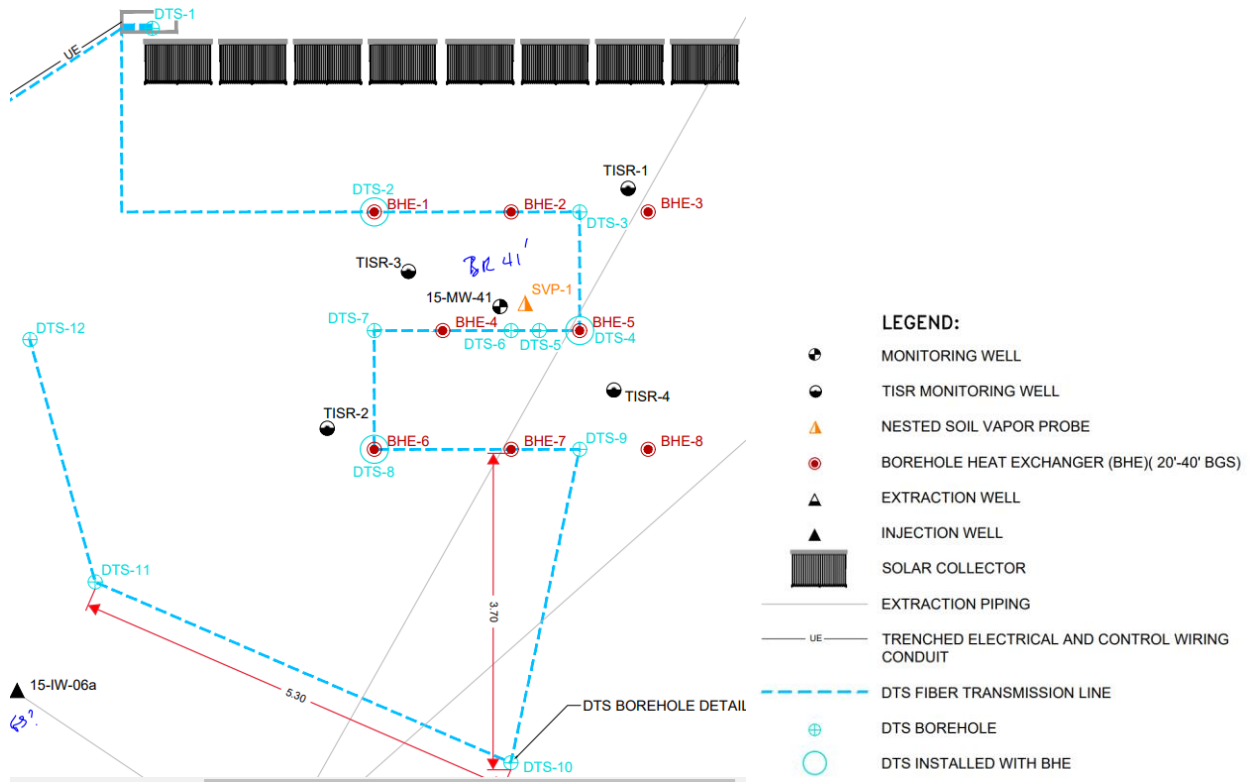
Fig. 6. Basemap of the Vandenberg solar thermal remediation test site (Arcadis U.S., Inc., 2021).

A series of twelve fiber optic distributed temperature sensors (DTS 1-12), devices that can measure temperature with submillimeter spatial resolution, were placed at various distances from the BHE's. Figure 7 illustrates the installation of the DTS sensors at the Vandenberg test site, where a single fiber optic cable attached to a data logger at one end is looped into a U-shape that extends to the bottom of the borehole. The other end of the cable returns to the ground surface where it continues on to the next borehole.

As shown in Figure 6, three DTS sensors (DTS-2, DTS-4, DTS-8) were placed into three of the boreholes containing heat exchangers (BHE-1, BHE-5, BHE-6). The rest of the DTS sensors were placed in monitoring boreholes in proximity to the BHE's. Because these measurements are continuous along the fiber optic cable, the temperature change can be analyzed with depth, giving valuable insight into the subsurface temperature profile around the heaters.
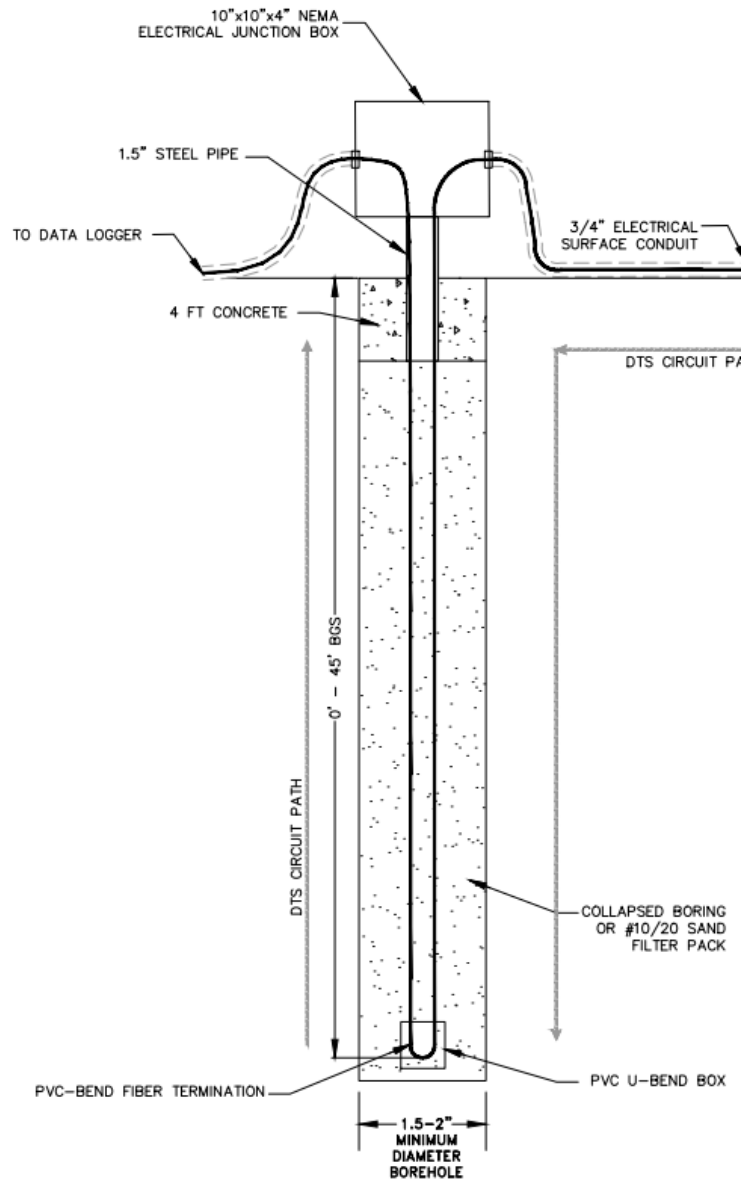
Fig. 7. Diagram of a DTS sensor installation (Arcadis U.S., Inc., 2021).

For example, Figure 8 shows a snapshot of the temperature-depth profile of all twelve DTS sensors on the Vandenberg test site at a moment in time. Among the twelve DTS sensors, temperatures near the ground surface vary between 15.5 and 16.5 ◦C before sharply rising and peaking at around 21 ◦C between the depths of 2 and 5 meters. Beneath this point, the temperatures appear to stabilize between 19.5 and 20.5 ◦C.

In addition to temperature-depth profiles, time series data can be extracted from any point along the fiber optic cable, giving valuable insight on subsurface temperature change with time. For example, Figure 9 shows how the temperature at three different depths along a single strand of the fiber optic cable changes with time.
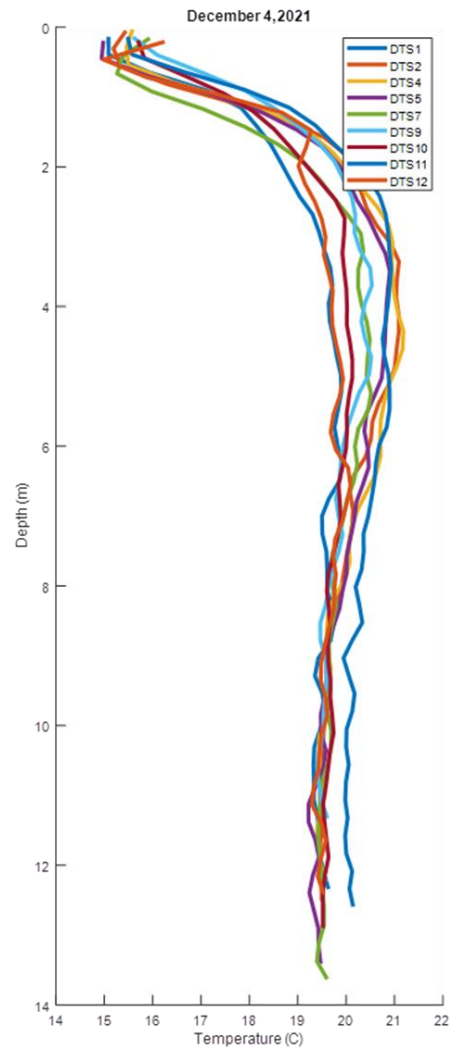
Fig. 8. Temperature-depth profile of the twelve DTS sensors at a moment in time.
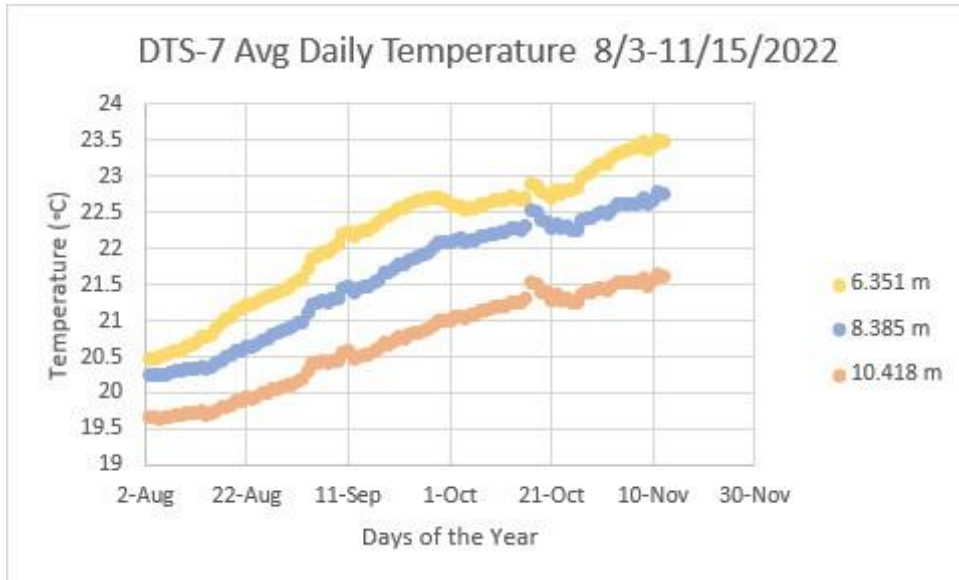
Fig. 9. Time series data extracted from three different depths along a DTS sensor.

4.2 Measured Hydrogeologic and Thermal Properties of the Test Site

The installation of the solar thermal remediation system at Vandenberg as well as the initial soil, moisture, thermal, and hydraulic testing of the field site was carried out by Arcadis, an engineering consulting company. In their initial laboratory report, a saturated thermal conductivity of 1.87 $\frac{W}{m \cdot C}$ and a porosity of 40.7% were determined from the field site. Table 2 lists depth-to-water measurements that were taken at a series of monitoring wells on the test site in a 1-year period between January of 2022 and January of 2023.

	TISR-1s	TISR-1d	TISR-2s	TISR-2d	TISR-3s	TISR-3d	TISR-4s	TISR-4d d	15-MW-8
Jan 2022 dtw (m)	7.17	6.98	7.17	7.46	7.24		7.02	6.98	
Sep 2022 dtw (m)	7.54	7.26	7.53	7.72	7.63	7.27	7.40	7.36	7.75
Jan 2023 dtw (m)	7.46	7.09	7.32	7.60	7.44	7.17	7.13	7.19	7.51
Avg dtw (m)	7.39	7.11	7.34	7.59	7.44	7.22	7.18	7.18	7.63

Table 2. Depth-to-water measurements from each monitoring well on the Vandenberg test site (Arcadis U.S., Inc., 2022).

With an average overall depth-to-water of 7.2 m, it is unlikely that the BHEs are completely submerged. Having been installed at a depth interval of 6.1 to 12.2 m, it is likely that the top meter or so of each heater is above the water table. The orientation of groundwater flow is assumed to be perpendicular to the shoreline Southwest of the test site. The bulk heat capacity is a critical parameter used by the analytical model to calculate the thermal diffusivity as well as the convective thermal velocity in projecting subsurface temperature change (see Equations 4 and 5). A summary of the hydraulic and thermal properties gathered from the Vandenberg solar thermal remediation test site are listed in Table 3:

Vandenberg Space Force Base Hydraulic and Thermal Properties	
Darcy Velocity	11 m/yr
Porosity	0.4
Thermal Conductivity	1.9 W/m°C
Bulk Heat Capacity	2.7E6 J/m^3°C

Table 3. A summary of the hydraulic and thermal properties gathered from the Vandenberg solar thermal remediation test site.

4.3 Determining Average Monthly Power Input

4.3.1 Methods

The first step in modeling the solar thermal remediation system at Vandenberg Space Force Base was to determine the average monthly power input from the solar panels to the BHE's. Raw BHE inlet and outlet temperature and flowrate data were obtained from system operations at the Vandenberg field site and used to calculate hourly heating rates using equation 14, where P is the power delivery (W), Q is the volumetric flowrate of the 50:50 glycol fluid $(\frac{m^3}{s})$, C_p is the fluid heat capacity $\left(\frac{J}{kg \cdot C}\right)$, ΔT is the temperature differential ($\circ$ C), and ρ is the fluid density $\left(\frac{kg}{m^3}\right)$.

$$P = QC_p\Delta T\rho \qquad \text{(Equation 14)}$$

The hourly heating rates were averaged over each month and divided by the number of BHE's to calculate average monthly heat flow per borehole (W). These values could then be compared to average monthly power rates predicted by the analytical model using the solar power calculator.

A global tilted irradiation of 6 $\frac{kWh}{m^2 day}$ was determined based off the test site's location and was used to predict average monthly power into the solar thermal remediation system using the solar heat flow calculator. Table 4 lists the inputs to the calculator:

Solar Heat Flow Calculator Input	
Collector Efficiency	0.405
Panel Collector Area	$4.89\ m^2$
Number of Collectors	8
Number of Boreholes	8
Latitude	40 degrees (N)
Longitude	-105 degrees (W)
Global Tilted Irradiation	$6\ \frac{kWh}{m^2 day}$

Table 4. Parameters used by the solar power calculator in the design tool to predict average monthly power to the Vandenberg solar thermal remediation system.

4.3.2 Results

Average monthly power values from the start of heating in June 2022 through early May of 2023 were calculated and varied between 164 and 361 watts per borehole, while the values predicted by the model ranged from 240 to 727 watts per borehole. Figure 10 shows the comparison between average power obtained from field data and estimated from the solar power calculator.
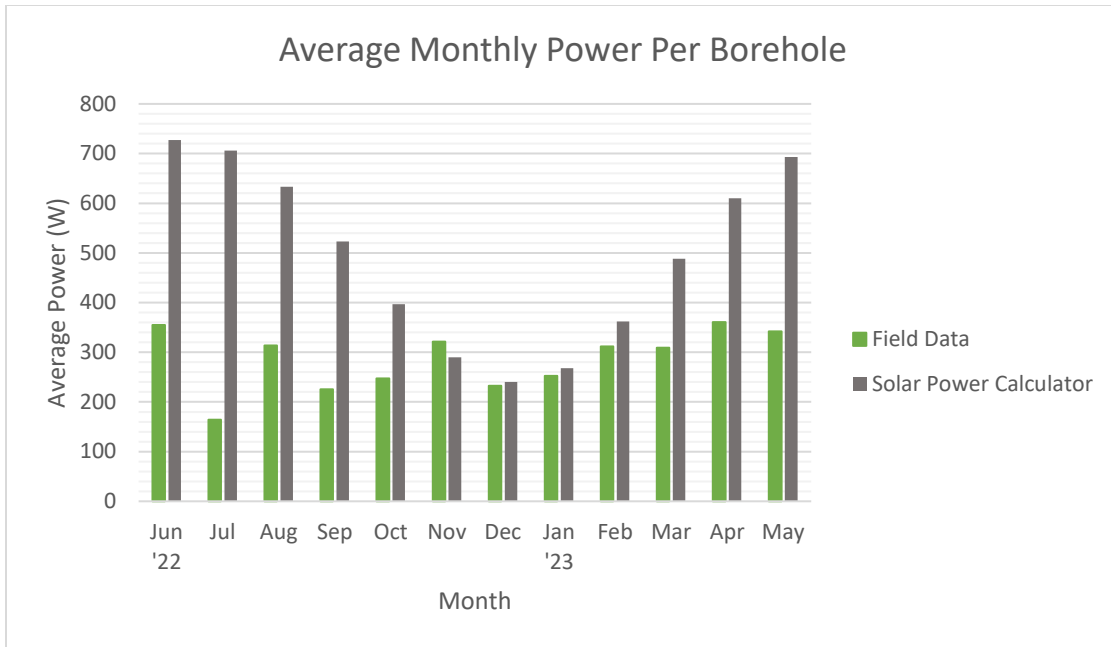
Fig. 10. Average monthly power per borehole comparison between field data and the solar power calculator.

While the heat flow calculator closely predicted average monthly power for the colder months of November through February, it overestimated the warmer months of March through October. It is suspected that this difference may be due to the climate of the coastal Pacific area being overcast during the start of heating in the Summer of 2022. The largest difference between actual power data and the model prediction was evident in July, when a massive electrical power outage was reported on the Vandenberg test site due to a missile explosion. Power delivery data that was observed from the test site's control system suggests that the site-wide power outage lasted from July 8th through July 28th, which prevented thermal power from entering all eight BHE's and is likely responsible for the low average power per borehole for the month of July.

4.4 Modeling the Vandenberg Test Site Using the Analytical Design Tool

4.4.1 Methods

The average monthly power values that were calculated from the start of heating in June through May of the following year from system operations data were input into the analytical model. Table 5 lists the average power values that were used to model the Vandenberg test site. After the first year of operation, an estimated power of 335 watts per borehole was used for July of every following year in the forward simulations.

Month	Watts Per Borehole
June 2022	355
July	164
August	313
September	225
October	247
November	322
December	232
January 2023	252
February	312
March	309
April	361
May	342

Table 5. Average monthly power values obtained from field data that were used to model the Vandenberg test site for the first year of operation.

Table 6 lists the thermal, hydraulic and heater parameters obtained in Sections 4.1 and 4.2 that were input into the analytical model. A background temperature of 0 degrees Celsius was chosen so that the model output would reflect only the change in temperature from ambient conditions.

Model Input	
Darcy Velocity	11 m/yr
Number of heaters	8
Background Temperature	0 ∘C
Porosity	0.4
Rock heat capacity	790 J/kg∘C
Rock grain density	2200 kg/m^3
Bulk heat capacity	2.7 x 10^6 $\frac{J}{m^3 \cdot C}$
Thermal Conductivity	1.9 W/m∘C
Heater length	6.1 m
Depth to top of heater	6.1 m

Table 6. The thermal, hydraulic and heater parameters used to model the Vandenberg test site.

The UTM coordinates of all eight heat exchangers and twelve DTS sensors on the Vandenberg site were also provided by Arcadis and used to create a local coordinate system of the field site. Figure 11 shows the layout of the modeled field site, with BHE-4 as the coordinate system's origin point. The BHEs are aligned into two rows of 3 and one row of 2 in the center of the array. They are roughly equally spaced from one another by about 5 meters, covering a total area of approximately 100 m^2. The distances between the DTS sensors and the BHEs are highly variable. DTS-2, 4, and 8 are placed in boreholes containing BHEs while DTS-3, 5, 6, 7, and 9 are in separate boreholes but still within the 100 m^2 perimeter of the BHE array. DTS-1, 10, 11, and 12 surround the western and southern perimeters of the BHE array and are over 8 meters from the nearest heat exchanger.
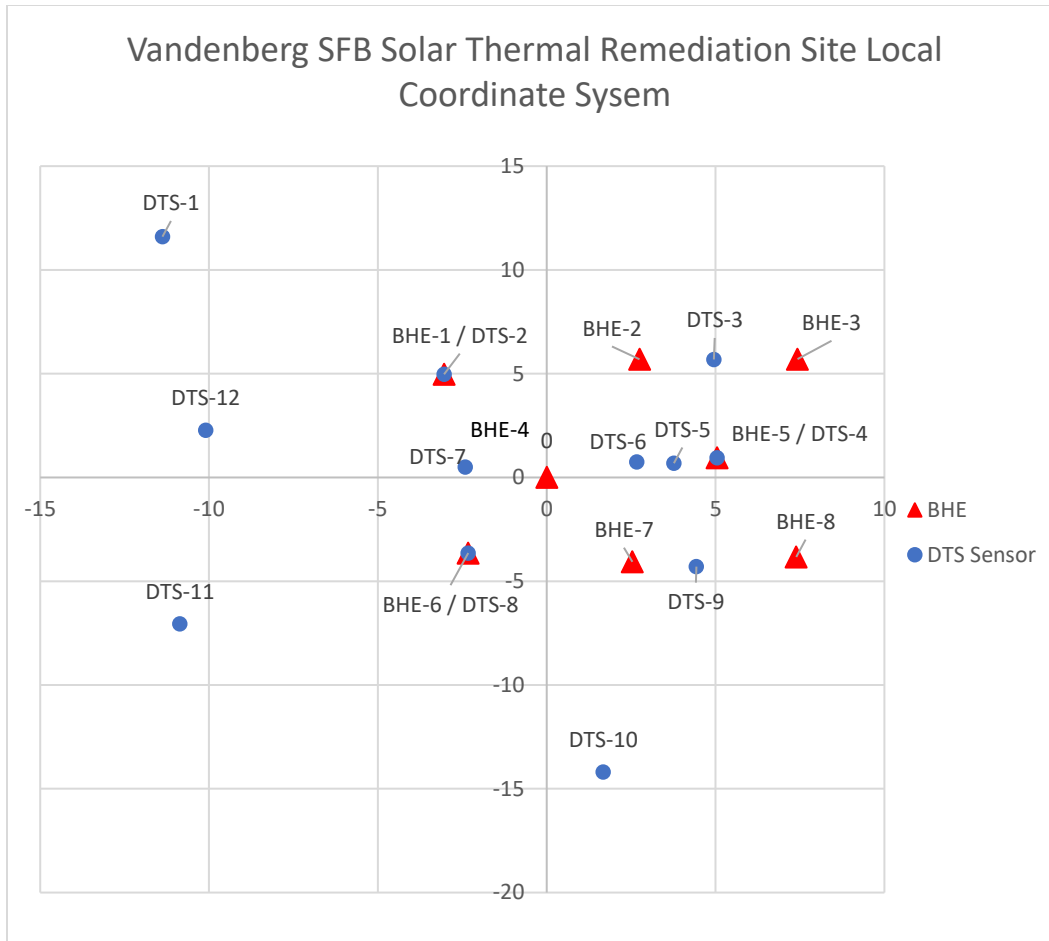
Fig. 11. Local coordinate system of the Vandenberg solar thermal remediation test site (m).

Because of their proximity to the BHEs, the coordinates for DTS-5, 7, and 9 were chosen as initial observation points in the model to compare to actual temperature change during early portions of the solar thermal remediation test. The DTS-3 and DTS-6 locations were excluded from the model after these sensors had failed early on during the test.

Six different depths were assigned to each XY observation point in the model and coincided with the depths at which temperature data were extracted from the DTS sensors on the field site, ranging from 5 to 10 meters. Table 7 summarizes the XYZ coordinates of each observation point at the DTS-5, DTS-7, and DTS-9 locations.

Hourly temperature time series data was sampled from DTS-5, 7, and 9 on the Vandenberg field site at each of the indicated depths listed in Table 7. Figure 12 shows an example of temperature data that was extracted from a single point along a DTS cable.

X obs	Y obs	Z obs	ID
3.77	0.69	5.33	DTS-5
3.77	0.69	6.35	DTS-5
3.77	0.69	7.37	DTS-5
3.77	0.69	8.39	DTS-5
3.77	0.69	9.40	DTS-5
3.77	0.69	10.42	DTS-5
-2.41	0.50	5.21	DTS-7
-2.41	0.50	6.22	DTS-7
-2.41	0.50	7.24	DTS-7
-2.41	0.50	8.26	DTS-7
-2.41	0.50	9.27	DTS-7
-2.41	0.50	10.29	DTS-7
4.43	-4.30	5.11	DTS-9
4.43	-4.30	6.13	DTS-9
4.43	-4.30	7.15	DTS-9
4.43	-4.30	8.16	DTS-9
4.43	-4.30	9.18	DTS-9
4.43	-4.30	10.20	DTS-9

Table 7. Observation locations modeling the DTS sensors in the analytical model's domain.

Date, Time	Time, hours since start	Time, hours into year	Time, days into year	Temperature (C)
5/21/2022 0:00	0			
8/3/2022 20:15	1796.262659	5180.262659	215.8442775	21.648563
8/3/2022 21:15	1797.263792	5181.263792	215.8859913	21.527563
8/3/2022 22:15	1798.264923	5182.264923	215.9277051	21.534563
8/3/2022 23:15	1799.265969	5183.265969	215.9694154	21.600563
8/4/2022 0:16	1800.267123	5184.267123	216.0111301	21.602563
8/4/2022 1:16	1801.268314	5185.268314	216.0528464	21.669563

Fig. 12. Hourly temperature data extracted from a single point of a DTS sensor.

The raw temperature data is given in terms of hours since the start of data collection, which began on May 21, 2022; 10 days before heating began on June 1, 2022. Because the analytical design tool computes temperature change relative to days of the calendar year, the sampled time data was converted to days into the year. As shown in Figure 12, all temperature data that were recorded before 8:15 PM on August 3, 2022 were lost due to the mentioned electrical power outage that occurred in July 2022. This meant that all of the data that recorded ambient conditions in the subsurface before heating began were unavailable, and so an average ambient temperature had to be estimated using early portions of the temperature data that were extracted from monitoring locations distant to the BHEs.

To do this, averaged daily temperature data extracted from depths ranging between 5 and 12 meters from DTS-1, 10, and 11 were examined from August 3 to August 7, 2022. Figure 13 shows the temperature data at DTS-1 during the first 5 days of data collection. Between the depths of 6 and 11 meters, temperatures initially ranged from 18.4 to 18.7 ◦C on August 3rd and remained relatively stable for the following 5 days.
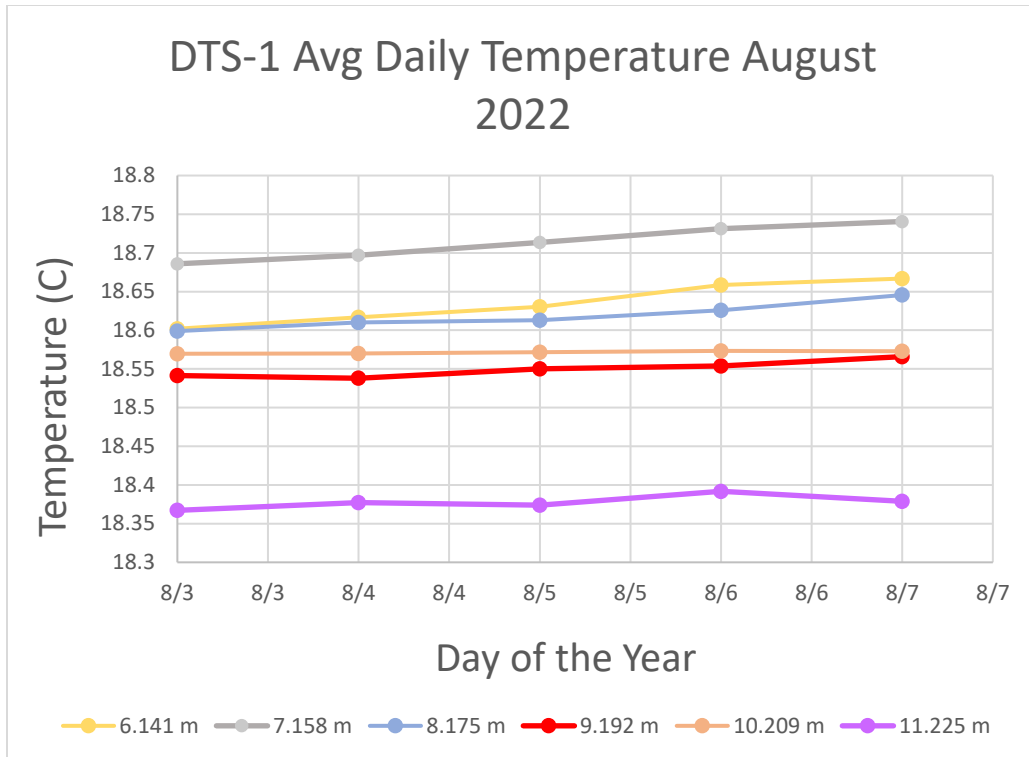
Fig. 13. DTS-1 average daily temperature at 6 different depths at the beginning of
on-site data collection in early August 2022.

Similar initial temperature ranges were observed at DTS-10 and DTS-11. Figure 14

shows temperature data at DTS-10 during the first 5 days of data collection. Between the depths

of 5 and 11 meters, temperatures initially ranged from 18.5 to 18.7 ∘C on August 3rd and

gradually increased by just 0.1 ∘C after 3 days. Figure 15 shows temperature data at DTS-11

where temperatures also increased by 0.1 ∘C after 3 days of data collection and initially ranged

from 18.7 to 18.9 ∘C, just slightly higher than the temperature ranges observed at DTS-1 and

DTS-10.
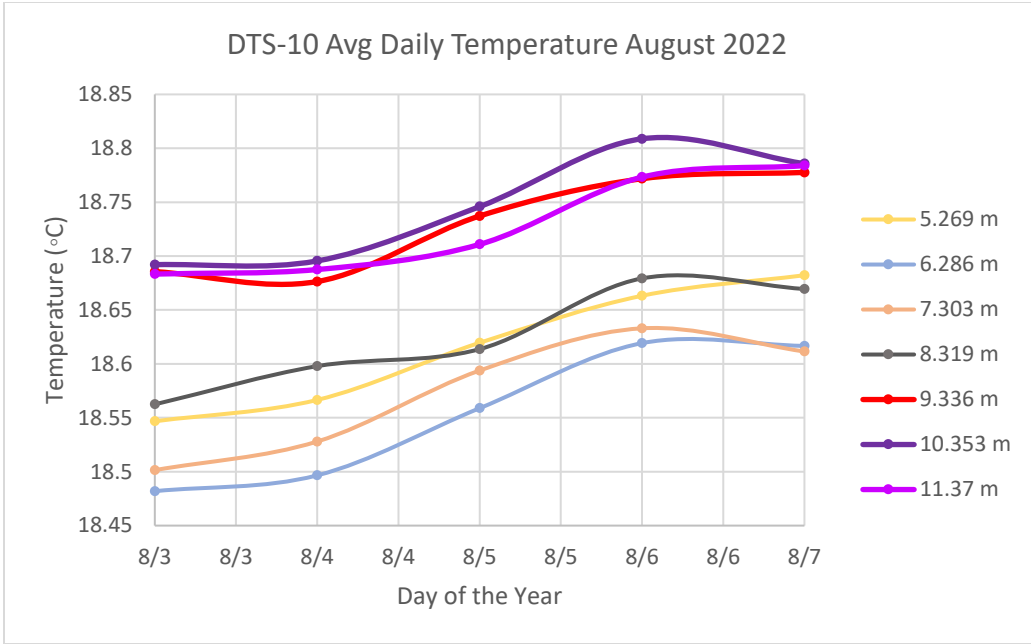
Fig. 14. DTS-10 average daily temperature at 7 different depths at the beginning of on-site data collection in early August 2022.
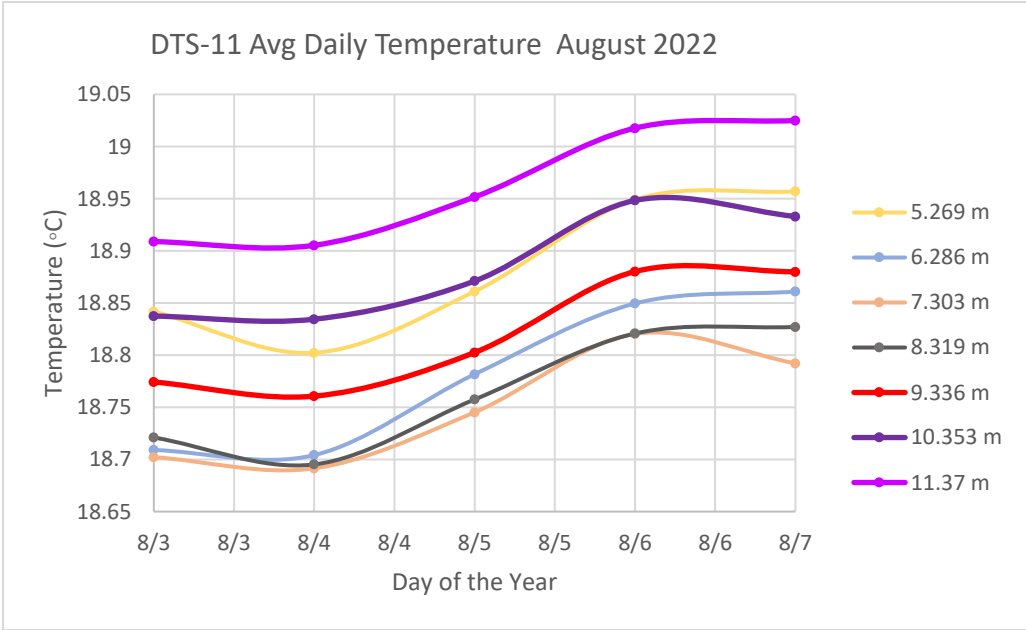
Fig. 15. DTS-11 average daily temperature at 7 different depths at the beginning of on-site data collection in early August 2022.

An average ambient temperature of 18.5 ∘C was chosen based off early temperature data from DTS-1,10, and 11. This value was assumed to be constant throughout the subsurface in the model prior to heating and was used as the baseline temperature for computing temperature change with the DTS temperature data. Figure 16 shows how the average ambient subsurface temperature is subtracted from each data point to compute the temperature change, ΔT. These values were then averaged over each day to obtain average daily temperature change, which could then be compared to temperature change predicted by the analytical design tool.

Time, days into year	Temperature (C)	avg ambient T	ΔT	Time, days into year	Avg Daily ΔT
215.8442775	21.648563	18.5	3.148563	216	3.086021333
215.8859913	21.527563	18.5	3.027563	217	3.139521333
215.9277051	21.534563	18.5	3.034563	218	3.181604667
215.9694154	21.600563	18.5	3.100563	219	3.231354667
216.0111301	21.602563	18.5	3.102563	220	3.295979667
216.0528464	21.669563	18.5	3.169563	221	3.426729667

Fig. 16. Workflow of the hourly temperature data being subtracted by the average ambient temperature and then averaged over each day to obtain average daily temperature change data.

The average temperature change data that were gathered from DTS-5, 7, and 9 were plotted from August 4, 2022 until all three sensors failed in late January 2023. Figure 17 shows the average daily temperature change that was sampled from DTS-5 in the depth range of 5 to 10 meters during this time. After the DTS system on the Vandenberg test site had been recovered on August 3rd, temperatures at DTS-5 had risen between 3 and 4.3 ∘C since the start of heating on June 1st. They continued to rise and eventually reached peak temperature increases between 5 and 7 ∘C on September 11th before plateauing through the following 13 days.
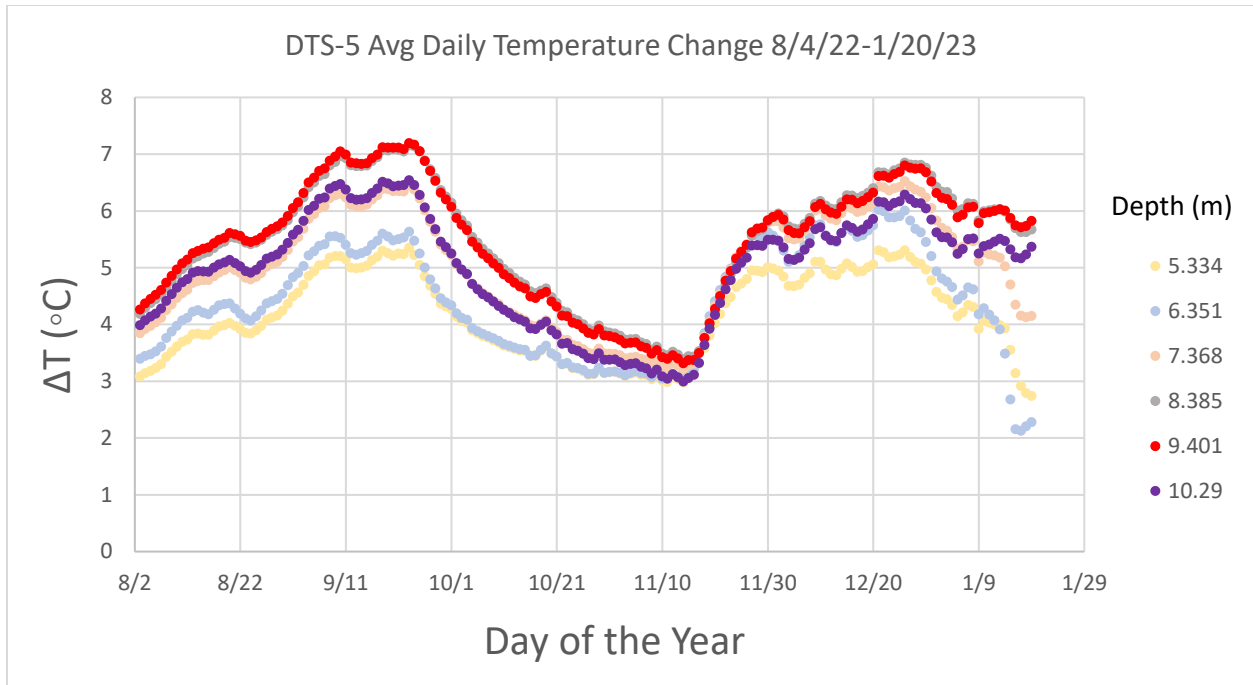
Fig. 17. Average daily temperature change sampled from 6 different depths along DTS-5 on the Vandenberg test site from August 4, 2022 to January 20, 2023.

On September 24th, BHE-3 and BHE-5 lost thermal power on the test site, causing a major decline in temperature change at all six DTS-5 observation points until power was eventually restored to both heaters on November 14th. Figure 18 shows the drop in temperature (∘C) between the times of thermal power loss and restoration at every depth coinciding with the interval in which the BHEs were installed between 6 and 12 meters. Complications involving the inlet valves prevented hot fluid from entering these heaters, effectively shutting them off.

The restoration of these two heaters on November 14th caused a second wave of temperature rise at every DTS-5 observation point, eventually reaching peak temperature changes of 5.2 to 6.8 ∘C in late December before entering a second period of rapid temperature decline through the end of available DTS data in late January 2023.

The exact cause of the temperature decline in late December is unknown, however it is suspected that it may have been caused by a combination of severe rainstorms and irregularly cold air temperatures that were reported at the Vandenberg Space Force Base test site at the time. As shown in Figure 17 and Figure 18, sharp decreases in temperature are only apparent at depths shallower than 7.4 meters.
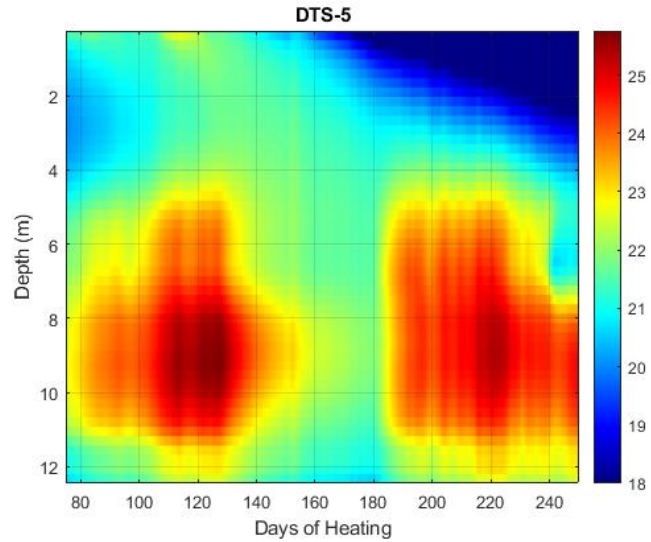
Fig. 18. Total depth profile of DTS-5 showing 2 periods of rapid temperature (◦C) decline. One as a result of the BHE power outages in September (center) and a second in late December that only appears to have affected temperatures at shallow depth (upper right corner of heated zone).

Observation points below this depth appear to be much less affected, so it is unlikely that this temperature drop was a result of another BHE thermal power outage. Additionally, similar cooling patterns were detected in the sampled temperature data from DTS-7 and DTS-9 at the same depth interval at similar times.

Figure 19 shows the average daily temperature change that was sampled from DTS-7 in the depth range of 5 to 10 meters. After the DTS system on the Vandenberg test site had been recovered on August 3rd, temperatures at DTS-7 had risen between 1.2 and 2 ◦C since the start of heating on June 1. They continued to rise and eventually reached peak temperature increases between 3.7 and 5.6 ◦C before plateauing in early December. Similar to temperature data

sampled from DTS-5, sharp temperature decreases between the depths of 5 and 7 meters in late December are also apparent in DTS-7.
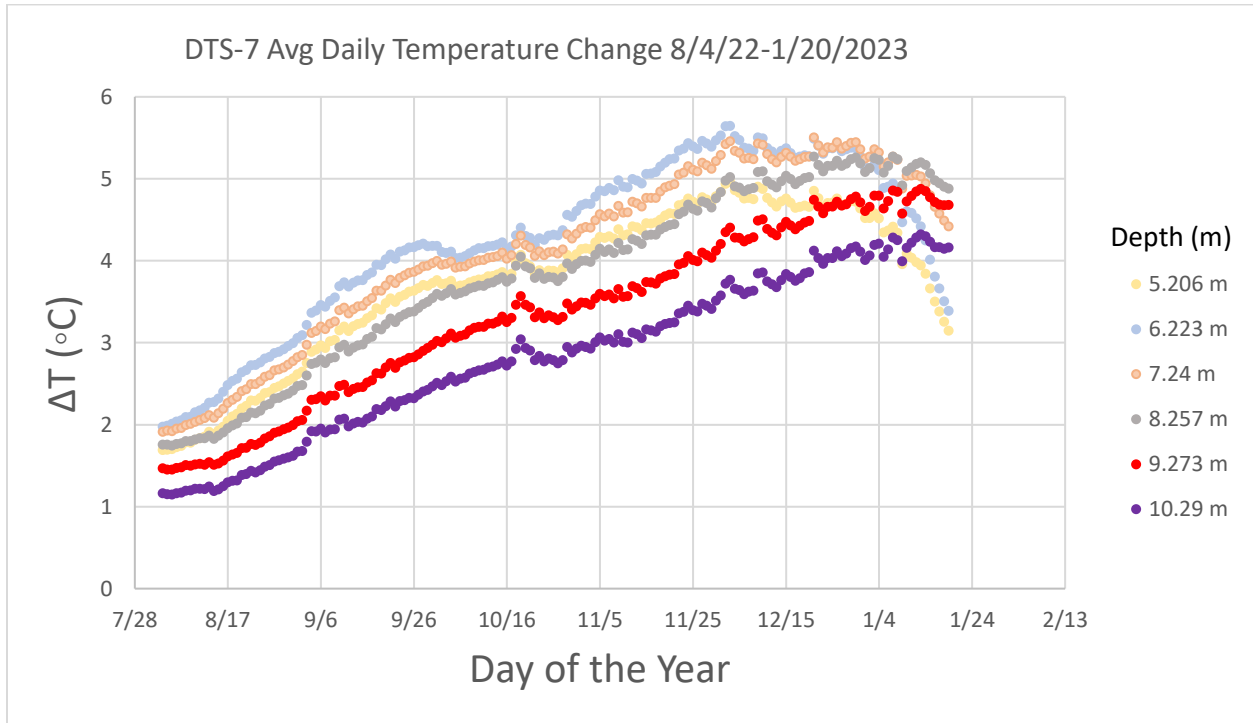
Fig. 19. Average daily temperature change sampled from 6 different depths along DTS-7 on the Vandenberg test site from August 4, 2022 to January 20, 2023.

Figure 20 shows the average daily temperature change that was sampled from DTS-9 in the depth range of 5 to 10 meters. After the DTS system on the Vandenberg test site had been recovered on August 3rd, temperatures at DTS-9 had risen between 1.1 and 3 ∘C since the start of heating on June 1. They continued to rise and eventually reached peak temperature increases between 3.8 and 6.4 ∘C before plateauing in early December. Again, the same pattern that is evident in both DTS-5 and DTS-7 is repeated in DTS-9 where much larger drops in temperature are apparent at shallower depths of 5 to 7 meters in late December.
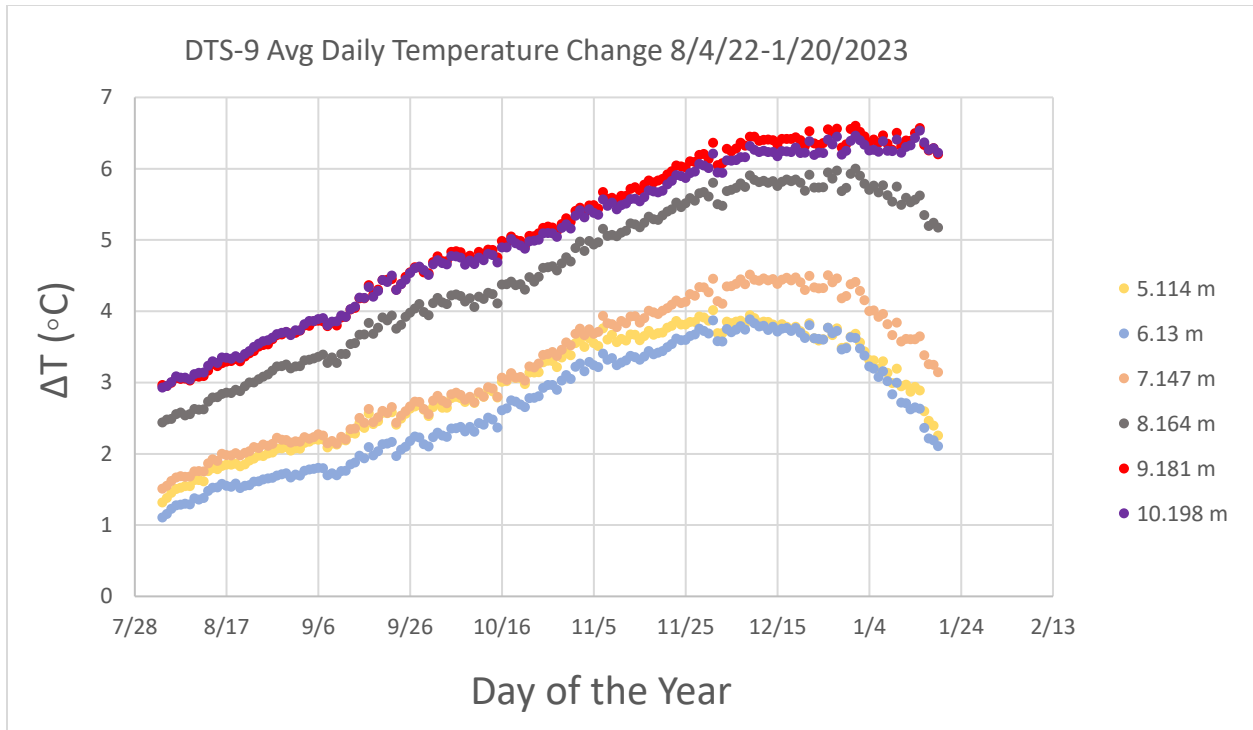
Fig. 20. Average daily temperature change sampled from 6 different depths along DTS-9 on the Vandenberg test site from August 4, 2022 to January 20, 2023.

Unlike DTS-5, the average daily temperature change profiles for DTS-7 and DTS-9 don't appear to have been affected by the thermal power outages to BHE-3 and BHE-5 in late September through mid-November. This is most likely because DTS-5 is in much closer proximity to both BHEs and DTS-7 and DTS-9 may have not experienced the full effects of the power outages as a result. To account for this particular power outage in the analytical design tool, adjustments were made to the average monthly power input section for each BHE. This was done by assigning power factors of 0 for BHE-3 and BHE-5 for the months of October and November of the first year of heating. The rest of the heaters were assigned factors of 1.33 for those same months to account for the total power being divided into only 6 heaters instead of 8.

4.4.2 Results (pre-calibration)

The time series component of the analytical design tool was run using the initial reported parameters summarized in Table 6 from the start of heating on June 1, 2022 to the end of January 2023 at every observation point indicated in Table 7. The solution was evaluated at daily intervals and the resulting simulated temperature change output was compared to the average daily temperature change data sampled from the Vandenberg test site. Figure 21 shows this temperature change comparison for the observation points placed at DTS-5.
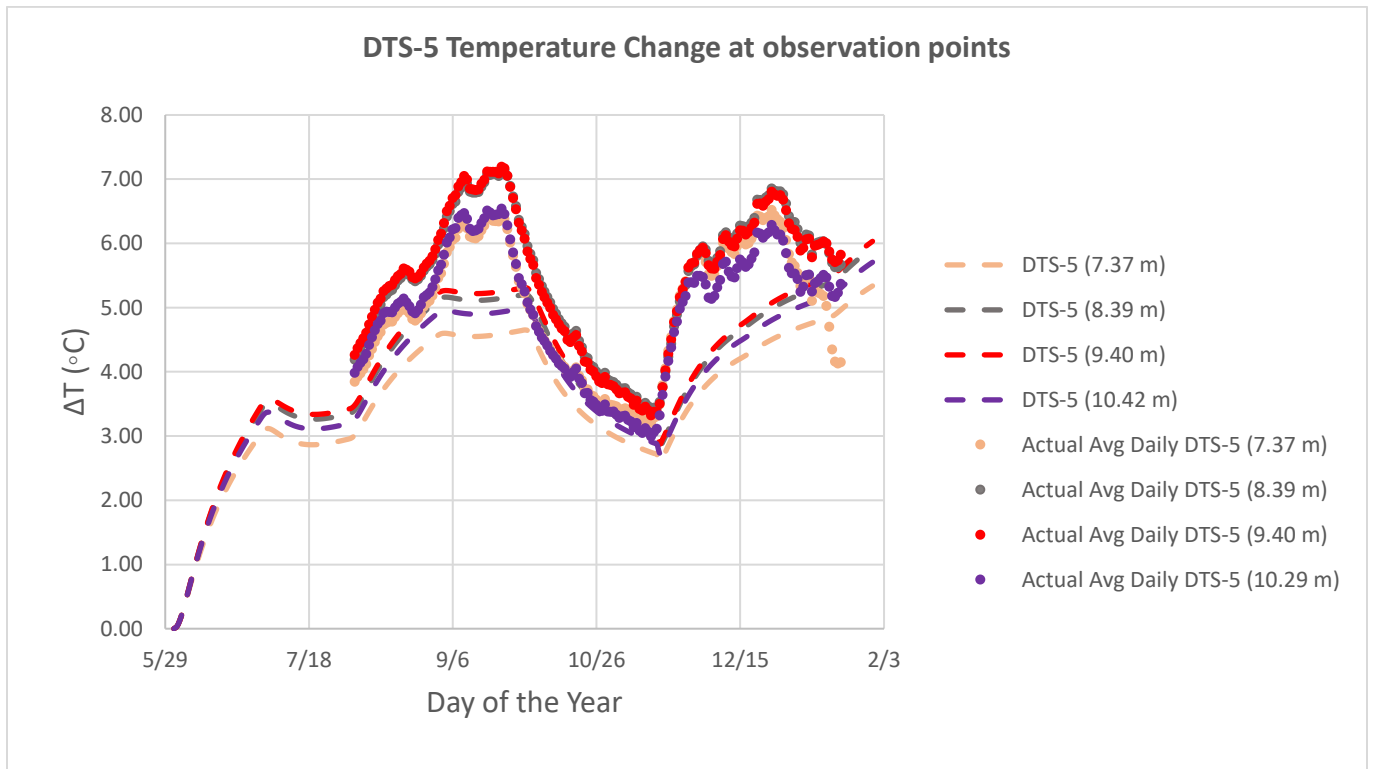
Fig. 21. Simulated temperature change from the analytical design tool (dashed lines) compared with average daily temperature change data (dotted points) at DTS-5 observation points between depths of 7 and 10 meters.

The analytical design tool slightly underestimates the first period of temperature rise by 1 to 2 °C from the start of temperature data collection on August 3rd to the BHE thermal power loss on September 24th. From October to the restoration of thermal power to the BHEs in mid-November, the overall fit of the analytical prediction greatly improves, as the model appears to have successfully accounted for the thermal power losses to BHE-3 and BHE-5. However, the analytical model underestimates the second period of temperature rise after November 15th through December, after which the overall fit to the temperature data significantly degrades in January 2023 where a second period of rapid temperature decline occurred.

Figure 22 shows the comparison between the temperature change simulation and average daily temperature change data at DTS-7.
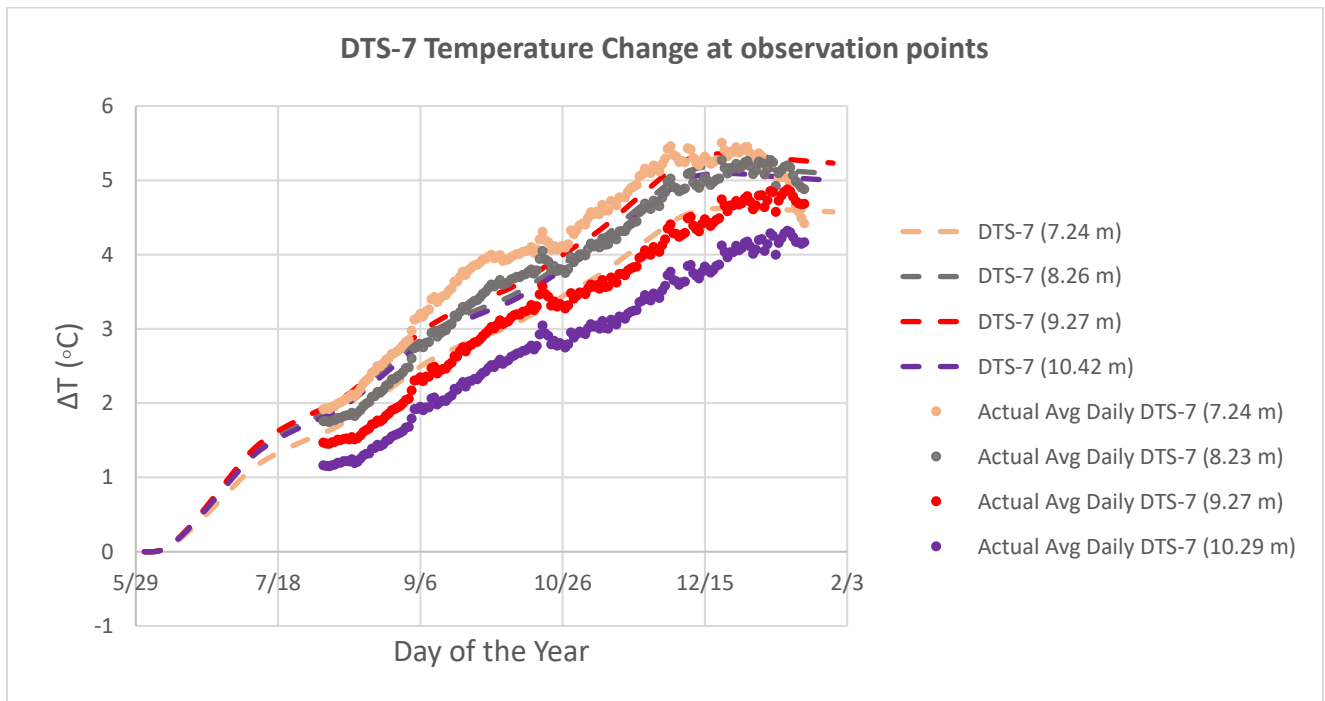
Fig. 22. Simulated temperature change from the analytical design tool (dashed lines) compared with average daily temperature change data (dotted points) at DTS-7 observation points between depths of 7 and 10 meters.

The analytical design tool sufficiently predicts temperature change at the DTS-7 observation points from the start of temperature data collection on August 3rd through the end of December, most notably at the 8.26-meter point. The greatest difference in temperature change between the two datasets is evident at the 7-meter observation point, where the model slightly underestimates temperature change by as much as 1 ∘C. Conversely, the model slightly overestimates temperature by approximately 1 ∘C for the 9 and 10-meter observation points. Like DTS-5, agreement between the model prediction and temperature data at the 7 and 8-meter observation points significantly declines after the rapid temperature decline in January.

Figure 23 shows the comparison between the temperature change simulation and average daily temperature change data at DTS-9.
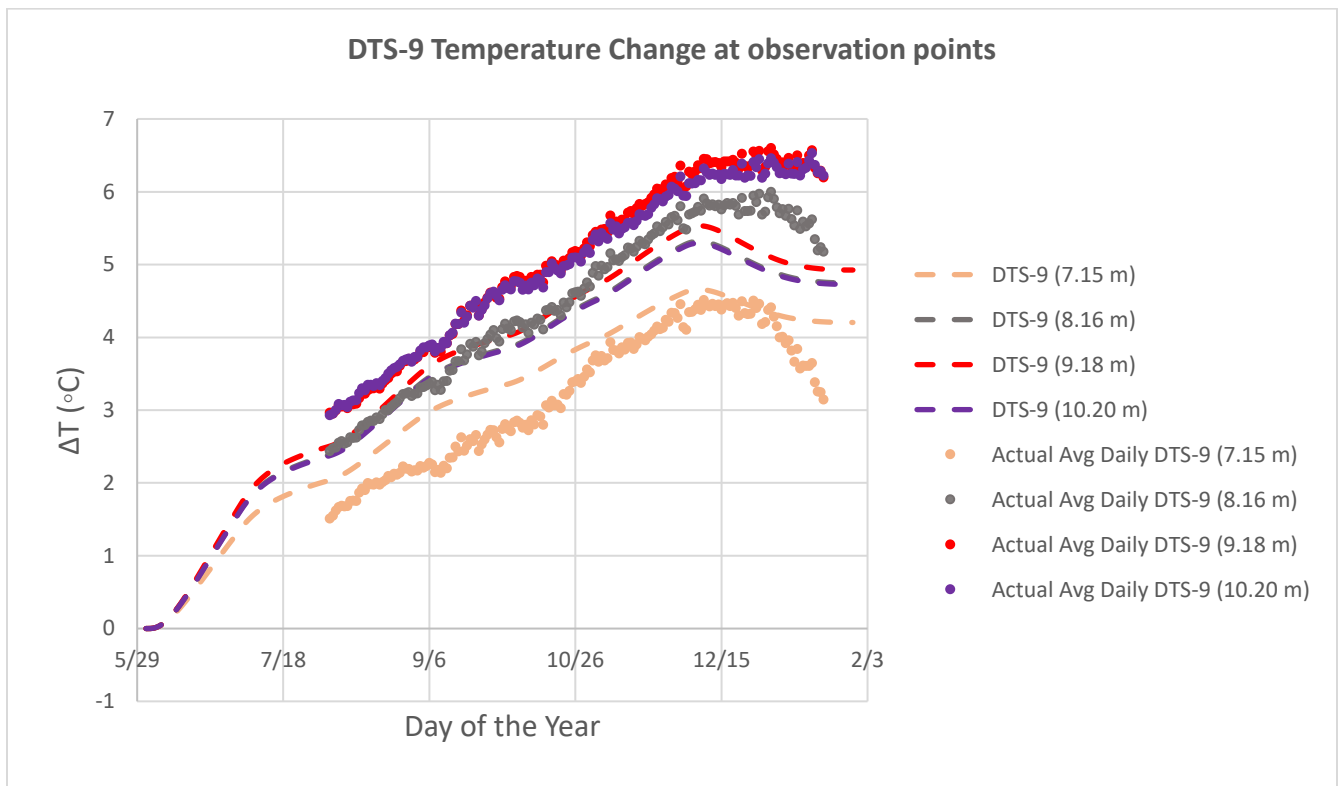
Fig. 23. Simulated temperature change from the analytical design tool (dashed lines) compared with average daily temperature change data (dotted points) at DTS-9 observation points between depths of 7 and 10 meters.

The analytical design tool sufficiently predicts temperature change at the DTS-9 observation points from the start of temperature data collection on August 3rd through November. Conversely from DTS-7, the model slightly underestimates temperature change at the 8, 9, and 10-meter observation points by 1 ◦C, and overestimates temperature change at the 7-meter observation point for DTS-9. Additionally, similar to DTS-5 and DTS-7, agreement between the model prediction and sampled temperature change data severely degrades exclusively at shallow depth (7 meters in Figure 36) after late December where the rapid temperature decline has been recorded by all three DTS sensors.

The results from Section 4.2 suggest that the analytical design tool can reasonably predict the overall trend of temperature change within the targeted heating zone of 7 to 10 meters beneath the ground surface from August through December of the 1st year of heating. However, the model was not able to account for the substantial temperature decline in January, which is where the greatest degree of error between the datasets occur. The model generally underestimated temperature change at the DTS-5 and DTS-9 observation points and overestimated temperature change at the DTS-7 observation points. The only exception to this was evident at the 7-meter depths, where temperature change was underestimated at DTS-7 and overestimated at DTS-9.

It's possible that some disagreement between the model and the field data is being caused by heterogeneity with depth in the subsurface. Even small amounts of variability in subsurface permeabinty can cause significice uncertainty in the size and distribution of the heat plume that moves with groundwater flow (Ferguson, 2007). The thermal parameters that were measured from the field site were expected to be relatively constant, as these values won't typically vary with grain size. However, the hydraulic properties of the soil, particularly the hydraulic

conductivity which determines the groundwater velocity, can vary by many orders of magnitude and is influenced by changes in groundwater temperature (Fetter, 2001). For this reason, the analytical model was re-run using a range of different groundwater velocities in an effort to enhance the agreement between the model simulation and the temperature data from the site.

4.5 Model Calibration Using a Range of Groundwater Velocities

4.5.1 Methods

A range in groundwater velocity between 3 and 15 m/yr was chosen to calibrate the analytical model to the field site temperature data.

A minimum groundwater velocity of 3 m/yr was chosen because below this value, the convective component simulated by the model is negligible. As shown in Figure 24, the simulated temperature contours from using a groundwater velocity of 1 m/yr remain evenly spaced and circular after 5 years of heating, indicating that the groundwater velocity is slow enough that any heat transport by convection has become relatively insignificant compared to conduction.
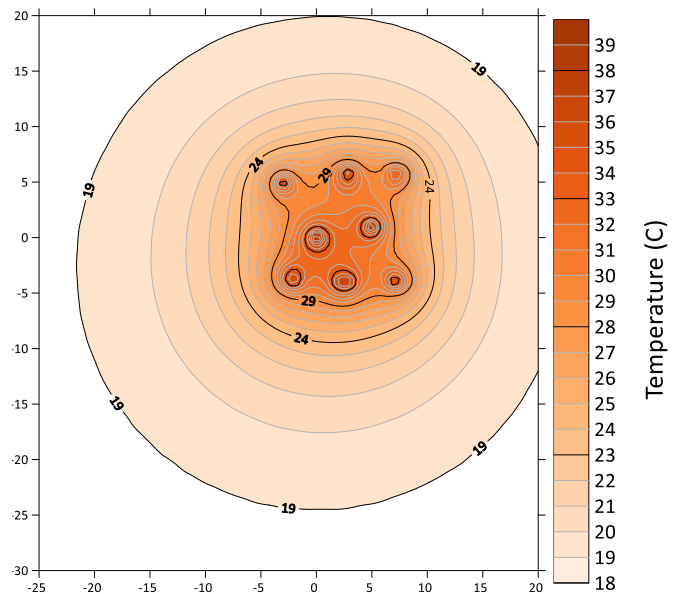
Fig. 24. Simulated temperature distribution after 5 years of heating using a groundwater velocity of 1 m/yr and a background temperature of 18.5 ∘C.

45

A maximum groundwater velocity of 15 m/yr was chosen because after this point, the effects of convection are extreme compared to field data. Figure 25 shows the simulated temperature distribution with a groundwater velocity of 17 m/yr after 5 years of heating. The higher groundwater velocity causes the predicted temperature contours to be stretched out in the indicated direction of groundwater flow, simulating a high-velocity heat plume.

The faster rate of colder groundwater (18.5 °C) entering the solar thermal remediation system from the Northeast causes a significant loss in temperature due to heat dissipation from the BHEs.
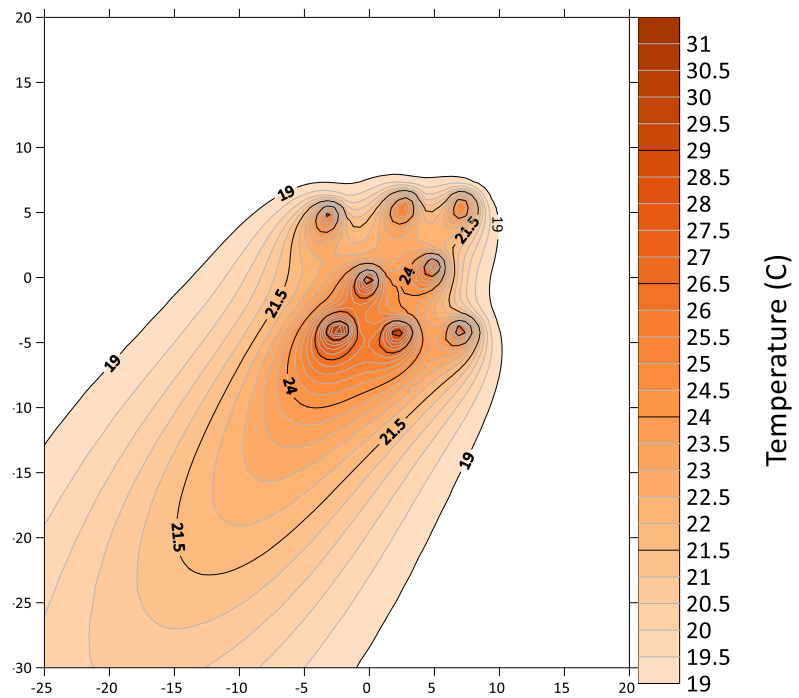
Fig. 25. Simulated temperature distribution after 5 years of heating using a groundwater velocity of 17 m/yr and a background temperature of 18.5 °C.

For two of the three observation locations, it was observed that this reduction in temperature as a result of increased groundwater velocity noticeably degraded the agreement between the model simulation and field data when using velocities greater than 8 m/yr. A maximum value of 15 m/yr was therefore used for the model calibration.

The agreement between the model simulation and field data was assessed for each groundwater velocity in the indicated range by calculating the coefficient of determination (R^2) at each observation point of DTS-5, DTS-7, and DTS-9. These were then compared with each other, along with that of the initial estimate of 11.13 m/yr that was used to generate the early temperature simulations shown in Section 4.4.2.

The coefficient of determination measures the extent that a model can predict actual observed values based on the distribution of total variation. It is the difference of 1 and the quotient of the sum of squares of residuals over the total sum of squares:

$$R^2 = 1 - \frac{RSS}{TSS} \qquad \text{(Equation 15)}$$

The sum of squares of residuals (RSS) is the sum of the differences between the actual observed values and the model prediction at every time, squared:

$$RSS = \sum (Y - \hat{Y})^2$$

The total sum of squares is the sum of the differences between the actual observed values and the mean actual observed value at every time, squared:

$$TSS = \sum (Y - \bar{Y})^2$$

Equation 15 can then be rewritten as:

$$R^2 = 1 - \frac{\sum (Y - \hat{Y})^2}{\sum (Y - \bar{Y})^2}$$

For a given range of data points, the model simulation will have a strong correlation to field data when the sum of squares of residuals is much lower than the respective total sum of squares. This means that the total variation of the model simulation from field data will be much lower than the total variation of the field data from the mean and as $\left(\frac{RSS}{TSS}\right)$ approaches a value of 0, R^2 approaches a value of 1.

4.5.2 Results

The coefficient of determination was calculated for 6 different model simulations that were generated by the analytical design tool using different groundwater velocities between 3 and 15 m/year at 4 different depths within the targeted heating zone of 7 to 10 meters below the ground surface. Table 8 shows the R^2 results for each observation point at the DTS-5 location where the initial model simulation that produced the results in section 4.2.2 are highlighted in grey.

DTS-5 Observation Points	R^2 3 m/yr	R^2 5 m/yr	R^2 8 m/yr	R^2 11.13 m/yr	R^2 13 m/yr	R^2 15 m/yr
7.37 m	0.16	0.09	-0.11	-1.17	-0.85	-1.21
8.39 m	0.25	0.21	0.10	-0.85	-0.54	-0.91
9.40 m	0.33	0.30	0.24	-0.63	-0.32	-0.66
10.42 m	0.43	0.42	0.39	-0.42	-0.10	-0.39
Avg	0.29	0.26	0.16	-0.77	-0.45	-0.79

Table 8. Coefficient of determination (R^2) calculated for 6 model simulations using different groundwater velocities at the DTS-5 observation location.

At the DTS-5 observation location, the calculated R^2 values at all 4 depths for the initial model simulation of 11.13 m/yr as well as those of 13 and 15 m/yr are all negative. The variation of the model prediction from the field data using these velocities is high enough that the residual sum of squares has surpassed the total sum of squares, which causes negative R^2 values and suggests a poor fit between the datasets. The agreement between the model prediction and field data improved at all four observation points after reducing the groundwater velocity from the initial value of 11.13 m/yr. The highest average R^2 value was calculated for the model simulation that used a velocity of 3 m/yr.

Table 9 shows the R^2 results for each observation point at the DTS-7 location. Adjusting the groundwater velocity had little effect on the agreement between the model simulation and field data for these observation points compared to the DTS-5 location. The average R^2 value for all four depths was slightly reduced after increasing and decreasing the groundwater velocity from 11.13 m/yr.

DTS-7 Observation Points	R^2 3 m/yr	R^2 5 m/yr	R^2 8 m/yr	R^2 11.13 m/yr	R^2 13 m/yr	R^2 15 m/yr
7.24 m	0.36	0.18	0.54	-0.08	0.37	-0.60
8.26 m	0.96	0.94	0.96	0.87	0.97	0.62
9.27 m	0.61	0.77	0.40	0.89	0.60	0.92
10.29 m	-0.12	0.19	-0.50	0.47	-0.13	0.75
Avg	0.45	0.52	0.35	0.54	0.45	0.42

Table 9. Coefficient of determination (R^2) calculated for 6 model simulations using different groundwater velocities at the DTS-7 observation location.

Table 10 shows the R^2 results for each observation point at the DTS-9 location. Like DTS-7, adjusting the groundwater velocity also had little effect on the agreement between the model simulation and field data for these observation points. The average R^2 value for all four depths was reduced after increasing the groundwater velocity from 11.13 m/yr.

DTS-9 Observation Points	R^2 3 m/yr	R^2 5 m/yr	R^2 8 m/yr	R^2 11.13 m/yr	R^2 13 m/yr	R^2 15 m/yr
7.15 m	0.04	-0.22	0.39	0.40	0.82	0.71
8.16 m	0.92	0.84	0.99	0.97	0.72	0.75
9.18 m	0.96	0.96	0.91	0.87	0.33	0.42
10.20 m	0.90	0.94	0.80	0.77	0.06	0.18
Avg	0.71	0.63	0.77	0.75	0.48	0.52

Table 10. Coefficient of determination (R^2) calculated for 6 model simulations using different groundwater velocities at the DTS-9 observation location.

Average R^2 was slightly reduced after decreasing the groundwater velocity, although the simulation that was run using an 8 m/yr velocity slightly improved by 2% from the initial model prediction. Interestingly, high R^2 values were calculated at shallow depths (7.15 m and 8.16 m) for the two highest groundwater velocities (13 m/yr and 15 m/yr), which wasn't evident at either DTS-5 or DTS-7.

For all three observation locations DTS-5, DTS-7, and DTS-9, the model simulations that used higher groundwater velocities than the initial simulation tended to have the greatest overall error. Smaller velocities had a definitive impact on the DTS-5 observation points because R^2 increased for every depth at each reduction in velocity (Table 8). However, adjusting the groundwater velocity had very little impact on improving the agreement between model simulations and field data at the DTS-7 and DTS-9 observation locations. These locations still

retained average R^2 values between 0.5 and 0.8, so most of the model simulations generated by the analytical design tool were able to reasonably predict temperature change during the heating test on Vandenberg SFB.

The analytical model was unable to resolve the high degree of error that was observed at the 7-meters depth points in all three observation locations with exception to the use of high velocities at DTS-9, where R^2 values of 0.71 and 0.82 were calculated. At this depth, the model tended to underestimate temperature change for DTS-5 and DTS-7, and overestimate temperature change for DTS-9. This could be explained by the fact that the 7-meter observation point at the DTS-9 location sits just 0.05 meters above the average depth-to-water that was reported for the test site . It's possible that this observation point is in fact above the water table and thus receives less heat on account of the lower thermal conductivity of partially saturated soil. Because the model's domain is assumed to be completely saturated, the analytical design tool is prone to overestimating temperature change at shallow depths above the water table in the vadose zone.

Despite the insignificant effects that decreasing the groundwater velocity in the analytical model had on the DTS-7 and DTS-9 locations, the simulation that was run using a velocity of 3 m/yr had the highest overall agreement for the three observation locations and was used for all the following simulations in this work. Figures 26, 27, and 28 show time series comparisons between field data and model simulations using the adjusted groundwater velocity of 3 m/yr.
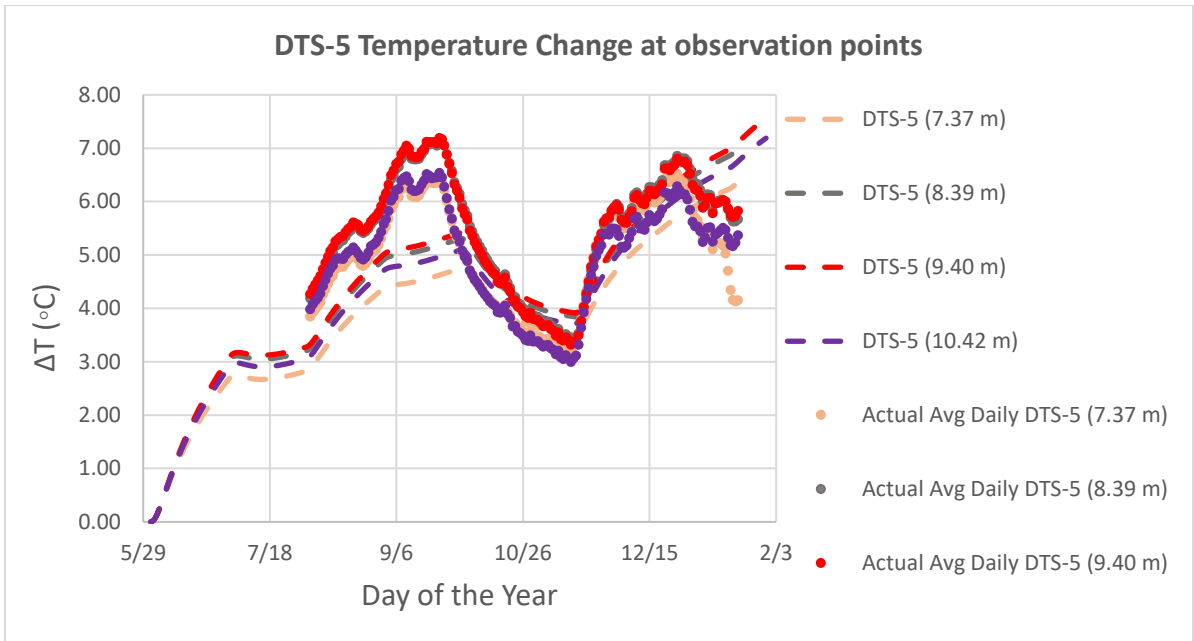
Fig. 26. Simulated temperature change from the analytical design tool using an adjusted groundwater velocity of 3 m/yr (dashed lines) compared with field data (dotted points) at DTS-5.
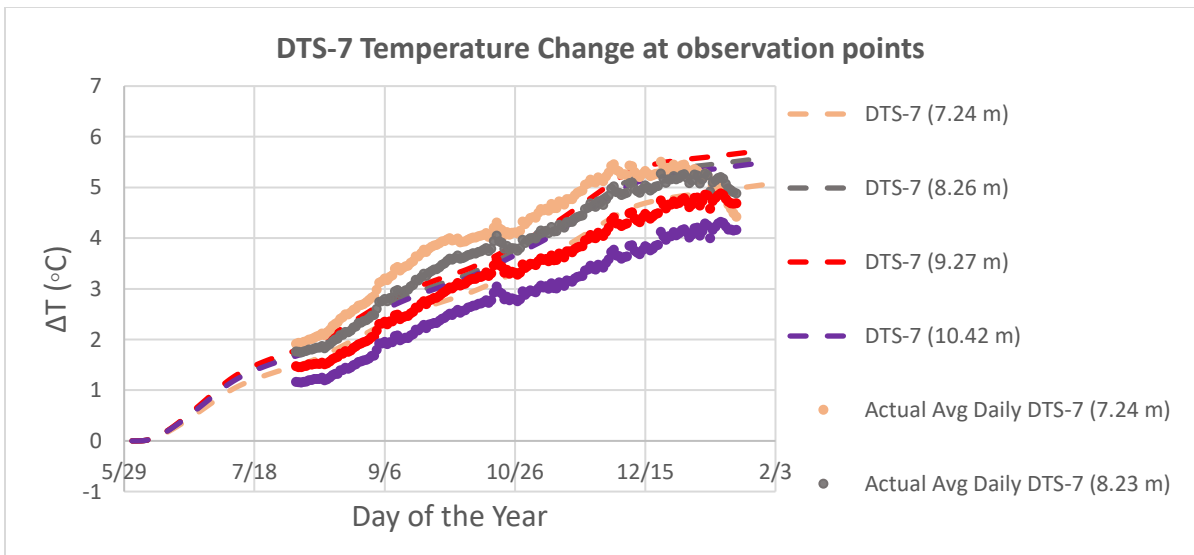
Fig. 27. Simulated temperature change from the analytical design tool using an adjusted groundwater velocity of 3 m/yr (dashed lines) compared with field data (dotted points) at DTS-7.
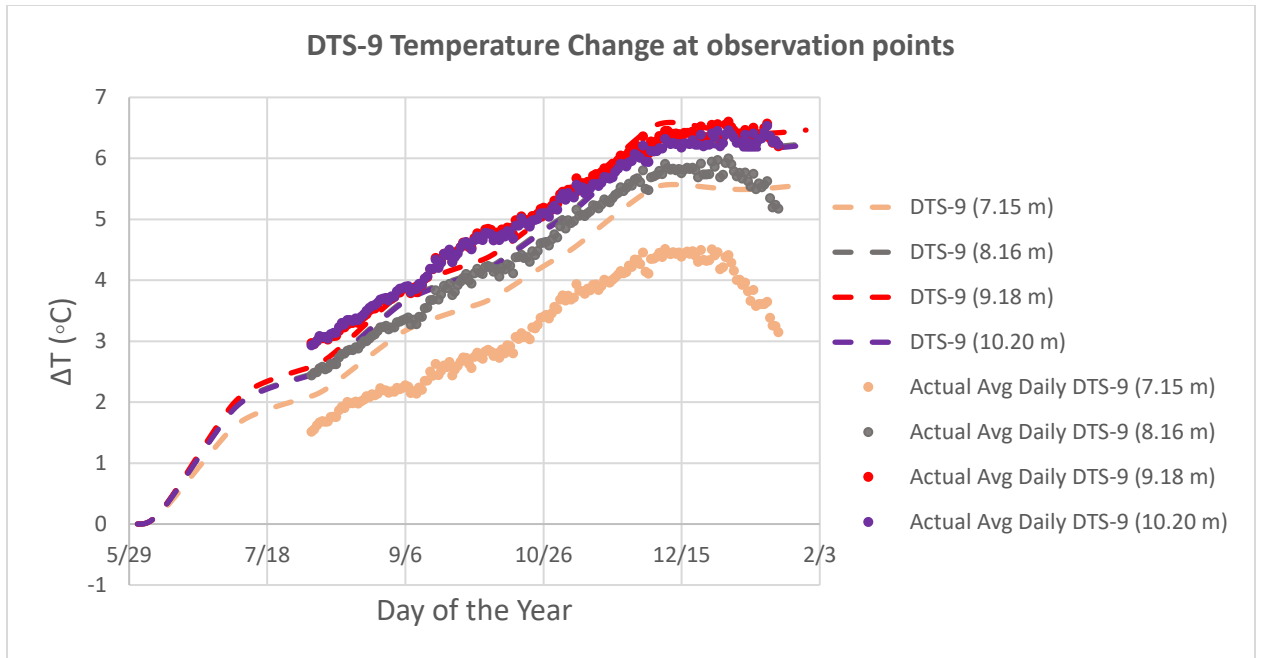
Fig. 28. Simulated temperature change from the analytical design tool using an adjusted groundwater velocity of 3 m/yr (dashed lines) compared with field data (dotted points) at DTS-9.

4.6 5-Year Projection of Temperature Change at the Vandenberg Test Site

On a solar thermal remediation project, it is useful to have an idea of what the long-term temperature change will be beyond what has already been described by available data. The ability to predict these long-term trends can help project managers estimate the total duration time of the contaminant remediation as well as the total costs required to complete the project. Additionally, an estimate of future temperature change can help determine whether changes to the current solar thermal remediation system configuration will be needed, or whether additional remediation methods will need to be installed.

After the analytical design tool had been compared to early-time temperature change at

Vandenberg Space Force Base, a 5-year projection of temperature change at the solar thermal

remediation test site was made using the analytical design tool. The runtime of the analytical

model was increased to 1,825 days to project temperature change on the field site for the next 4.5

years of operation. The average monthly power values that were derived from field data were

used to model the 5-year projection where a value of 335 watts was assigned to every July after

the first year of heating (see Table 5). Time series plots for observation points at DTS-5, 7, and 9

were constructed to show the long-term performance of the current solar thermal remediation

system configuration at various points on the test site. Figure 29 shows the 5-year temperature

change projection at the DTS-5 observation location between the depths of 7 and 10 meters.
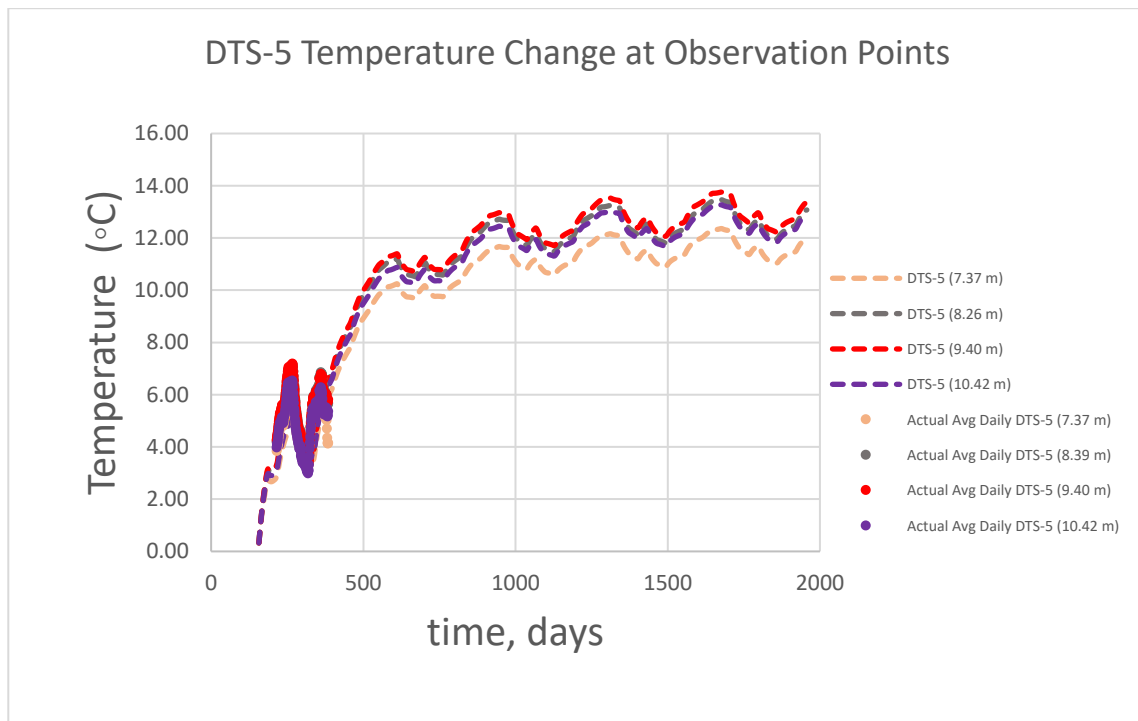
Fig. 29. 5-year model projection of temperature change from 7 to 10-meter depths at the DTS-5
observation location on the Vandenberg test site.

After 15 months of heating, the rate of temperature rise in the subsurface begins to equilibrate, eventually reaching a peak increase of 13.5 ∘C in August of the 3rd year since the start of heating. From this point in time, the temperature change will continue to fluctuate between 11.5 and 13 ∘C unless the average daily heat flow rate supplying power to each BHE changes. For instance, the current configuration of the solar thermal remediation system on Vandenberg Space Force Base is operating at an average yearly heat flow rate of 300 watts per borehole. Figure 30 shows a hypothetical 5-year projection if this value was increased to 500 watts per borehole.
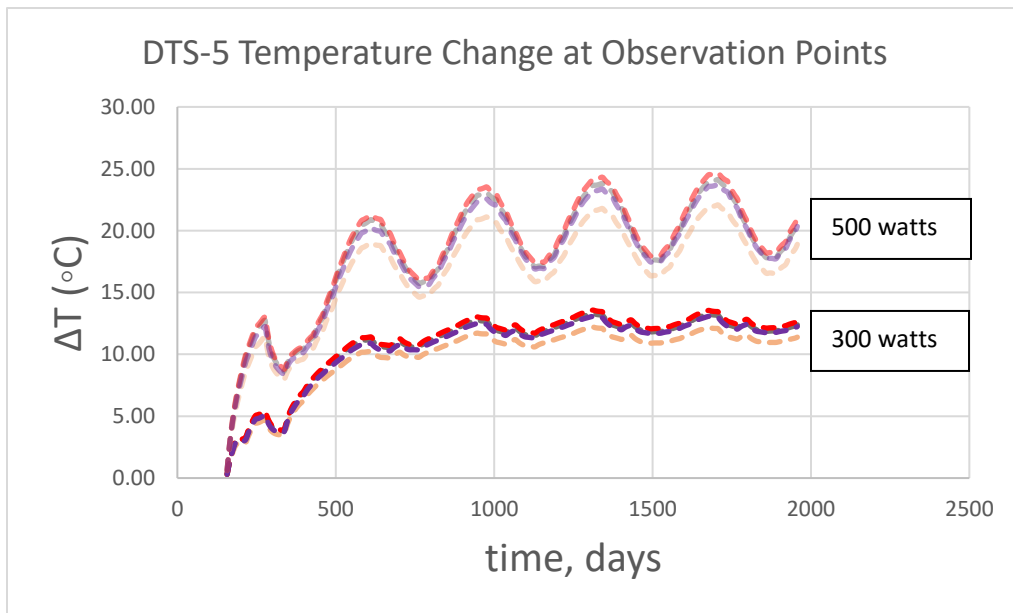
Fig. 30. Hypothetical projected temperature change if the average yearly power was increased from the current 300 watts to 500 watts per borehole.

With a yearly average of 500 watts being supplied to each BHE, the increased amount of power per borehole allows the temperature change to climb by over 23 ∘C before equilibrating. Figure 31 shows the 5-year temperature change projection at the DTS-7 observation location

between the depths of 7 and 10 meters. After 15 months of heating, the rate of temperature rise in the subsurface begins to equilibrate, eventually reaching a peak increase of 11 ◦C in August of the 3rd year since the start of heating. The temperature change then fluctuates seasonally between 10 and 11 ◦C.
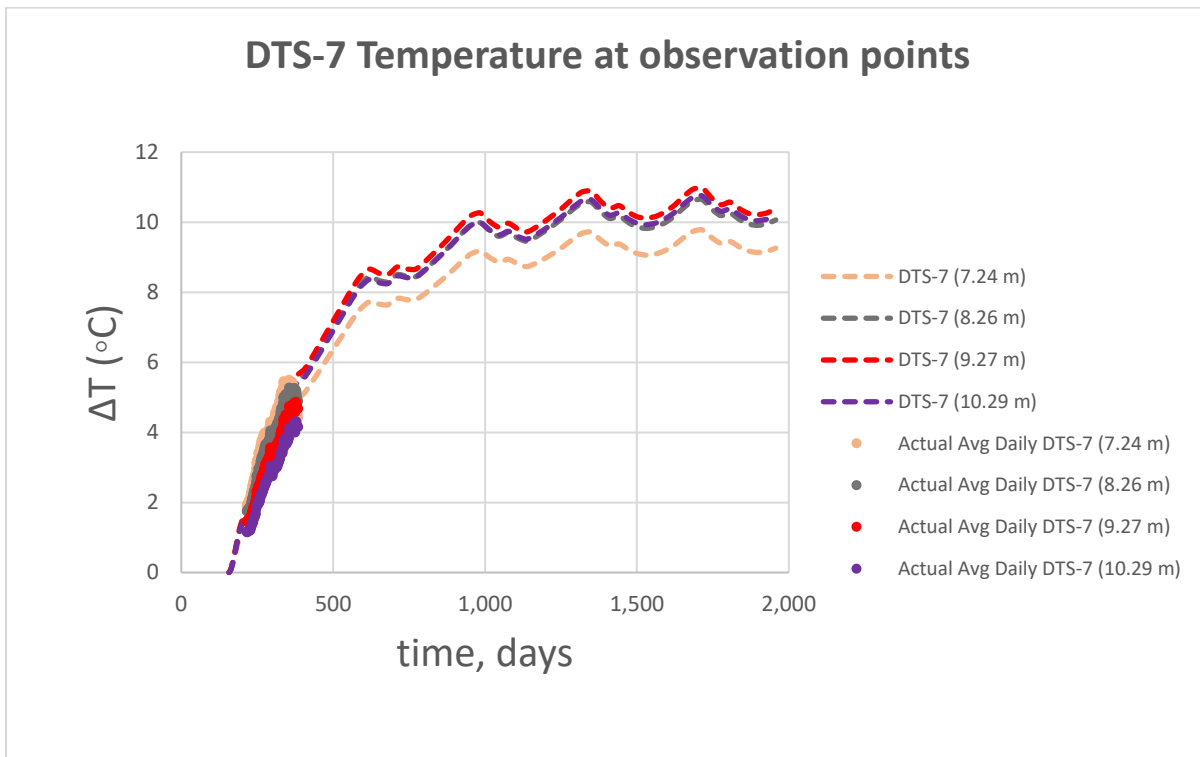
Fig. 31. 5-year model projection of temperature change from 7 to 10-meter depths at the DTS-7 observation location on the Vandenberg test site.

Figure 32 shows the 5-year temperature change projection at the DTS-9 observation location between the depths of 7 and 10 meters. After 15 months of heating, the rate of temperature rise in the subsurface begins to equilibrate, eventually reaching a peak increase of 12 ◦C in August of the 3rd year since the start of heating. The temperature change then fluctuates seasonally between 11 and 12 ◦C.
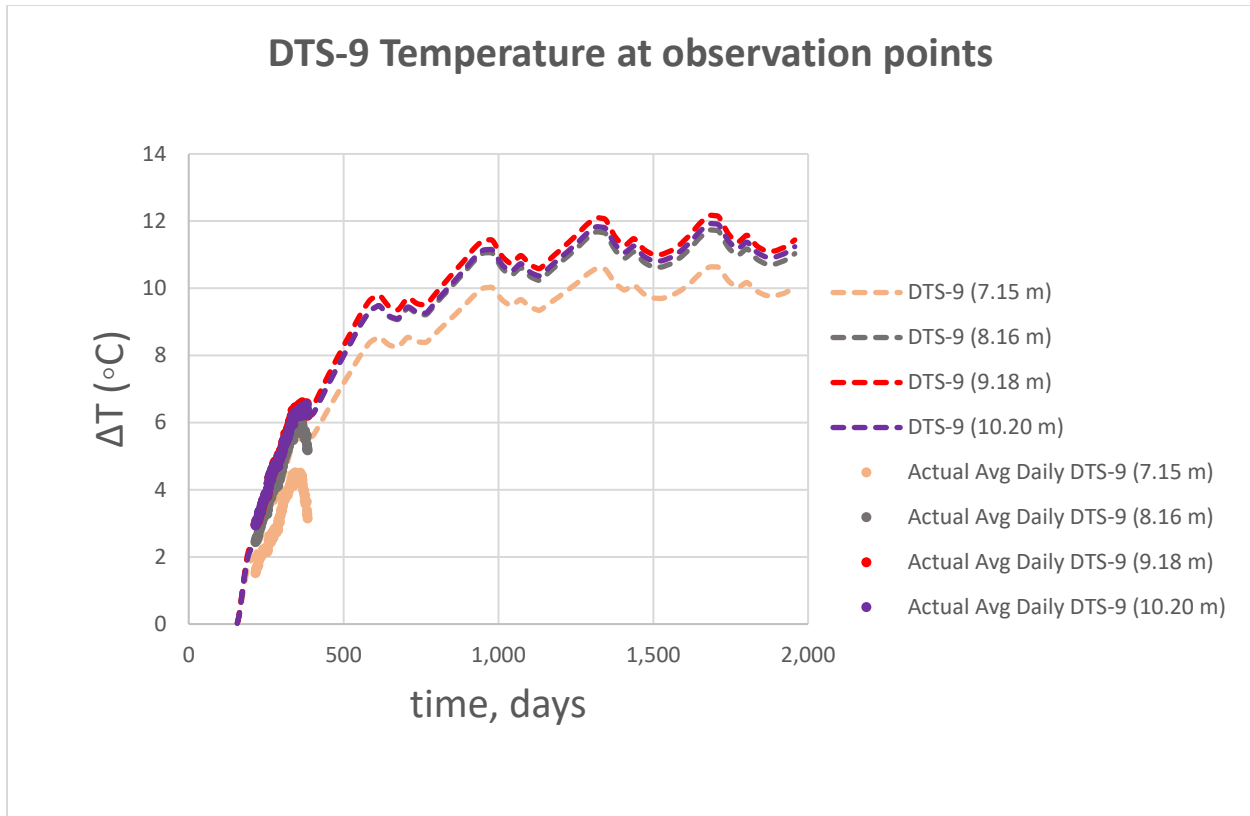
Fig. 32. 5-year model projection of temperature change from 7 to 10-meter depths at the DTS-9 observation location on the Vandenberg test site.

The XY and XZ snapshot flags in the user interface (See Appendix 1A) were used to generate contour plots projecting the horizontal and vertical temperature distribution from the Vandenberg test site after the temperature had been estimated to stabilize after 3 years of heating. Figure 33 shows an aerial view of the projected lateral temperature distribution after 15 months of heating on the test site. The 27 °C contour can be seen to envelope all eight BHEs, accounting for a total area of 160 m^2 while the heaters themselves have reached temperatures up to 39 °C.
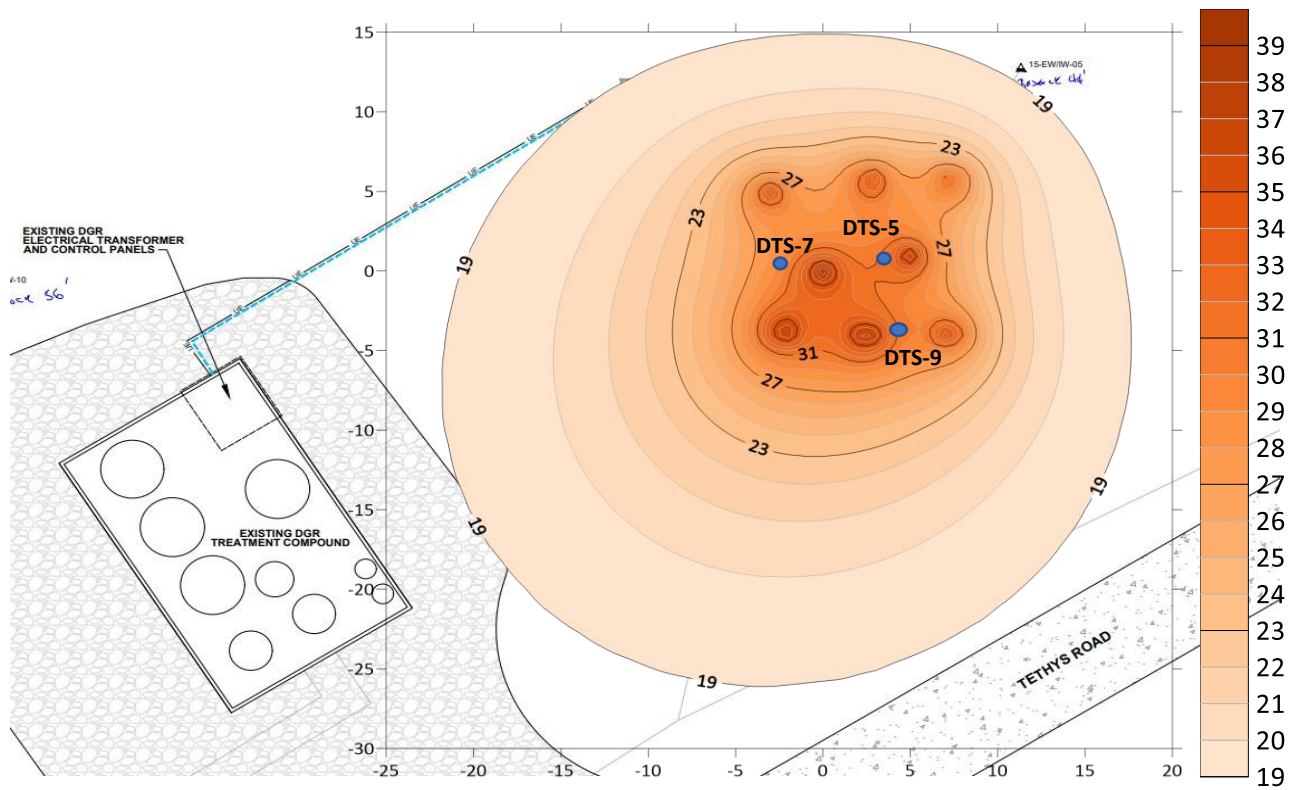
Fig. 33. Projected lateral heat propagation from the current solar thermal remediation configuration at Vandenberg after 3 years of heating (9 meters depth) and a background temperature of 18.5 ◦C.

Figure 34 shows a cross-sectional point of view of Figure 33 through BHE-4 and BHE-5 in the center of the heater array.
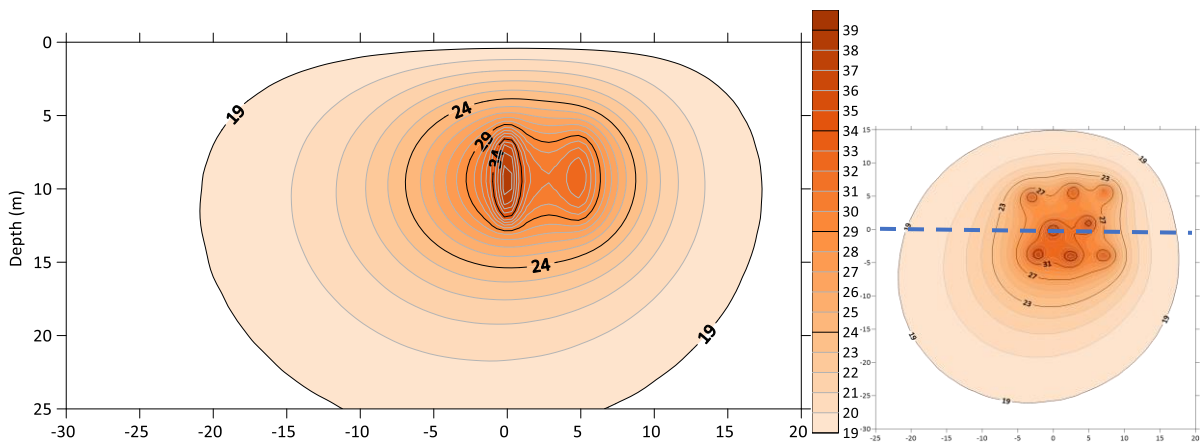
Fig. 34. Cross sectional temperature contour plot of BHE-4.

4.7 Summary

Using the initial reported groundwater velocity of 11.13 m/yr, the analytical design tool reasonably predicted the overall trend of temperature change within the depth range of 7 to 10 meters from August through December of the 1st year of heating as model simulations differed from the field data by 1 to 2 ∘C at the most for any given point in time. Favorable average R^2 values that described an overall fit between projected temperature change and field data taken at a range of observation points at the DTS-7 and DTS-9 locations suggest that at these locations, the initial model simulation was able to sufficiently predict the observed temperature change.

Confidence in the initially reported groundwater velocity was low on the basis that this parameter can vary by many orders of magnitude in heterogeneous subsurface conditions. In an effort to improve the agreement between the model simulation and field data, particularly at the DTS-5 location where initial R^2 values were negative, additional model simulations were generated using a range in groundwater velocities. The results showed how reducing the groundwater velocity had a much larger impact at DTS-5, where R^2 significantly improved at every depth for each reduction in velocity while R^2 values remained relatively constant at DTS-7 and DTS-9.

While the analytical model was able to simulate the power outages to BHE-3 and BHE-5 from October through November using the power factor inputs, it was unable to account for a second period of rapid temperature decline that was observed from field data from late December through the end of data collection in mid-January. No power outages to any component of the solar thermal remediation were detected at this time and it is possible that this event may have been caused by a severe rainstorm that was reported over the test site. Weather patterns that can reduce the available solar irradiation could also be a potential explanation for the overestimation

59

of the average monthly power delivery by the built-in solar heat flow calculator. A reduction in solar irradiation will result in a smaller power than can be generated from the system but even in the event of a dramatic reduction in solar irradiation, the collector efficiency will remain relatively constant.

Five-year projections of the current configuration of the solar thermal remediation system in place at Vandenberg Space Force Base suggest that subsurface temperatures could potentially increase by about 10 ◦C within 3 years of operating before equilibrating. Temperature contour plots of the test site after 3 years of heating suggest that temperatures in the immediate vicinities of the heat exchangers could reach temperatures 10 degrees higher than the surrounding subsurface.

5   MODELING THERMAL ENHANCED DECAY AT VANDENBERG SFB

After a detailed projection of temperature change throughout the current configuration of the Vandenberg solar thermal remediation test site had been made, the temperature output data generated from the analytical model could then be used with temperature decay factors to estimate the general thermal enhanced decay at the site over time. Decay projections from two different variations of the test site were then compared with the current configuration at Vandenberg SFB. These alterations were designed to optimize the solar thermal remediation test site by 1) maximizing the decay rate by increasing subsurface temperatures to peak thermal enhancement conditions and 2) Increasing the number of BHE's to expand the area of total decay.

5.1 Thermal Enhanced Decay of the Current Solar Thermal Remediation Configuration: 8 BHE's / 8 Solar Panels

5.1.1 Methods

As mentioned previously in this work, the temperature range for facilitating mesophilic activity that contributes to thermal enhanced decay has generally been observed to be between 20 and 40 °C (Horst, 2018). Decay rates of most contaminant compounds have been observed to double for every 10-degree increase in temperature (Dettmer, 2002) and peak thermal enhancement is expected to occur between 30-40 °C (Macbeth et a., 2012). At temperatures above 40 °C, mesophilic activity generally deactivates and any further degradation is reliant on the presence of thermophiles: microorganisms that can withstand high temperatures (Truex et al., 2007).

However, the exact relationship between temperature and compound degradation rates can vary amongst different contaminant strains, and little is known about the change in microbial activity rates beyond 40 °C (Dettmer, 2002). For modeling purposes, this makes it vitally important for the user to have a fundamental understanding of how temperature rise influences the decay of the in-situ contaminant. Unfortunately, representative decay factors for the Vandenberg test site were unavailable at the time of this writing, and so hypothetical values were used to demonstrate possible in-situ outcomes of thermal enhanced decay. Preliminary data from laboratory experiments suggest that the actual decay enhancement at elevated temperatures may be lower than the values assumed here.

Table 11 shows the decay factors that were used to model thermal enhanced decay in all three configurations of the Vandenberg solar thermal remediation system. Between 10 and 40 °C, the decay factors are assumed to double in value for every ten-degree increase in temperature. Peak thermal enhancement is assumed to occur at 35 °C, where a maximum decay factor of 2.8 is assigned. Decay factors of 0 were assigned to temperatures 40 °C and greater, where it is assumed that the contaminant decay ceases to occur.

The analytical model was run with the decay tool for the current solar thermal remediation system configuration for up to 3, 6, and 10 years of heating with an assumed base decay rate of 0.35 1/yr and a retardation factor of 2. The decay ratio $\left(\frac{C_{Thermal}}{C_{base}}\right)$ after each runtime was plotted as contour maps showing the simulated thermal enhanced decay.

Temperature (°C)	Decay Factor
0	0.1
5	0.2
10	0.5
15	0.71
20	1
25	1.41
30	2
35	2.8
40	0
45	0
50	0
55	0
60	0

Table 11. Decay factors used to model thermal enhanced decay at the Vandenberg test site.

5.1.2 Results

The hypothetical decay factors in Table 11 were used to project the potential thermal

enhanced decay for the current system configuration at Vandenberg Space Force Base (8 BHE's

to 8 solar panels) to end-times of 3, 6, and 10 years. Figure 35 shows the simulated thermal

enhanced decay on the test site after 3 years of heating.
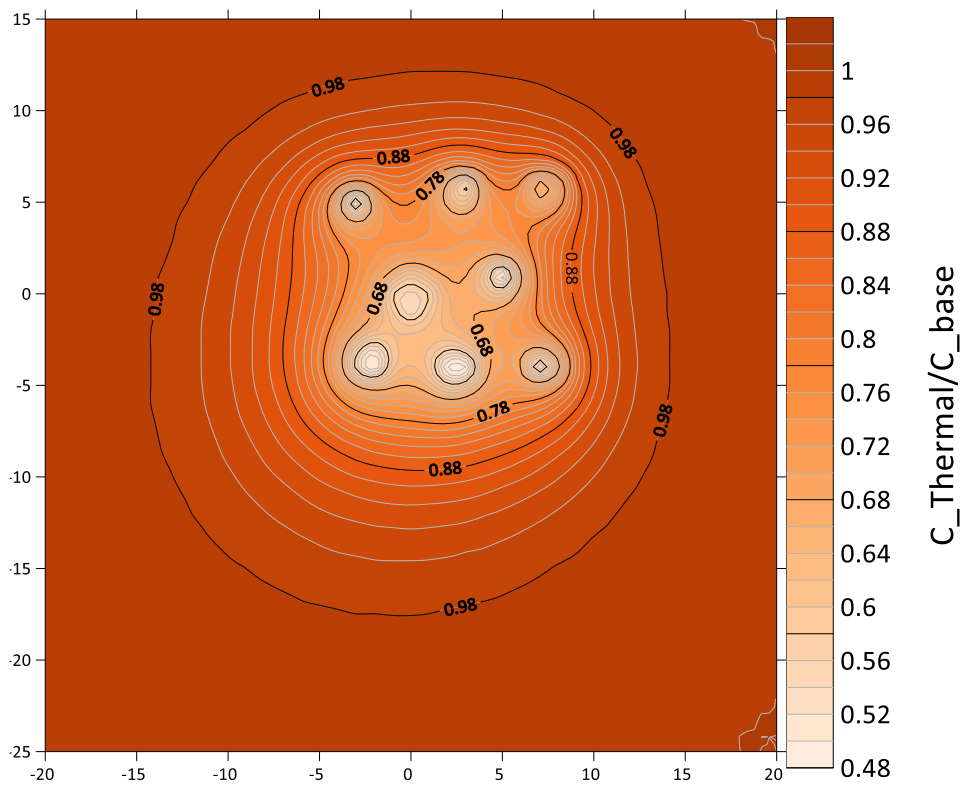
Fig. 35. Simulated thermal enhanced decay $\left(\frac{C_{Thermal}}{C_{base}}\right)$ on
the Vandenberg test site after 3 years of heating.

The 8 BHEs can be seen to be enveloped by the 0.78 contour, which means that at the

perimeter of the $100\ m^2$ BHE array, the extent of base case decay (C_{base}), or the amount of

decay that has occurred at the constant ambient temperature, is projected to be enhanced by 22%

as a result of 3 years of heating. The decay ratio gradually drops toward the center of the BHE array where temperatures are higher and the thermal enhanced concentration ($C_{Thermal}$) is reduced at increasing rates from the higher decay factors. In the immediate vicinity of the heaters where temperatures are the highest, the thermal enhanced decay has reached as high as 52%.

Figure 36 shows the projected thermal enhanced decay on the site after 6 years of heating. Contaminant decay within the 100 m^2 BHE array has been thermally enhanced by 40% and greater, reaching as high as 80% within the immediate vicinity of the heaters.
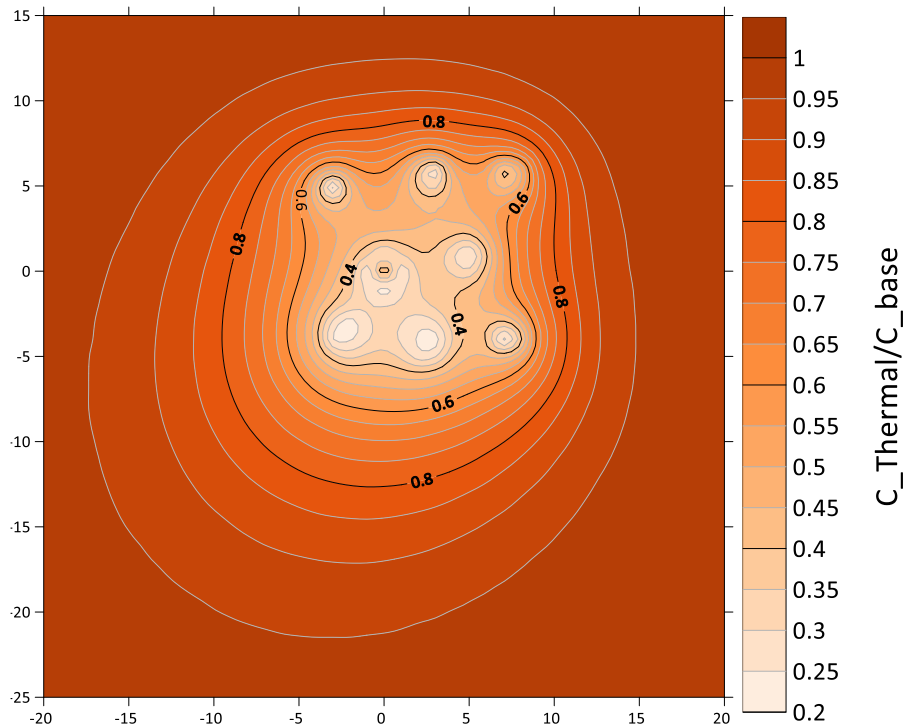
Fig. 36. Thermal enhanced decay $\left(\frac{C_{Thermal}}{C_{base}}\right)$ on the Vandenberg test site after 6 years of heating.

Figure 37 shows the projected thermal enhanced decay on the site after 10 years of heating. Contaminant decay within the 100 m^2 BHE array has been thermally enhanced by 70% and greater compared to the constant ambient temperature case (C_{base}). Thermal enhanced decay ($C_{Thermal}$) reaches as high as 95% within the immediate vicinity of the heaters where temperatures have reached 35-40 ∘C.
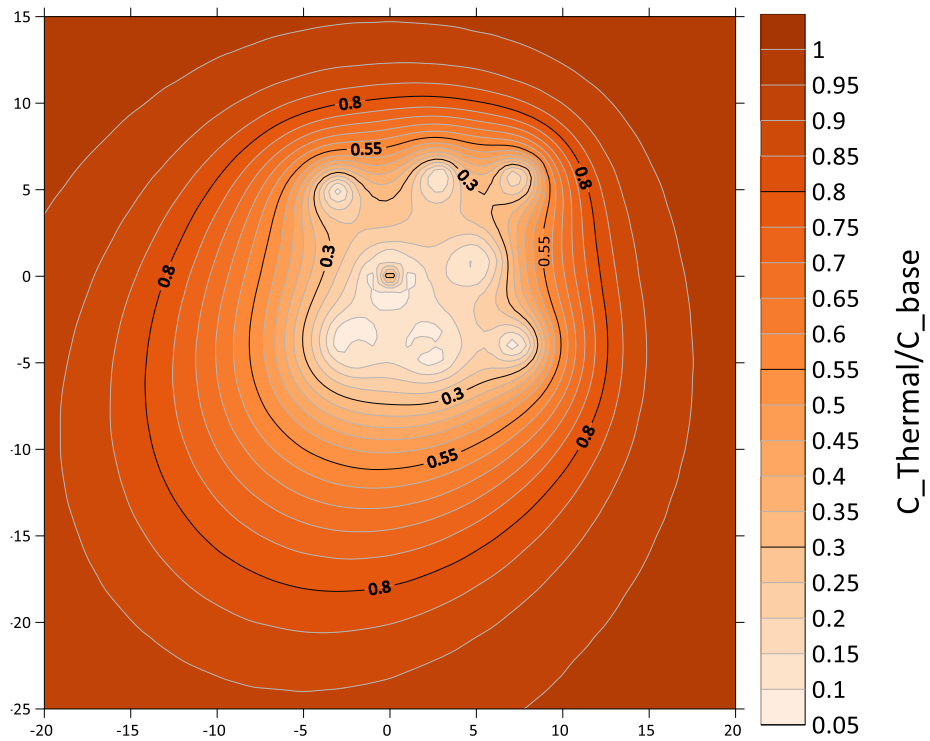
Fig. 37. Thermal enhanced decay $\left(\frac{C_{Thermal}}{C_{base}}\right)$ on the Vandenberg test site after 10 years of heating.

5.2 Thermal Enhanced Decay of System Configuration #2: 8 BHE's / 13 Solar Panels

An alternative configuration to the Vandenberg solar thermal remediation system was designed to maximize decay rates by increasing steady-state subsurface conditions to the peak thermal temperature of 35 °C. By introducing additional solar panels to the system and increasing the average monthly power rates, it was expected that the resulting temperature increase would shorten the duration of remediation and contribute to a larger degree of contaminant destruction.

5.2.1   Methods

The solar calculator component of the analytical design tool was used to estimate a new variable power rate supplying the solar thermal remediation system from an increased number of solar panels. The calculator was calibrated to actual average monthly power rates by adjusting the collector efficiency input until the projected average daily heat flow rate per borehole equaled that of the field data. Adjusting the collector efficiency to 0.245 projected an average daily heat flow rate of 300 watts per borehole. Figure 38 shows the new average monthly heat flow rates projected by the solar calculator after calibrating it to the field data under the current system configuration of 8 BHEs to 8 solar collectors at the test site.
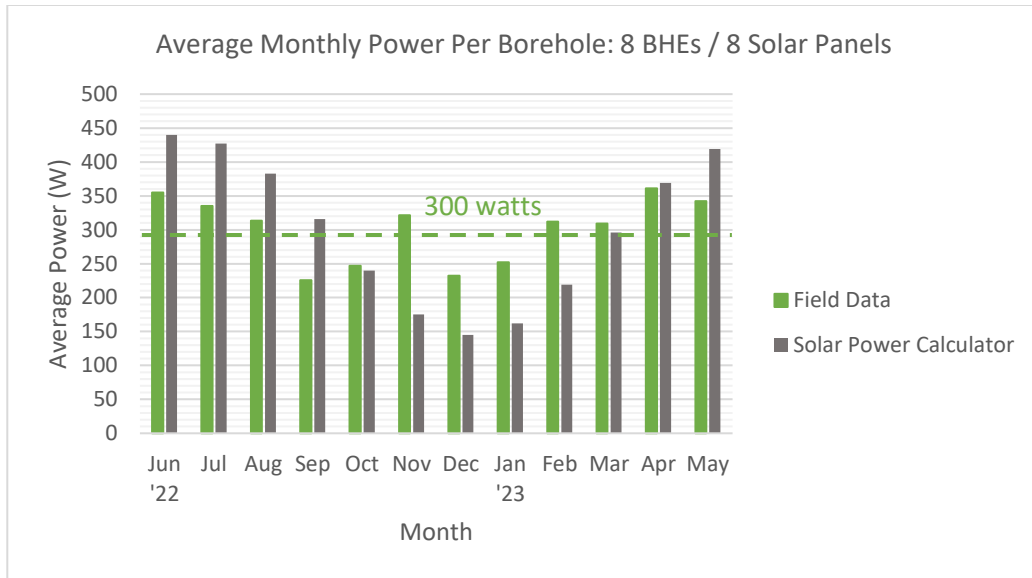
Fig. 38. Average monthly power (8 BHEs to 8 solar panels) projected by the solar calculator compared to field data after adjusting the collector efficiency.

After the solar calculator was adjusted to the average daily heat flow rate, the number of solar panels was increased and the heat flow was recalculated, sending new average monthly power values to the analytical model. This was repeated until subsurface temperature projections equilibrated to the peak thermal enhancement temperature 35 ∘C.

To evaluate the improvement in decay of the optimized solar thermal remediation system configuration, the plotted contour results were subtracted from those of the original system configuration. This resulted in a new contour map that plots the difference in thermal enhanced decay between the two system configurations for each simulation.

Based on time series plots extracted from the DTS-5, 7, and 9 observation points,

subsurface temperatures increase and equilibrate near the peak thermal enhancement temperature

of 35 °C when utilizing 13 solar panels to 8 BHE's in the solar thermal remediation system,

yielding a new average daily heat flow rate of 487 watts per borehole. Figure 39 shows the

monthly distribution of power to each borehole when the solar thermal remediation system is

operating at this new average yearly power rate.
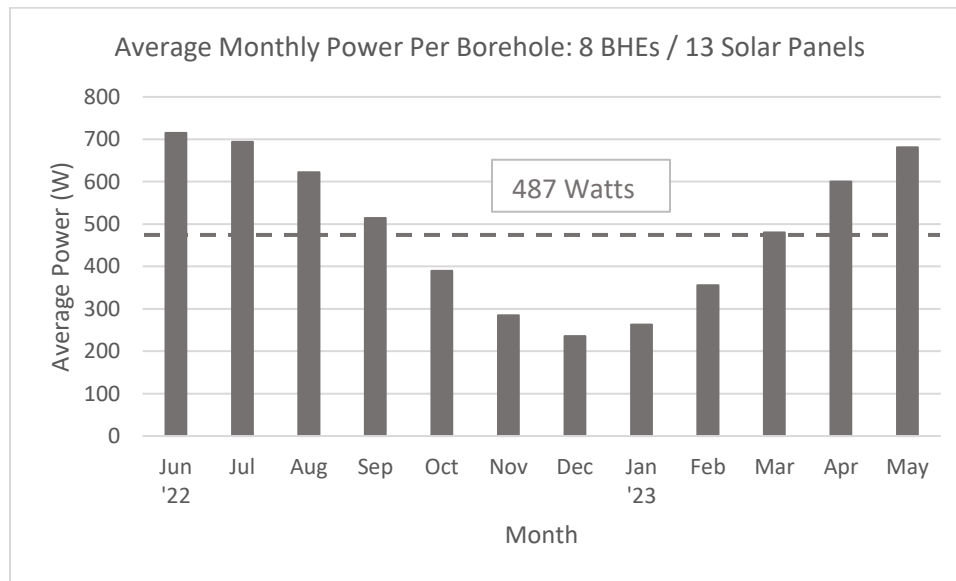
Fig. 39. Average monthly power projected by the solar calculator when the
system is operating with 8 BHEs and 13 solar panels.

Figure 40 shows how the model projects temperatures at the DTS-5 observation locations

to equilibrate between just over 40 °C and just under 35 °C when operating at the new average

daily heat flow rate.
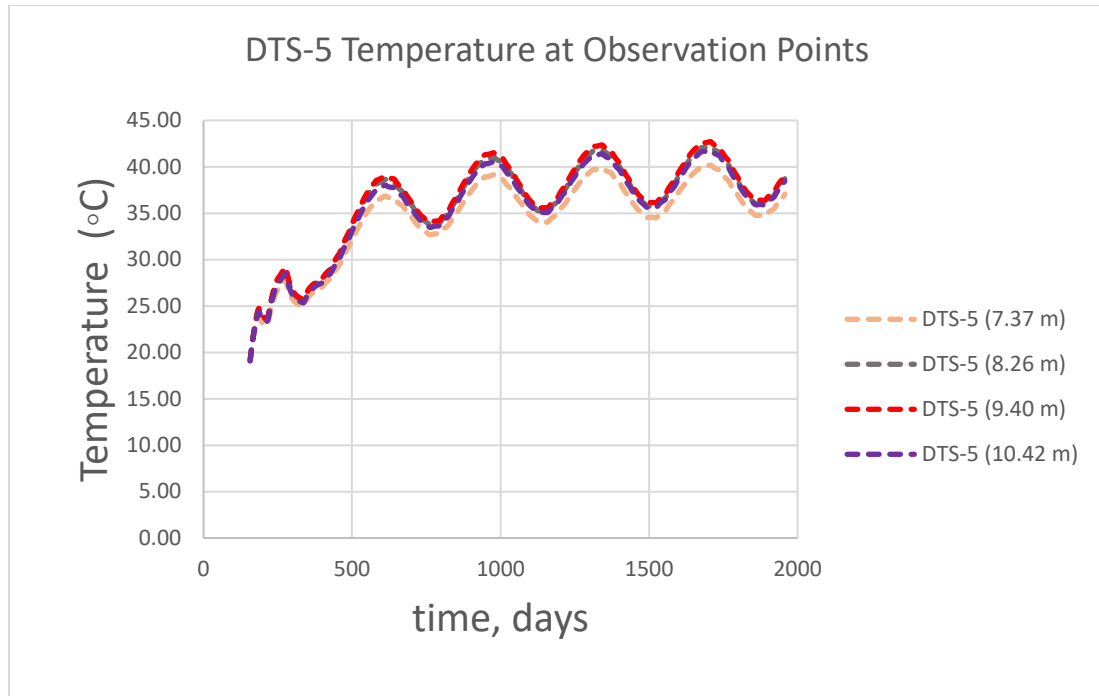
Fig. 40. Time series plot of the DTS-5 observation points showing elevated temperatures after adding 5 solar panels to the solar thermal remediation system.

Figure 41 shows how the model projects temperatures at the DTS-7 observation locations to equilibrate between 33 ∘C and 37 ∘C when utilizing 13 solar panels to the 8 BHEs in the solar thermal remediation system. Figure 42 shows how the model projects temperatures at the DTS-9 observation locations to equilibrate between 34 ∘C and 38 ∘C when utilizing 13 solar panels to the 8 BHEs in the solar thermal remediation system.
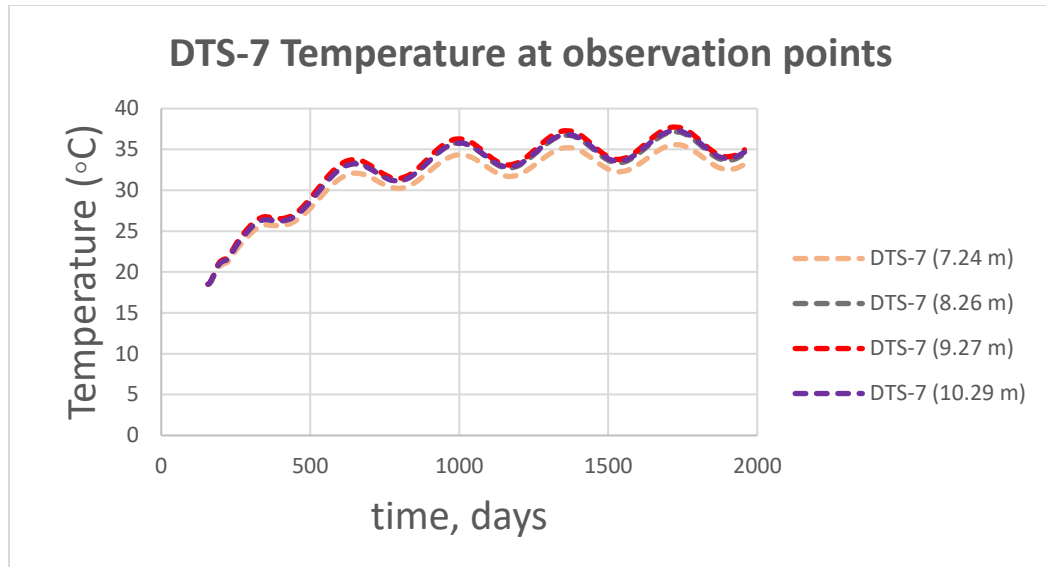
Fig. 41. Time series plot of the DTS-7 observation points showing elevated temperatures after adding 5 solar panels to the solar thermal remediation system.
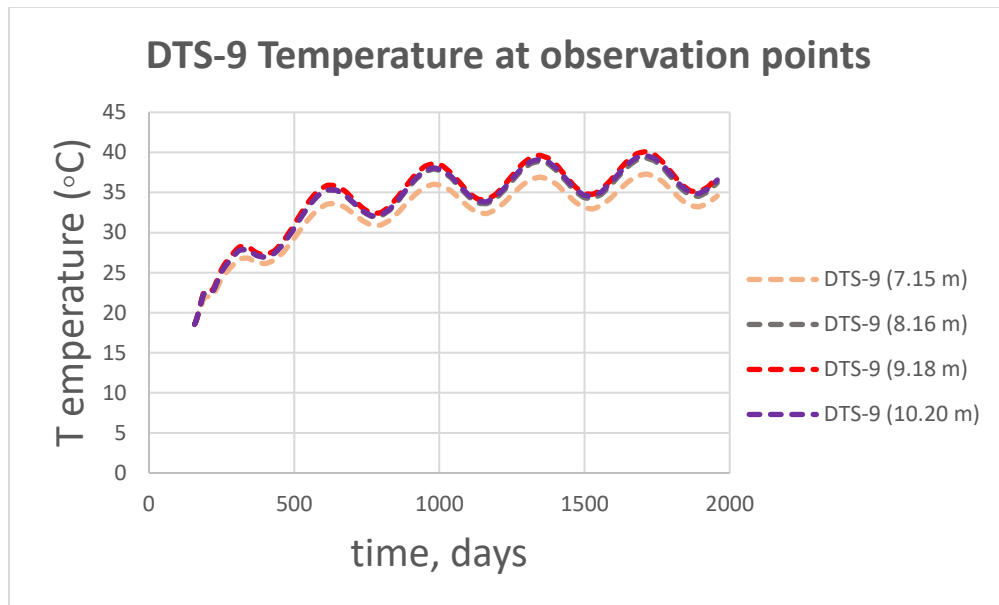
Fig. 42. Time series plot of the DTS-9 observation points showing elevated temperatures after adding 5 solar panels to the solar thermal remediation system.

The analytical model with the decay tool was then run for the alternate system configuration of 8 BHE's powered by 13 solar panels to end-times of 3, 6, and 10 years from the start of heating. Figure 43 shows the projected thermal enhanced decay of the optimized solar thermal remediation system after 3 years of heating, where decay has been thermally enhanced by up to 45 and 50% in the areas surrounding the BHEs.
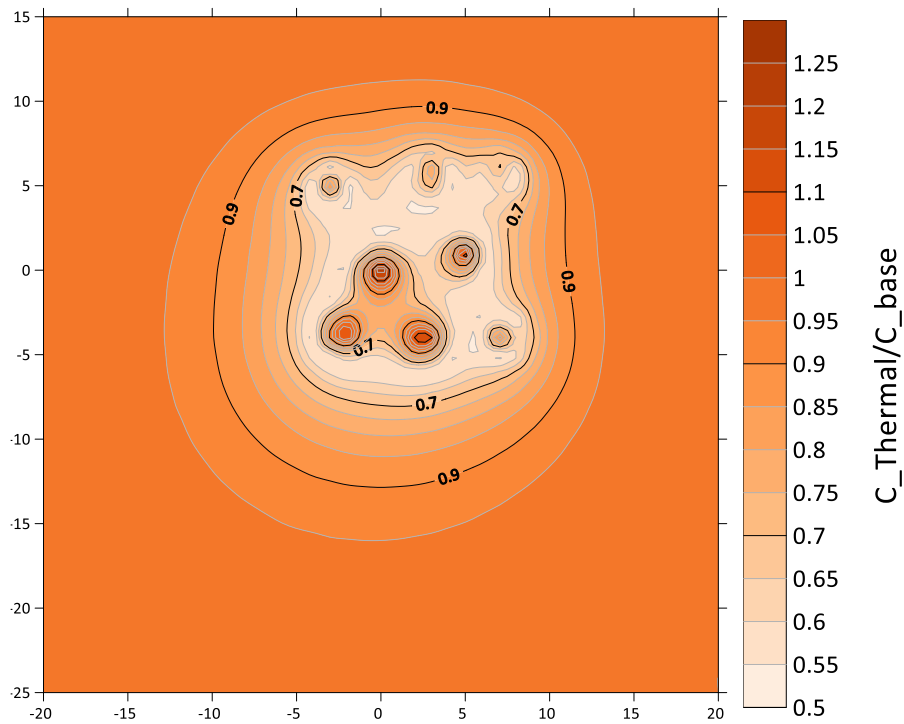
Fig. 43. Projected thermal enhanced decay of the optimized solar thermal remediation system after 3 years of heating

The decay ratio $\left(\frac{C_{Thermal}}{C_{base}}\right)$ has surpassed a value of 1 in the immediate vicinity of the BHEs in the Southwestern corner of the remediation system. In these regions, the temperature has surpassed 40 ∘C and risen out of the optimal mesophilic temperature range of 20 to 40 ∘C.

After the temperature reaches this point, the hypothetical decay factors are reduced to 0 and the thermal enhanced concentration component ($C_{Thermal}$) of the decay ratio ceases to decay. Because the base case component (C_{base}) of the ratio is independent of temperature change, C_{base} continues to decay and is eventually surpassed by $C_{Thermal}$, yielding a decay ratio greater than 1.

The decay ratio dataset of the optimized solar thermal remediation system after 3 years of heating was subtracted from that of the current system configuration for comparison. Figure 44 shows the difference in thermal enhanced decay between the two different configurations of the remediation site after 3 years of heating.
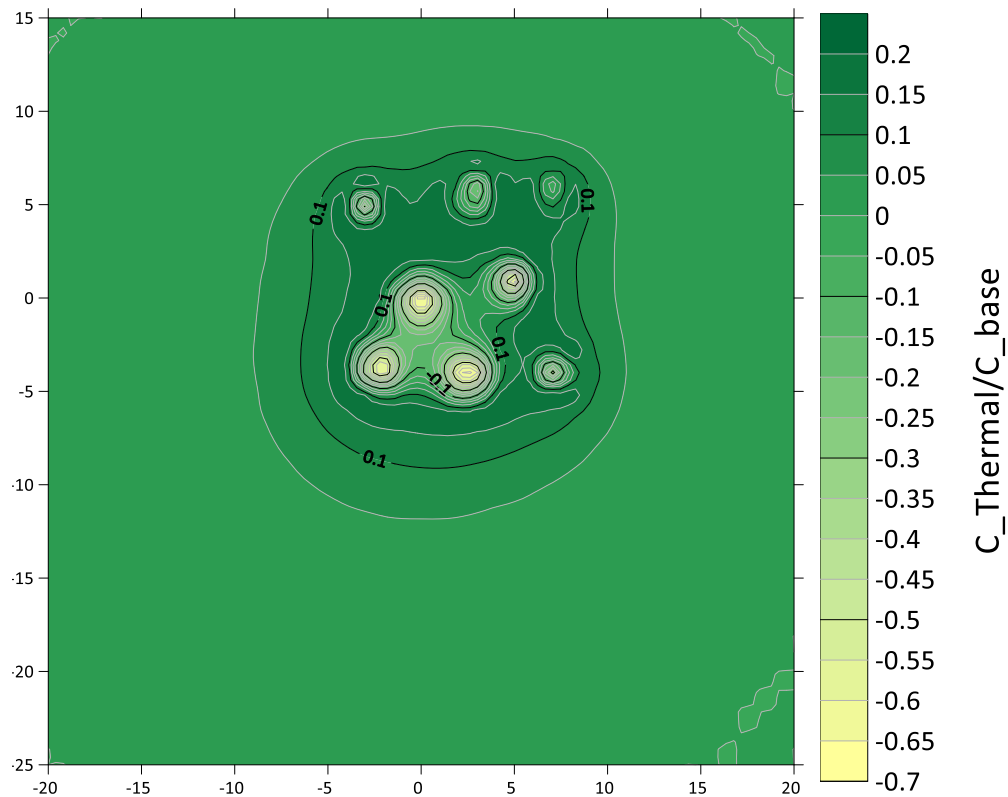
Fig. 44. Difference in thermal enhanced decay between the current system configuration at the Vandenberg test site of 8 solar panels and the optimized configuration of 13 solar panels after 3 years of heating.

After 3 years of heating, the thermal enhanced decay improved by 15-20% in the areas within the 100 m^2 BHE array around the BHEs after adding 5 solar panels to the solar thermal remediation system. Negative values were observed in the Southwest corner of the BHE array, coinciding with the same area in which decay ratios of over 1 were projected by the model in Figure 43.

Figure 45 shows the projected thermal enhanced decay of the optimized solar thermal remediation system after 6 years of heating, where decay has been thermally enhanced by up to 80% in the areas surrounding the BHEs.
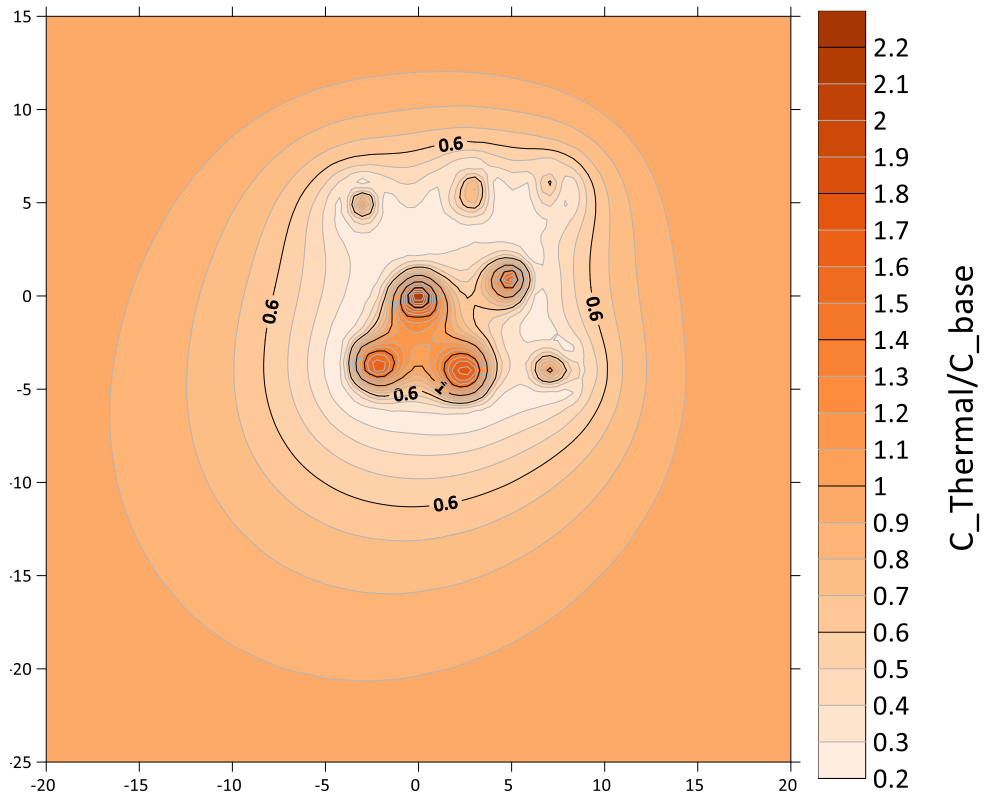
Figure 45. Projected thermal enhanced decay of the optimized solar thermal remediation system after 6 years of heating.

The simulated decay ratio $\left(\frac{C_{Thermal}}{C_{base}}\right)$ has surpassed a value of 2 in the immediate vicinity of the BHEs in the Southwestern corner of the remediation system, meaning the heated contaminant concentration is over twice it would have been under ambient conditions. If temperatures are maintained above the assumed mesophilic range threshold of 40 ∘C, then the decay ratio in this region of the remediation system will continue to rise as the thermal enhanced concentration ($C_{Thermal}$) remains constant and the base case concentration (C_{base}) continues to be reduced despite the elevated temperatures.

Figure 46 shows the difference in decay ratio between the two different configurations of the remediation site after 6 years of heating.
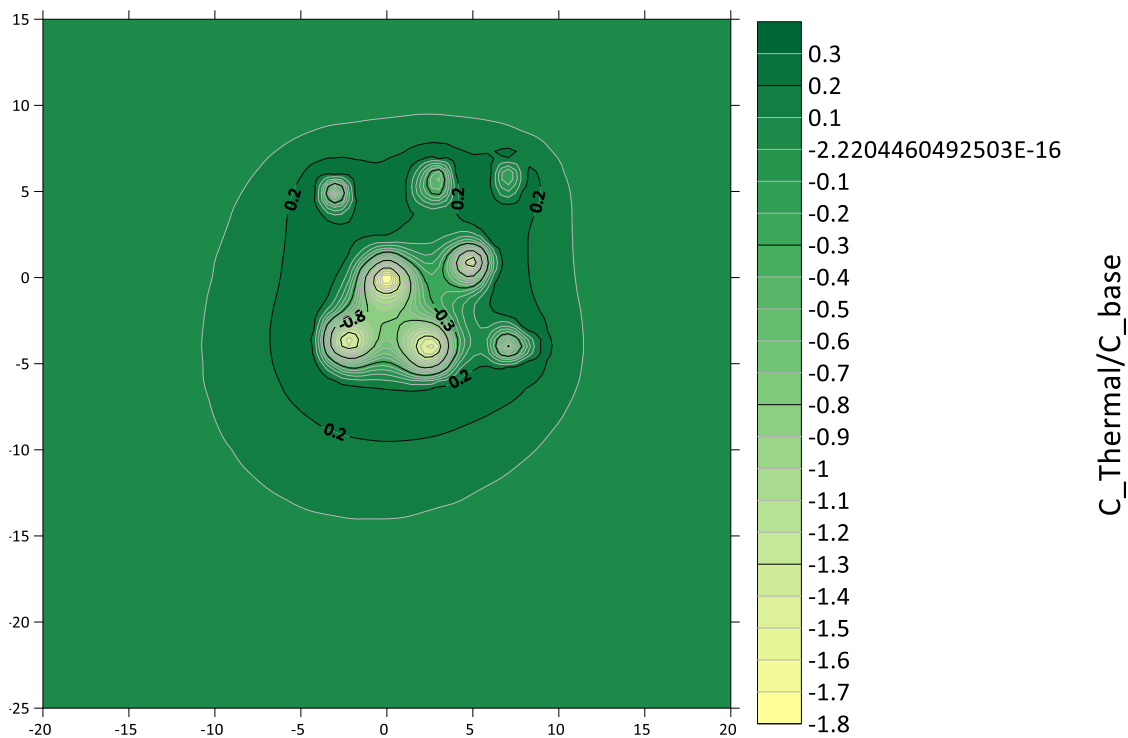
Fig. 46. Difference in decay ratio between the current system configuration at the Vandenberg test site of 8 solar panels and the optimized configuration of 13 solar panels after 6 years of heating.

After 6 years of heating, the thermal enhanced decay improved by 20-30% in the areas within the $100\ m^2$ BHE array around the BHEs after adding 5 solar panels to the solar thermal remediation system. The area of improvement has noticeably increased and expanded outward from the BHE array as temperatures outside of the remediation system have reached the optimum mesophilic range of 30 to 40 ∘C.

Figure 47 shows the projected thermal enhanced decay of the optimized solar thermal remediation system after 10 years of heating.
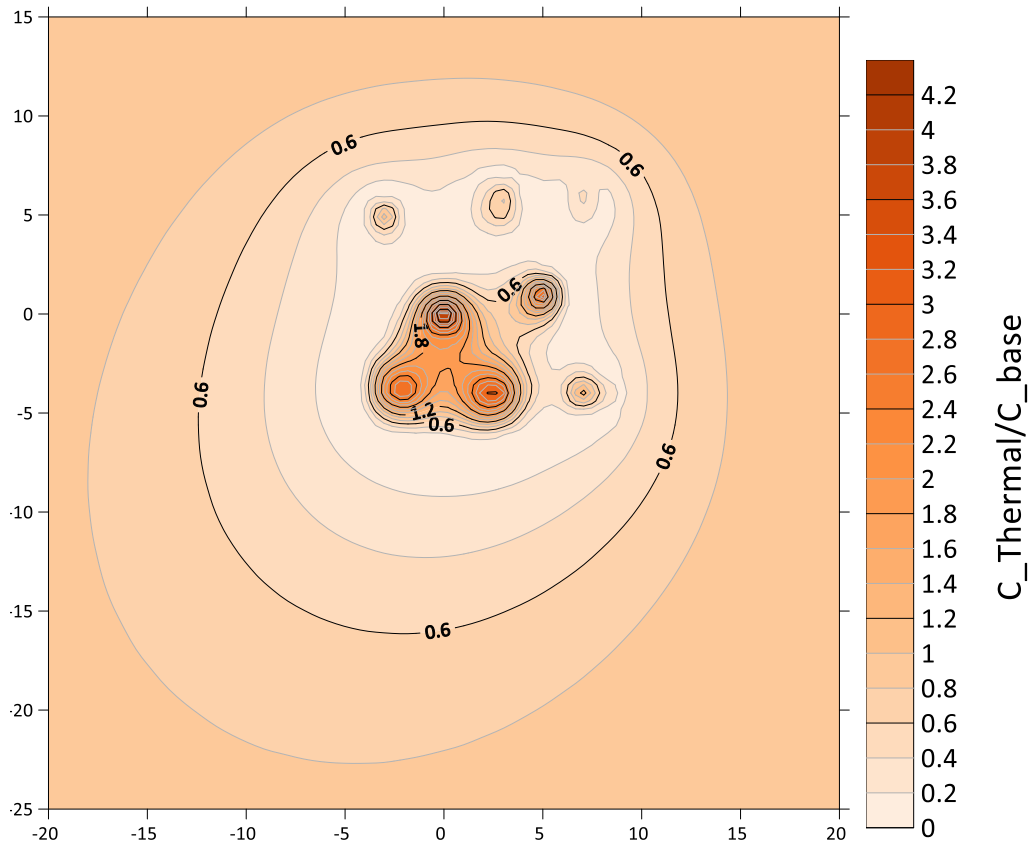
Figure 47. Projected thermal enhanced decay of the optimized solar thermal remediation system after 10 years of heating.

A large proportion of the area in and around the $100\ m^2$ BHE array has been thermally enhanced by 80% and greater. As shown by the color scale, a portion of that area has reached complete decay of the thermal enhanced concentration component $(C_{Thermal})$ of the decay ratio. As expected, the decay ratio $\left(\frac{C_{Thermal}}{C_{base}}\right)$ in the immediate vicinities of the BHEs in the Southwestern corner of the remediation system have surpassed a value of 4 owing to the sustained high temperatures in these areas.

Figure 48 shows the difference in decay ratio between the two different configurations of the remediation site after 10 years of heating.
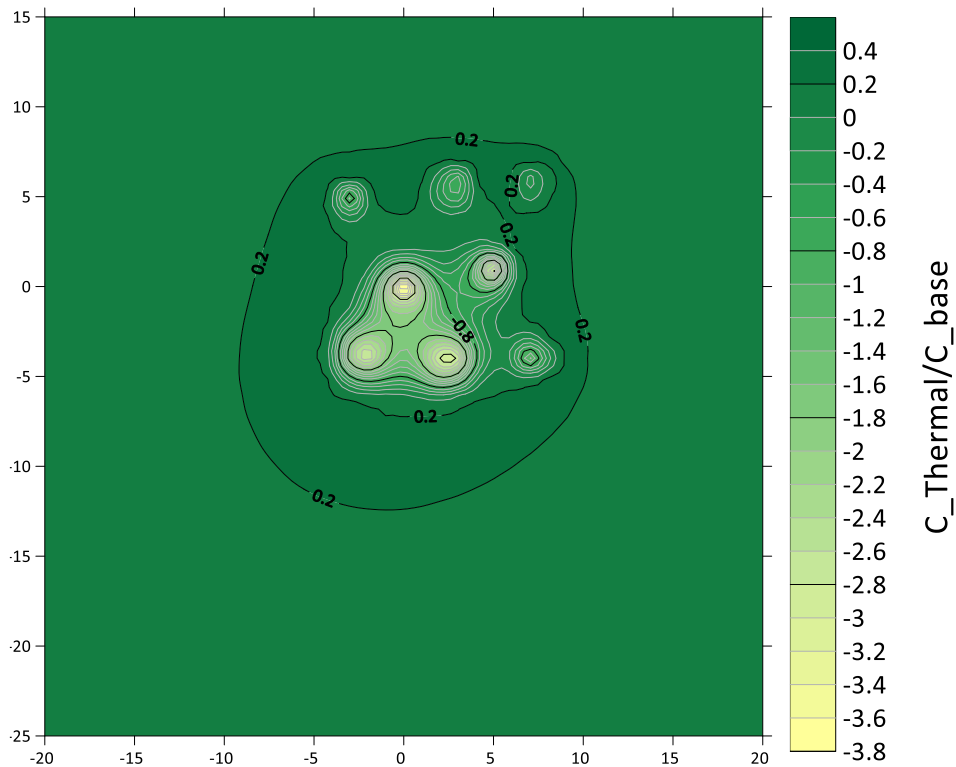
Fig. 48. Difference in decay ratio between the current system configuration at the Vandenberg test site of 8 solar panels and the optimized configuration of 13 solar panels after 10 years of heating.

After 10 years of heating, the thermal enhanced decay improved by 20-40% after adding 5 solar panels to the solar thermal remediation system. Although this is a modest improvement in decay, the area encompassing the largest difference between the 2 thermal enhanced decay simulation results has slightly shifted from being contained within the outer perimeter of the BHE array to just outside of the remediation system.

5.3 Thermal Enhanced Decay of System Configuration #3: 16 BHE's / 16 Solar Panels

A second alternative configuration of the test site was designed to expand the total area of enhanced decay by introducing additional BHE's to the solar thermal remediation system. The same average power per borehole as the current system configuration was maintained by keeping the same BHE-to-collector ratio. By doubling the number of BHE's and collectors in the system, it was expected that the total area of enhanced decay would expand substantially and contribute to a larger degree of contaminant destruction.

5.3.1 Methods

To model the second alternate system configuration, a new local coordinate system was set up with 16 BHE's equally spaced apart by 5 m. A series of 4 observation points were placed within the heating zone in the direction of assumed moving groundwater. Figure 49 shows the local coordinate system of the second alternate system configuration, including the 4 observation points: OBS-1, 2, 3, and 4.

The analytical model was run with the thermal enhanced decay tool using the same average monthly power-per-borehole values (Table 5) and decay factors (Table 11) as the current system configuration. The areas contained within targeted decay ratio contours were traced and measured for comparison between the current configuration of the solar thermal remediation system at the Vandenberg test site and the second optimized system configuration. Figure 50 shows an example of how simulated decay ratio contours can be traced using a measuring tool which will then estimate the total enveloped area. This process was implemented for 3 different simulations: 3, 6, and 10 years of heating.
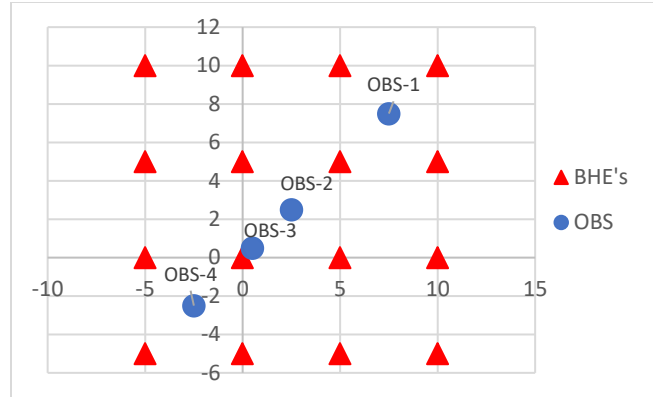
Fig. 49. Local coordinate system used to model the second alternate solar thermal remediation system.
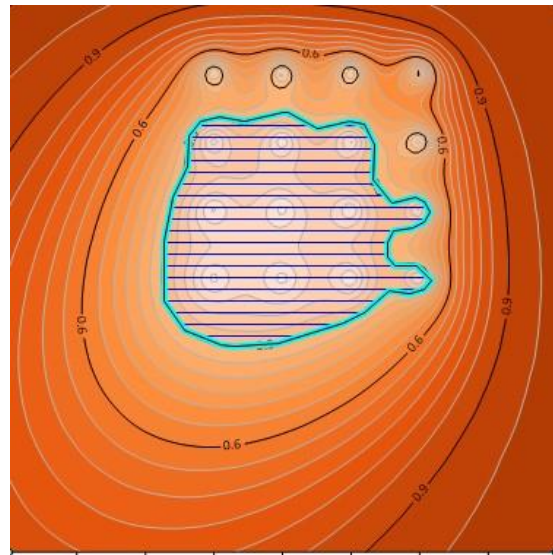
Fig. 50. Visual example of calculating the area enveloped by a decay ratio contour using a measuring tool.

5.3.2   Results

Figure 51 shows the horizontal temperature distribution of the 3rd configuration of the solar

thermal remediation system after 3 years of heating. Within the 225 m^2 area of the alternate

system configuration, temperatures were projected to rise by over 10 ∘C after 3 years.

Temperatures in close proximity to heaters in the Southwest corner of the test site were projected

to rise by over 15 ∘C. Overall, the lateral temperature distribution across the optimized solar

thermal remediation system after 3 years of heating is very similar to the current system

projection (See Figure 33). The maximum temperature projected by this optimized simulation is

just 2 degrees higher than what was predicted with the current configuration. This may be caused

by an increased amount of heat by convection that is propagating into the Southwest corner of

the test site due to the greater number of heat exchangers in the system.
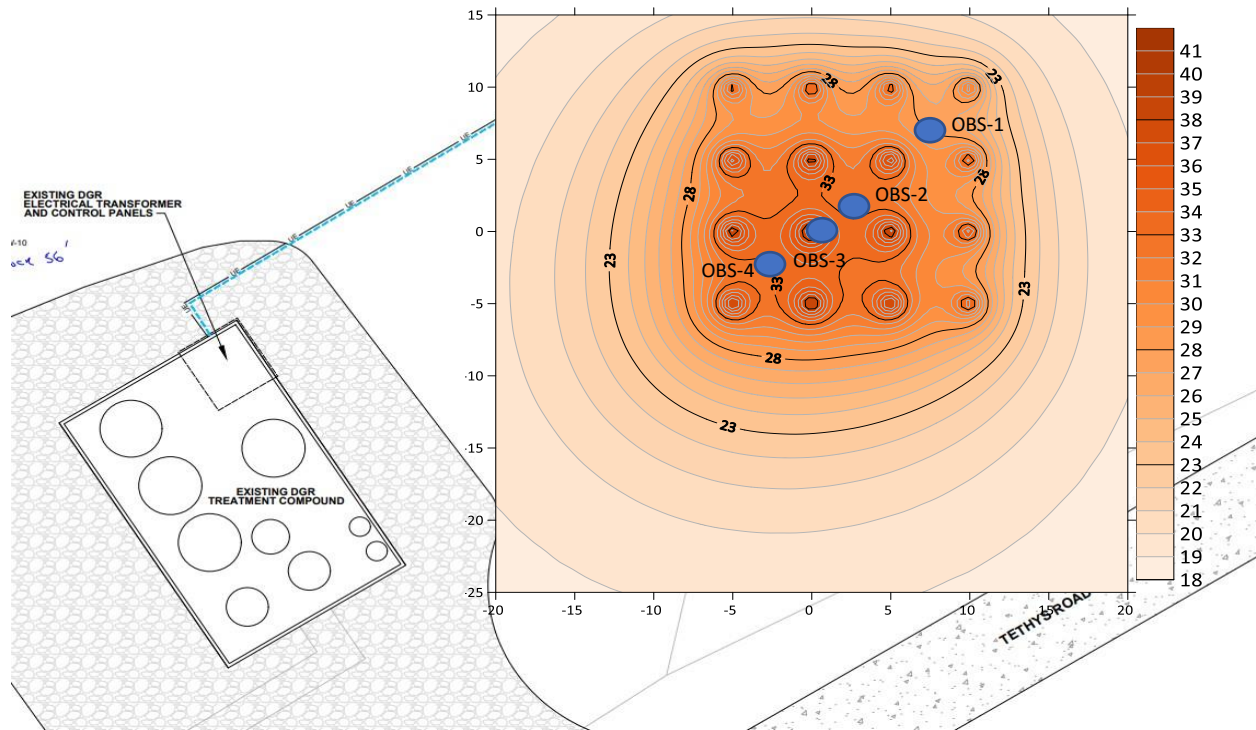
Fig. 51. Projected horizontal temperature distribution on the Vandenberg test site with an alternate configuration of 16 BHE's and 16 solar panels after 3 years of heating.

Figure 52 shows time series plots of the 4 observation locations of the 3rd system configuration over 3 years of heating. From the Northeast to the Southwest corners of the modeled solar thermal remediation system, the simulated temperature rise increases along the assumed path of groundwater flow from the added effects of convection.
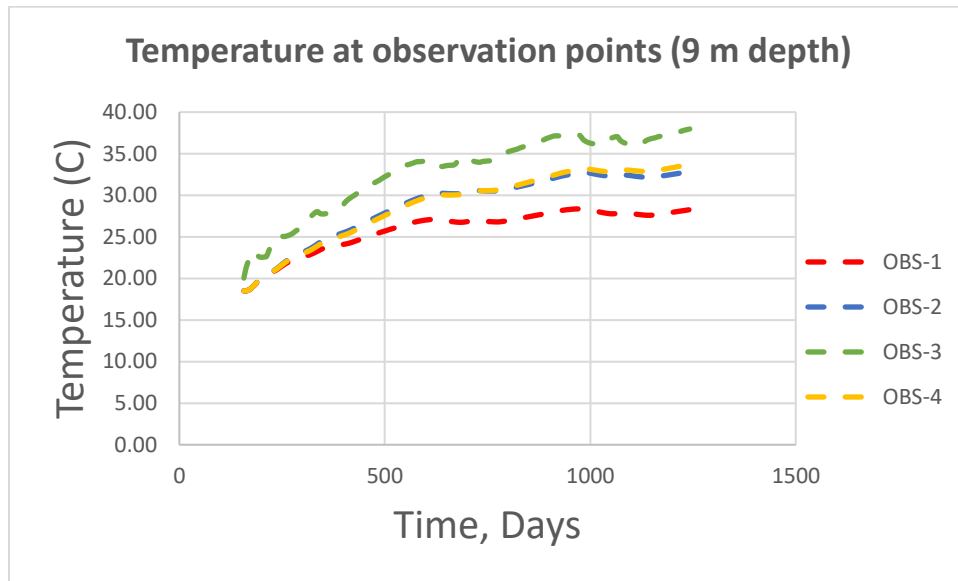
Fig. 52. Time series plot showing temperature change over a 3-year heating period at each of the 4 observation points placed in the 2nd alternate configuration of the solar thermal remediation system.

Figure 53 shows the projected thermal enhanced decay of the optimized system configuration after 3 years of heating. Like the simulated temperature distribution, the projected distribution of thermal enhanced decay over the optimized system is also very similar to the current system configuration (See Figure 35). Both simulations projected up to 50% thermal enhancement in areas surrounding the heat exchangers and up to 20% surrounding the outer perimeter of the remediation systems after 3 years of heating.
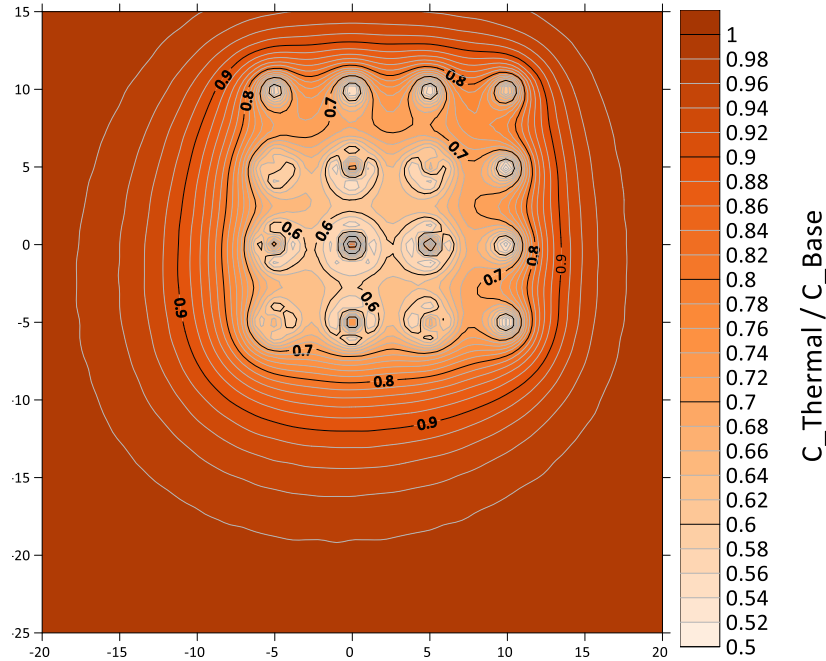
Figure 53. Simulated thermal enhanced decay of the 2nd alternate system configuration after 3 years of heating.

Table 12 summarizes how measured areas enveloped by targeted decay ratio contours compare with those of the current system simulation. Since doubling the number of solar panels and BHEs in the solar thermal remediation system, the area enveloped by the 0.8 decay ratio contour more than doubled in size. Table 12 shows how the area of the remediation system that was thermally enhanced by 20% and greater increased from 164 to 365 m^2 with the optimized system configuration. The area enveloped by the 0.7 decay ratio contour experienced a four-fold increase from 59 to 239 m^2.

3 Years	20+ %Decay	30+ %Decay
8 BHE : 8 collectors	164 m^2	59 m^2
16 BHE : 16 collectors	365 m^2	239 m^2

Table 12. Areas enveloped by the 0.8 (20% thermal enhancement) and 0.7 (30% thermal enhancement) decay ratio contours for the current system configuration compared with the optimized system after 3 years of heating.

Figure 54 shows the projected thermal enhanced decay of the optimized system configuration after 6 years of heating. The optimized simulation predicted a decay ratio distribution that was also similar to the current system configuration (See Figure 36), although the optimized simulation projected a maximum decay ratio that was 25% higher than the current system at the center of the heat exchangers and a minimum decay ratio that was 5% lower than the current system.
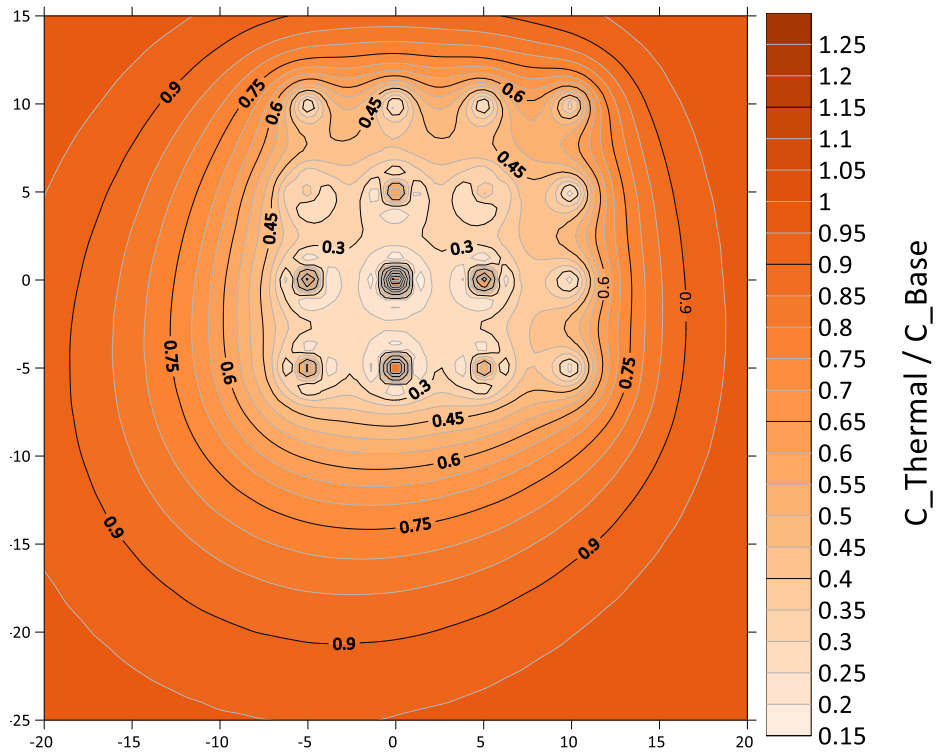
Fig. 54. Simulated thermal enhanced decay of the 2nd alternate
system configuration after 6 years of heating.

Table 13 summarizes the resulting increases in areas of decay that have been thermally enhanced by greater than 30 and 55% between the two model simulations after 6 years of heating. Since doubling the number of solar panels and BHEs in the solar thermal remediation system, the area enveloped by the 0.7 decay ratio contour more than doubled in size, increasing from 246 to 519 m^2. The area enveloped by the 0.45 decay ratio contour experienced a three-fold increase from 92 to 282 m^2.

6 Years	30+ %Decay	55+ %Decay
8 BHE : 8 collectors	246 m^2	92 m^2
16 BHE : 16 collectors	519 m^2	282 m^2

Table 13. Areas enveloped by the 0.7 (30% thermal enhancement) and 0.45 (55% thermal enhancement) decay ratio contours for the current system configuration compared with the optimized system after 6 years of heating.

Figure 55 shows the projected thermal enhanced decay of the optimized system configuration after 10 years of heating. The optimized simulation predicted much higher maximum decay ratios in the center of the Southwestern heat exchangers than the current system configuration, which remained below a value of 1 (See Figure 37). While the modeled decay ratio will never mathematically reach a value of 0, a significant portion of the optimized simulation has reached conditions of essentially complete decay, while a minimum decay ratio of 0.05 from the current system simulation occupied a much smaller area.

Table 14 summarizes the resulting increases in areas of decay that have been thermally enhanced by greater than 55 and 80% between the two model simulations after 10 years of heating. Since doubling the number of solar panels and BHEs in the solar thermal remediation system, the area enveloped by the 0.45 decay ratio contour more than doubled in

size, increasing from 219 to 493 m^2. The area enveloped by the 0.2 decay ratio contour

experienced more than a three-fold increase from 75 to 276 m^2.
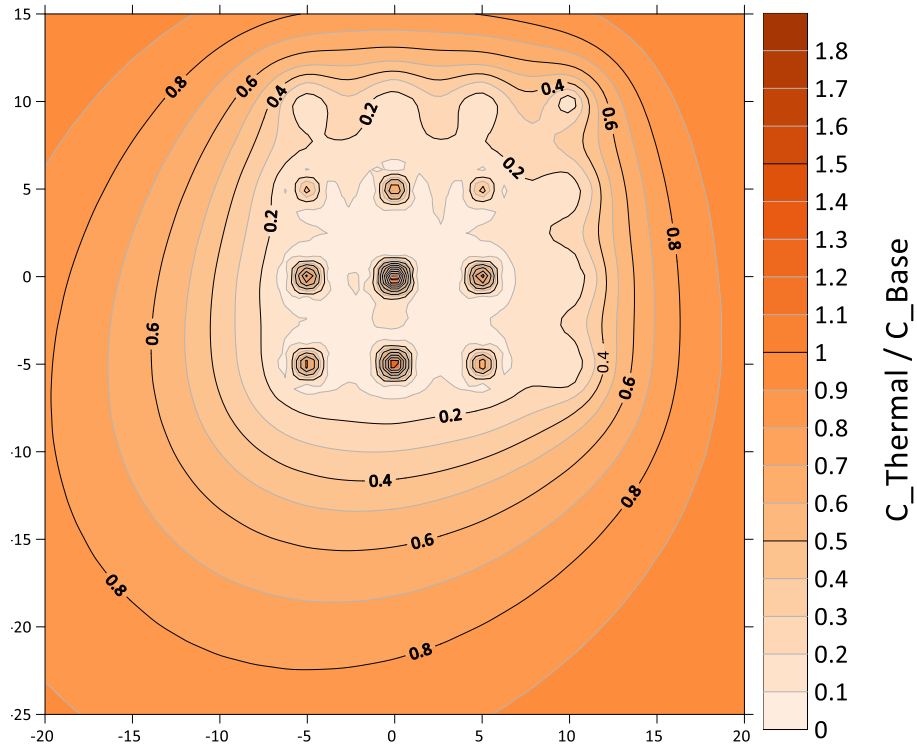
Fig. 55. Simulated thermal enhanced decay of the 2nd alternate
system configuration after 10 years of heating.

10 Years	55+ %Decay	80+ %Decay
8 BHE : 8 collectors	219 m^2	75 m^2
16 BHE : 16 collectors	493 m^2	276 m^2

Table 14. Areas enveloped by the 0.45 (55% thermal enhancement) and 0.2 (80% thermal
enhancement) decay ratio contours for the current system configuration compared with the
optimized system after 10 years of heating.

5.4 Summary

The decay tool component of the analytical model was used to simulate how the moderate rises in subsurface temperature that were projected in Chapter 4 could potentially enhance contaminant decay rates using estimated decay factors. Results for the current system configuration at the Vandenberg test site showed how cumulative decay could be thermally enhanced by 22% to 50% after 3 years of heating, 40% to 80% after 6 years of heating, and 70% to 90% after 10 years of heating.

The decay tool was used to demonstrate how this new addition to the analytical model could be used to optimize solar thermal remediation system design by 1) adding solar panels to the system to boost subsurface temperatures to peak thermal enhancement conditions and 2) adding BHEs to the system to boost the area of thermal enhanced decay. Results for the 1st optimized system configuration at the Vandenberg test site showed how cumulative decay could be thermally enhanced by 30% to 50% after 3 years of heating, 60% to 80% after 6 years of heating, and 80% to 100% after 10 years of heating.

The greatest differences in thermal enhanced decay from the current system configuration were evident in the areas between the heat exchangers for the first 6 years of heating, where temperatures were sustained in the assumed optimal mesophilic temperature range of 30 ∘C to 40 ∘C. After 10 years, the difference in thermal enhanced decay between the 2 simulations is more evident in the surrounding area outside the array of BHEs, as the projection for the current system reaches near 100% enhanced decay in areas close to the heat exchangers.

Results for the 2nd optimized system configuration showed how introducing additional heat exchangers can be effective in expanding the area of thermal enhanced decay. Doubling the number of BHE's while maintaining constant average daily power per borehole yielded decay areas two to four times larger than what was projected in the current system configuration. Like the 1st optimized system simulation, the greatest differences in thermal enhanced decay from the current system configuration were observed between the heat exchangers within the outer BHE array.

6   DISCUSSION

The analytical design tool is useful for modeling solar thermal remediation systems in simulating subsurface heat flow from BHE's. At the Vandenberg Space Force base test site, the model was able to reasonably predict temperature change at depths beneath the water table when operating with lower groundwater velocities (3-8 m/yr). Because of the model's assumption of total saturation with depth in its model domain, the analytical design tool may overestimate thermal conductivity within the vadose zone.

The recent addition of power factors to the variable heating rate section of the analytical model's user interface was proven effective in simulating the loss and return of power to specified BHEs in the solar thermal remediation system. These spatially variable heat inputs were able to adjust the average monthly power to both the affected heat exchangers (BHE-3 and BHE-5) as well as to the rest of the heaters in the system at correct times during the heating test. The major temperature decline that was observed from field data in late December as well as the overestimation of average monthly power values by the solar heat flow calculator may have been

possibly caused by inclement weather during the heating test and were not accounted for by the analytical model.

The recent addition of the thermal enhanced decay feature to the analytical model is a powerful tool that can be used to optimize solar thermal remediation systems. The model can produce detailed thermal enhanced decay estimates that provide insight into how the configuration of the remediation system can be altered to affect the extent and duration of thermal enhanced bioremediation projects. Therefore, this can be a valuable tool for planning stages of remediation projects by predicting necessary costs and time frames for operation.

For this project, site-representative decay factors were unavailable and so thermal enhanced decay results were estimated based on 3 main assumptions: 1) decay rates double at every 10 degree increase in temperature between 10 ∘C and 35 ∘C, 2) peak mesophilic conditions that maximize contaminant decay occur between 35 ∘C and 40 ∘C, and 3) thermal enhancement ceases at 40 ∘C, after which contaminant decay is inhibited. For future work using the analytical model to simulate thermal enhanced decay of a contaminated site, careful consideration should be made of the type of compound that is being modeled when assigning decay factors in the model input. If possible, decay factors that have been empirically determined on-site should be used.

WORKS CITED

Anderson, Mary P. Woessner, William W. Hunt, Randall J., 2015. Applied Groundwater Modeling - Simulation of Flow and Advective Transport (2nd Edition) - 2.1 Modeling Purpose. Elsevier.

Bryck, S., 2014. Numerical Modeling of Thermal Enhancement of *In Situ* Chemical Oxidation (ISCO) And Enhanced *In Situ* Bioremediation (EISB). MS Thesis, Queens University.

California Environmental Protection Agency. *Remediation of Chlorinated Volatile Organic Compounds in Vadose Zone Soil*, Department of Toxic Substances Control, 2010.

Chen, F., Freedman, D., Falta, R., Murdoch, L., 2012. Henry's Law Constants of Chlorinated Solvents at Elevated Temperatures. *Chemosphere, 86* (156-165).

Dettmer, K., 2002. A Discussion of the Effects of Thermal Remediation Treatments on Microbial Degradation Processes. U.S. Environmental Protection Agency Office of Solid Waste and Emergency Response Technology Innovation Office, Washington, DC.

Divine, C., 2020. *Thermal In-Situ Sustainable Remediation (TISR) To Enhance Biotic and Abiotic Reactions and Accelerate Remediation Timeframes*, U.S. Dept. of Defense, Environmental Security Technology Certification Program (ESTCP).

Ferguson, G., 2007. Heterogeneity and Thermal Modeling of Ground Water. *Groundwater*, *45*(4), 485-490.

Fetter, C. W., 2001. Hydraulic Conductivity of Earth Materials. *Applied Hydrogeology*, 4th ed., Pearson Education, Upper Saddle River, NJ, pp. 84-86.

Horst, J., Flanders, C., Klemmer, M., Randhawa, D.S., 2018. Low-Temperature Thermal Remediation: Gaining Traction as a Green Remedial Alternative. *Groundwater*, *38*(3), 18-27.

Lazaar, M., Bouadila, S., Kooli, S., Farhat, A., 2015. Comparative Study of Conventional and Solar Heating Systems Under Tunnel Tunisian Greenhouses: Thermal Performance and Economic Analysis. *Solar Energy, 120* (620-635).

Macbeth, T., Truex, M., Powell, T., Michalsen, M., ESTCP, 2012. Combining Low-Energy Electrical Resistance Heating with Biotic and Abiotic Reactions for Treatment of Chlorinated Solvent DNAPL Source Areas. ER-200719.

Man, Y., Yang, H., Diao, N., Liu, J., & Fang, Z., 2010. A new model and analytical solutions for borehole and pile ground heat exchangers. *International Journal of Heat and Mass Transfer*, 53(13-14), 2593-2601.

Margesin, R., Schinner, F., 2001. Biodegradation and Bioremediation of Hydrocarbons in Extreme Environments. *Applied Microbiology and Biotechnology, 56* (650-663).

Mehta, N., Gondaliya, V., Gundaniya, J., 2013. Applications of Different Numerical Methods in Heat Transfer – A Review. *International Journal of Emerging Technology and Advanced Engineering, 3* (363-368).

Molina-Giraldo, N., Blum, P., Zhu, K., Bayer, P., Fang, Z., 2011. A moving finite line source model to simulate borehole heat exchangers with groundwater advection. *International Journal of Thermal Sciences*, *50*(12), 2506-2513.

Ornelles, A., 2021. Development And Validation of An Analytical Modeling Tool for Solar Borehole Heat Exchangers. MS Thesis, Clemson University.

Ornelles, A., Falta, R., Divine, C., 2022. A Design Tool for Solar Thermal Remediation Using Borehole Heat Exchangers. *Groundwater*, *61*(2), 245-254.

Philippe, M., Bernier, M., & Marchio, D., 2009. Validity ranges of three analytical solutions to heat transfer in the vicinity of single boreholes. *Geothermics*, *38*(4), 407-413.

Ren, J., Song, X., Ding, D., 2020. Sustainable Remediation of Diesel-Contaminated Soil by Low Temperature Thermal Treatment: Improved Energy Efficiency and Soil Reusability. *Chemosphere, 241*.

Solar Panels Plus, SPP-30A SRCC Certification. (2020)

http://www.solarpanelsplus.compdfs/spp30a-srcc.pdf

Solar Panels Plus, SPP Spartan Spec Sheet. (2020)

http://www.solarpanelsplus.com/pdfs/spp-spartanspecs.pdf

Suthersan, S., Horst, J., Klemmer, M., Malone, D., 2012. Temperature-Activated Auto-Decomposition Reactions: An Under-Utilized In Situ Remediation Solution. *Groundwater Monitoring & Remediation*, *32*(3), 34-40.

Truex, M., Powell, T., Lynch, K., 2007. In Situ Dechlorination of TCE during Aquifer Heating. *Groundwater*, *27*(2), 96-105.

United States, Congress, U.S. Geological Survey, Reston, Virginia, et al. *Volatile Organic Compounds in the Nation's Ground Water and Drinking-Water Supply Wells: A Summary*, U.S. Dept. of the Interior, U.S. Geological Survey, 2006.

Vidonish, J., Zygourakis, K., Masiello, C., Sabadell, G., Alvarez, P., 2016. Thermal Treatment of Hydrocarbon-Impacted Soils: A Review of Technology Innovation for Sustainable Remediation. *Engineering, 2*(4), 426-437.

Xu, J., Yeung, P., Johnson, R., 1997. Biodegradation of Petroleum Hydrocarbons in Soil as Affected by Heating and Forced Aeration. *Journal of Environmental Quality*, *26*(6), 1511-1516.

APPENDIX

1 Modeling Tool User Interface

The solar thermal remediation design tool is coded in Visual Basic and the main

graphical user interface is presented on a single Microsoft Excel tab for ease of use as (Figure

56).

3D Analytical solution for borehole heat exchanger with regional GW flow					Averag e Power	Power Factor	Power Factor	Power Factor	Power Factor	Power Factor	Power Factor	Power Factor	Power Factor	Power Factor	Power Factor		Nmbr Inc	21.00	
Ron Falta 6/28/ Run Program					Q (Wat	BHE 4	BHE 2	BHE 3	BHE 1	BHE 5	BHE 6	BHE 7	BHE 8				zobs	yobs	zobs
Darcy velocity	5	m/yr	month	months															
number of heaters	8	unitless	Jan	1	252.3	1	1	1	1	1	1	1	1				3.77	0.63	5.33
Background T	18.5	C	Feb	2	272	1	1	1	1	1	1	1	1				3.77	0.63	6.35
porosity	0.38	unitless	Mar	3	292	1	1	1	1	1	1	1	1				3.77	0.63	7.37
Rock heat capacity	790	J/kg*C	Apr	4	312	1	1	1	1	1	1	1	1				3.77	0.63	8.39
Rock grain density	2200	kg/m^3	May	5	332	1	1	1	1	1	1	1	1				3.77	0.63	9.40
Thermal conductivity	2	W/m*C	Jun	6	355	1	1	1	1	1	1	1	1				3.77	0.63	10.42
Heater length	6.1	m	Jul	7	164.4	1	1	1	1	1	1	1	1				-2.41	0.5	5.21
depth to top of heater	6.1	m	Aug	8	313.5	1	1	1	1	1	1	1	1				-2.41	0.5	6.22
Snapshot flag xy=1, xz=2, time series =-	1.0		Sep	9	225.5	1	1	1	1	1	1	1	1				-2.41	0.5	7.24
xmin	-20	m	Oct	10	247.1	1.33	1.33	0	1.33	0	1.33	1.33	1.33				-2.41	0.5	8.26
xmax	20	m	Nov	11	321.6	1.33	1.33	0	1.33	0	1.33	1.33	1.33				-2.41	0.5	9.27
ymax	15	m	Dec	12	232.4	1	1	1	1	1	1	1	1				-2.41	0.5	10.29
ymin	-25	m	Jan	13	252.3	1	1	1	1	1	1	1	1				4.43	-4.30	5.11
dx	1	m	Feb	14	272	1	1	1	1	1	1	1	1				4.43	-4.30	6.13
dy	1	m	Mar	15	292	1	1	1	1	1	1	1	1				4.43	-4.30	7.15
z for xy plot	3	m	Apr	16	312	1	1	1	1	1	1	1	1				4.43	-4.30	8.16
y for xz plot	0		May	17	332	1	1	1	1	1	1	1	1				4.43	-4.30	9.18
zmin (depth)	0	m	Jun	18	355	1	1	1	1	1	1	1	1				4.43	-4.30	10.20
zmax (depth)	25	m	Jul	19	350	1	1	1	1	1	1	1	1				-10.10	2.27	5.19
dz	1	m	Aug	20	313.5	1	1	1	1	1	1	1	1				-10.10	2.27	6.21
N Gauss (integration)	16		Sep	21	225.5	1	1	1	1	1	1	1	1				-10.10	2.27	7.23
Flow direction angle	235	degrees	Oct	22	247.1	1	1	1	1	1	1	1	1						
t start, day of year	152	days	Nov	23	321.6	1	1	1	1	1	1	1	1						
t end, days since start	3650	days	Dec	24	232.4	1	1	1	1	1	1	1	1						
delta t for time series and decay integra	300	days	Jan	25	252.3	1	1	1	1	1	1	1	1						
flag for decay integration calculation (>	1		Feb	26	272	1	1	1	1	1	1	1	1						
base decay rate	0.34657	1/yr	Mar	27	292	1	1	1	1	1	1	1	1						
retardation factor	2		Apr	28	312	1	1	1	1	1	1	1	1						
temperature C	**decay factor**		May	29	332	1	1	1	1	1	1	1	1						
0	0.1		Jun	30	355	1	1	1	1	1	1	1	1						
5	0.2		Jul	31	350	1	1	1	1	1	1	1	1						

Figure 56. Graphical user interface for the analytical design model.

1A. Model Input

The design tool interface allows the user to define the thermal and hydrogeologic

properties of the subsurface matrix, as well as set physical locations for the heat exchangers.

Figure 57 shows some of these model inputs, such as Darcy velocity, thermal conductivity, and

depth to the top of the heaters.

With a snapshot flag input cell, the user can direct the model to generate temperature output data that can be used to plot either a contour map at a set time or a time series plot at specified points in space.

Darcy velocity	5	m/yr
number of heaters	8	unitless
Background T	18.5	C
porosity	0.38	unitless
Rock heat capacity	790	J/kg*C
Rock grain density	2200	kg/m^3
Themal conductivity	2	W/m*C
Heater length	6.1	m
depth to top of heater	6.1	m

Fig. 57. Model input section for hydrogeologic, thermal, and heater properties.

Figure 58 highlights the snapshot flag that gives instructions on how to generate XY, XZ, and time series data along with parameters defining the locations where the solution is evaluated. XY output contour data will reflect a slice plane through the z axis at the specified "z for xy plot" input section. Figure 59 shows the resulting aerial view of the modeled solar thermal remediation system after plotting XY output data.

Snapshot flag xy=1, xz=2, time series =-1	1.0	
xmin	-20	m
xmax	20	m
ymax	15	m
ymin	-25	m
dx	1	m
dy	1	m
z for xy plot	9	m
y for xz plot	0	
zmin (depth)	0	m
zmax (depth)	25	m
dz	1	m

Figure 58. Snapshot flag indicating the data output type from the analytical model.

This simulation setting can give insight on the extent of temperature change that has occurred in the area surrounding the BHEs after a specified amount of time at an indicated depth.

Conversely, XZ output contour data will reflect a slice plane through the y axis at the specified "y for xz plot" input section. Figure 60 shows the resulting cross-sectional view of the modeled solar thermal remediation system after plotting XZ output data. This simulation setting can give insight on the extent of temperature change that has occurred with depth surrounding the BHEs into the subsurface after a specified amount of time.
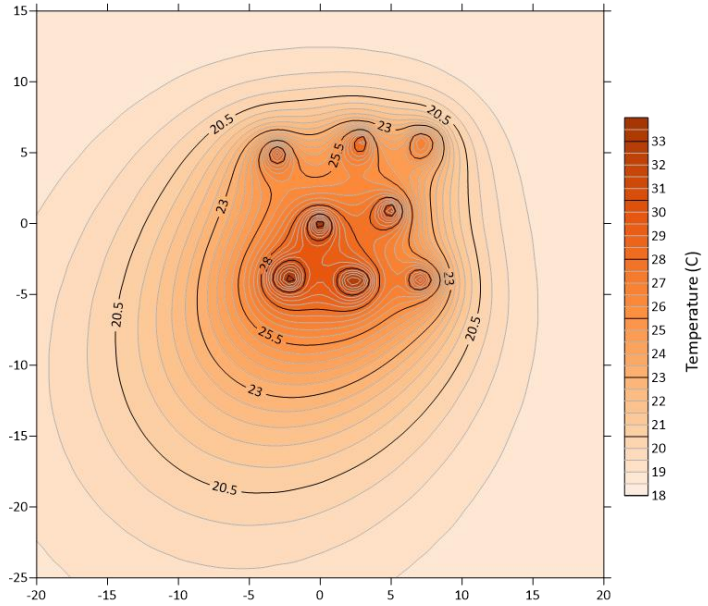

Fig. 59. XY contour plot from an analytical model temperature simulation.
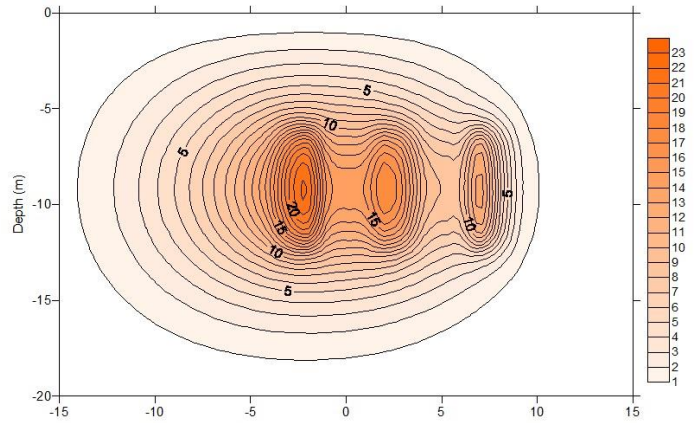
Fig. 60. XZ contour plot from an analytical model temperature simulation.

1B. Thermal Enhanced Decay

An additional snapshot flag input cell on the model interface allows for the option of generating thermal-enhanced decay results that can also be plotted as a contour map. Figure 61 shows the input sections for the decay integration tool, such as the base decay rate, retardation factor, and a set of decay factors that are each assigned to a specific temperature.

The tool then calculates the decay ratio at every point in space at the specified end-time. The user can then easily transfer and plot the output data to other plotting software for further analysis. Figure 62 shows an example of a thermal enhanced decay plot using the built-in decay tool.

flag for decay integration calculation (>0)		-1	
base decay rate		0.34657	1/yr
retardation factor		2	
temperature C		**decay factor**	
0		0.1	
5		0.2	
10		0.5	
15		0.71	
20		1	
25		1.41	
30		2	
35		2.8	
40		4	
45		2	
50		1	
55		0.5	
60		0.2	

Fig. 61. Thermal enhanced decay input window in the model's user interface.

Fig. 62. Thermal enhanced decay contour plot generated using the analytical model's decay tool.

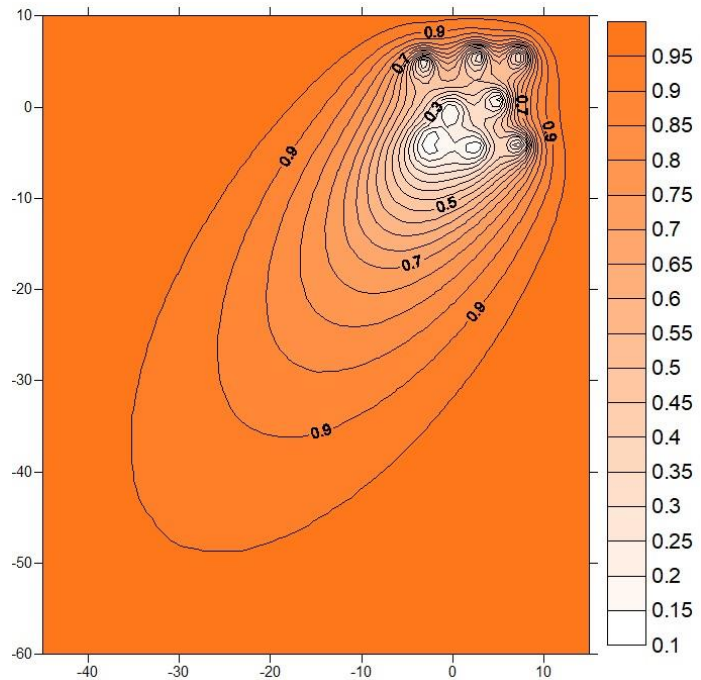The analytical design tool uses a local coordinate system to model the solar thermal remediation system. The user can define any number of heat exchanger coordinates in space which are placed at the user's specified depth. Figure 63 shows an example where 8 BHE's have been defined.

Heater Coordinates	
x (m)	y (m)
0	0
2.746951219	5.695121951
7.426829268	5.704268293
-3.042682927	4.972560976
5.045731707	0.951219512
-2.323170732	-3.640243902
2.536585366	-4.06097561
7.387195122	-3.829268293

Fig. 63. User input for heat exchanger coordinates in the local coordinate system.

Observational points can also be input into the local coordinate system that can record temperature time series plots. Figure 64 shows an example where 15 observation points have been defined in the coordinate system.

N obs loc	15.00		
xobs	yobs	zobs	
7.426829268	5.70426829	8	BHE-3 TEST
5.045731707	0.95121951	8	BHE-5 TEST
4.95	5.69	10.318	DTS-3 bottom
3.77	0.69	6.351	DTS-5 top
3.77	0.69	8.385	DTS-5 center
3.77	0.69	10.42	DTS-5 bottom
2.66	0.74	6.275	DTS-6 top
2.66	0.74	8.309	DTS-6 center
2.66	0.74	10.342	DTS-6 bottom
-2.41	0.50	6.223	DTS-7 top
-2.41	0.50	8.26	DTS-7 center
-2.41	0.50	10.29	DTS-7 bottom
4.432926829	-4.2957317	6.13	DTS-9 top
4.432926829	-4.2957317	8.164	DTS-9 center
4.432926829	-4.2957317	10.20	DTS-9 bottom

Fig. 64. User input for observation point coordinates in the local coordinate system.

When the model is run, the output time series data are arranged in columns in order of the input observation points on the user interface which can be easily plotted in Excel. Figure 65 shows an example where the temperature at 5 different observation locations has been plotted with time.
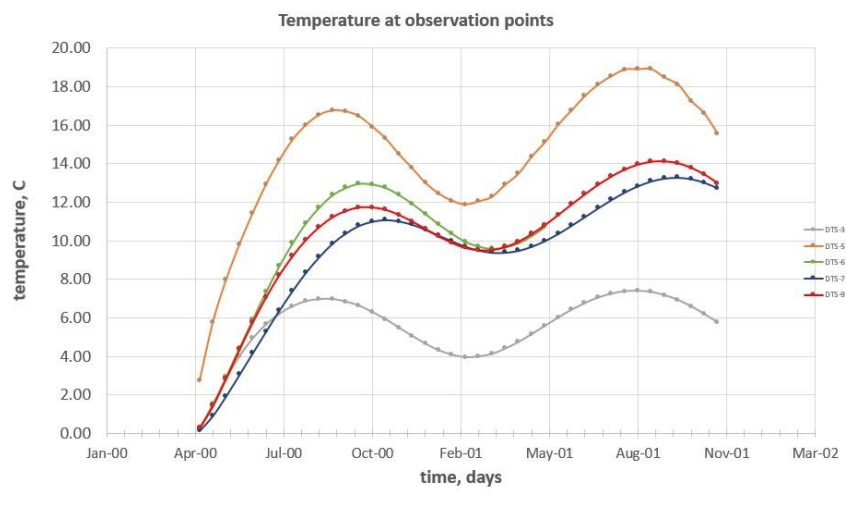

Fig. 65. Example of a temperature time series plot of selected observation points.

1D. Variable Heating Rate

The analytical design tool uses average monthly power-per-borehole values to calculate subsurface temperature change. If these values are known, the user can input the average monthly power (W) manually in the red column shown in Figure 66. Within the blue window, the power supplying each BHE can be manipulated by providing power factor input cells.

months	Average Power Q (Watts)	Power Factor BHE 4	Power Factor BHE 2	Power Factor BHE 3	Power Factor BHE 1	Power Factor BHE 5	Power Factor BHE 6	Power Factor BHE 7	Power Factor BHE 8	Power Factor	Power Factor
1	267.5471	1	1	1	1	1	1	1	1		
2	362.2408	1	1	1	1	1	1	1	1		
3	488.499	1	1	1	1	1	1	1	1		
4	610.248	1	1	1	1	1	1	1	1		
5	692.917	1	1	1	1	1	1	1	1		
6	354.99	1	1	1	1	1	1	1	1		
7	164.41	1	1	1	1	1	1	1	1		
8	313.48	1	1	1	1	1	1	1	1		
9	225.48	1	1	1	1	1	1	1	1		
10	247.1169	1.33	1.33	0	1.33	0	1.33	1.33	1.33		
11	321.61	1.33	1.33	0	1.33	0	1.33	1.33	1.33		
12	249.1	1	1	1	1	1	1	1	1		
13	250	1	1	1	1	1	1	1	1		
14	275	1	1	1	1	1	1	1	1		
15	300	1	1	1	1	1	1	1	1		
16	325	1	1	1	1	1	1	1	1		
17	350	1	1	1	1	1	1	1	1		
18	354.99	1	1	1	1	1	1	1	1		
19	350	1	1	1	1	1	1	1	1		
20	313.48	1	1	1	1	1	1	1	1		
21	225.48	1	1	1	1	1	1	1	1		
22	247.1169	1	1	1	1	1	1	1	1		
23	321.61	1	1	1	1	1	1	1	1		
24	249.1	1	1	1	1	1	1	1	1		
25	250	1	1	1	1	1	1	1	1		
26	275	1	1	1	1	1	1	1	1		
27	300	1	1	1	1	1	1	1	1		
28	325	1	1	1	1	1	1	1	1		
29	350	1	1	1	1	1	1	1	1		

Fig. 66. Monthly power (red) and power factor inputs (blue) allow the user to manipulate the power being supplied to any heater in the solar thermal remediation system on a month-to-month basis.

These factors are multiplied by the average power rate for that month and allow the user to turn specific BHE's on/off, or increase/decrease the power being supplied to those heaters for that specific month. If the average monthly solar power values are unavailable to the user, then they can be estimated using a built-in solar power calculator.

1E. Solar Power Calculator

The solar power calculator was developed by Ornelles (2021) and can estimate the average monthly power generated from solar collectors and that is applied to the thermal remediation system given the makeup of the system along with its geographic location. Shown in Figure 67, the user interface for the calculator is located on a separate tab in the analytical model's Excel sheet. The user inputs the number and size of solar panels along with the number of BHE's in the solar thermal remediation system, the lat/long coordinates of the site of interest, the collector thermal efficiency, and the average daily global tilted solar irradiation (GTI) of the site's geographic location to estimate the monthly average power delivery per borehole in watts.
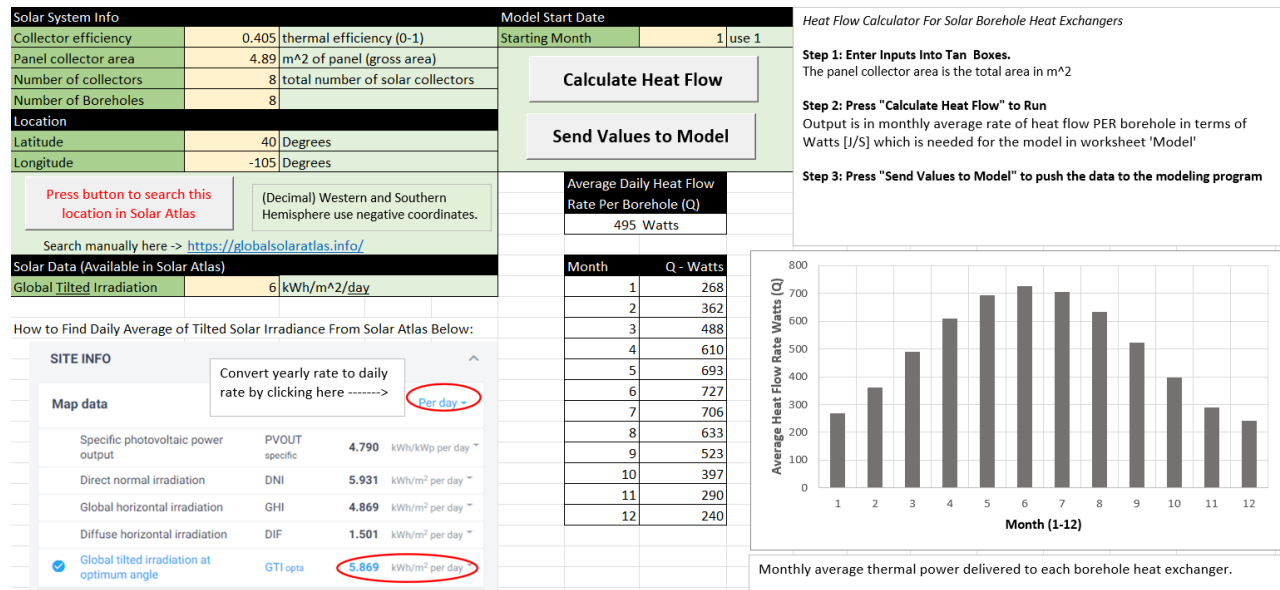

Fig. 67. Solar power calculator user interface.

The total solar energy produced by the system depends on the GTI, area, and efficiency of the solar collectors, where the solar irradation and total solar power output share a positive linear relationship (Ornelles, 2021). The thermal efficiency of the solar collectors is the ratio of actual power generated by the system to the total potential energy, or the solar irradation:

$$Collector\ Efficiency = \frac{power\ generated\ (\frac{kWh}{m^2d})}{solar\ irradation\ (\frac{kWh}{m^2d})}$$

Figure 68 shows how the thermal efficiency of solar panels can vary with increasing solar irradation and power generated from the system.
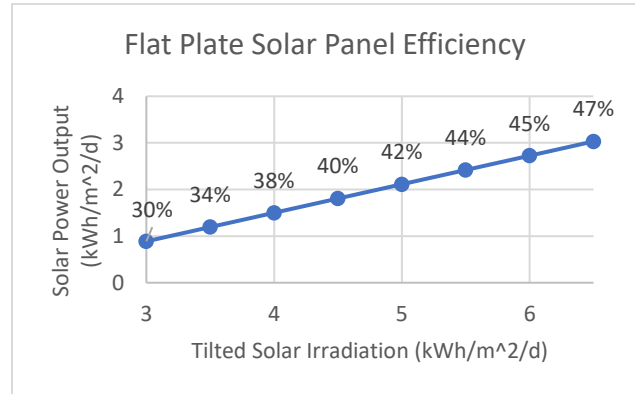

Fig. 68. Varying flat plate solar panel efficiency as a function of solar irradiation and solar power output (Solar Panel Plus SPP-Spartan, 2020).

Seasonal fluctuations from varying monthly solar insolation are modeled using the Nasa ModelE AR5 SRMONLAT solar insolation modeling code (Ornelles, 2021). The code uses the site latitude, solar incidence angle, orbit, and tilt of the earth to calculate the solar insolation variance. A reference table is built into the model that lists monthly percent change in insolation for every latitude and is used by the solar insolation tool to calculate average monthly heat flow.

The solar energy is converted to a rate of power in watts and divided by the number of boreholes to get an annual, average heat flow rate per borehole. Once the variable heat flow is calculated, the user can easily transfer the heating rate for entry into the analytical model by pushing the "send values to model" button on the solar heat flow calculator interface and the values will then populate the heat flow column in the center of the main interface of the analytical design tool.